University of Strathclyde

Department of Physics

Spectral matching by radiative transfer theory: a physics-based approach to marine remote sensing

Danielle Elizabeth Creanor

A thesis presented in fulfillment of the requirements for the degree of Doctor of Philosophy

2012

Declaration of Author's Rights

This thesis is the result of the author's original research. It has been composed by the author and has not been previously submitted for examination which has led to the award of a degree.

Signed:

Date:

This thesis is dedicated to my Mum and Dad,
Veronica and Richard Creanor

Abstract

The propagation of natural light in turbid media (including seawater) is determined by both the conditions of illumination and the inherent optical properties of the medium. The illumination conditions include solar angle, degree of cloud cover and sea state, while the relevant inherent optical properties are the spectral coefficients of absorption and scattering and the scattering phase function. These inherent optical properties are functions of seawater composition, including the concentrations of phytoplankton, suspended minerals and dissolved organic substances. Given knowledge of the concentrations of these materials and their specific optical cross-sections, the reflectance of a water body can be calculated using radiative transfer theory. However the inverse process, the determination of constituent concentrations from reflectance, is not directly soluble. This problem of reflectance inversion is at the heart of remote sensing of oceanic processes using satellite borne radiometers, and its solution is of great significance in modern oceanography, planetary science and climate change modelling. The hypothesis underlying this thesis is that the inversion of remote sensing signals can be achieved by a process of spectral matching, in which the water-leaving radiance spectra observed from space are compared with a database of spectra calculated using radiance transfer theory for water columns of known composition. This thesis has sought to implement a comprehensive look-up table (*LUT*) that can be expediently interrogated using a simple inversion algorithm that can be easily adapted to new datasets.

Acknowledgements

I would like to take this opportunity to thank those who have contributed and supported me throughout my PhD and who have made the completion of this thesis possible. Firstly, I owe my supervisor, Professor Alex Cunningham my sincere thanks and gratitude for his patience and support. Alex, your guidance has been invaluable and we made it in the end!

I would like to thank my partner, Marco for his endless love and support, without which the completion of this thesis would have been considerably more challenging. I would also like to thank my friends for their support; in particular Jennifer, my office and Friday night drinking buddy. Thank you for your support and advice, it has been invaluable.

Finally, I would like to thank my family; my Mum Veronica, Dad Richard, brother Richie and sister Lorna-Dawn, whose unwavering support, encouragement, words of comfort and unconditional love are the sole reason that I have managed to complete all my academic endeavors. Mum and Dad, it is because of you that I have been able to take advantage of all the opportunities that have been given to me, Thank You!

Contents

List of Figures

List of Tables

Abbreviations

TSM: Total Suspended Material

LUT: Look-up Table

MSS: Mineral Suspended Sediment

CDOM: Colour Dissolved Organic Material

CHL: Chlorophyll

IOPs: Inherent Optical Properties

AOPs: Apparent Optical Properties

OSM: Optically Significant Material

SIOPs: Specific Inherent Optical Properties

RMSE: Root Mean Square Error

Rrs: Remote Sensing Reflectance

NLw: Normalised Water Leaving Radiance

LM: Levenberg Marquardht

ANN: Artificial Neural Networks

SeaWiFS: Sea-Viewing Wide Field of view Sensor

OCTS: Ocean Colour and Temperature Sensor

MODIS: Medium Resolution Imaging Spectrometer

GLI: Global Imager

MERIS: Medium Resolution Imaging Spectrometer

ESA: European Space Agency

HSE: Hyper Spectral Environmental Suite

UAV: Unmanned Airborne Vehicle

PSD: Particle Size Distribution

RTE: Radiative Transfer Equation

VSF: Volume Scattering Function

POM: Particulate Organic Material

PIM: Particulate Inorganic Material

IPA: Individual Particle Analysis

SPMR: SeaWiFS Profiling Multispectral Radiometer

PSO: Particle Swarm Optimisation

Chapter 1

Introduction

The propagation of natural light in turbid media (including seawater) is determined by both the conditions of illumination and the inherent optical properties of the medium. The illumination conditions include the solar angle, the level of cloud cover and the sea state, while the relevant inherent optical properties (*IOPs*) are the spectral coefficients of absorption and scattering and the scattering phase function (β). These *IOPs* are functions of seawater composition, including the concentrations of phytoplankton, suspended minerals and dissolved organic substances. Radiative transfer theory can be used to calculate the reflectance of a water body when the concentrations of these materials and their specific optical cross-sections are known. However, the inverse problem i.e. the determination of constituent concentrations from a reflectance signal is not directly soluble. This problem of reflectance inversion using satellite borne radiometers is at the heart of remote sensing of oceanic processes and consequently, its solution is of great significance in modern oceanography, planetary science and climate change modeling. This chapter discusses the motivation for this thesis as well as the obstacles that arise in the direct and inverse problems of radiative transfer theory. It also presents an overview of some modern approaches to ocean colour inversion. These techniques are, however, conceptually complex and often require a degree of algorithm training that makes their application to new data sets time consuming. Consequently, there are potential advantages in disregarding more mathematically complex algorithms in favour of a more simple approach.

1.1 Motivation for this work

Optical remote sensing using satellite-borne radiometers has become an important tool for studying biological and physical processes in ocean basins (Dickey *et al*, 2004; Platt *et al.*, 2008), and is recognised as being potentially of great value for monitoring the changing status of coastal waters and shelf seas (Petersen *et al.*, 2008). Unfortunately, remote sensing algorithms derived using global data sets are not reliable when applied to waters subject to terrestrial influence (Robinson 2006). These waters are often classified as case 2 waters and contain optically significant concentrations of inorganic particles and coloured dissolved matter as well as phytoplankton cells. Conversely, case 1 waters describe regions where the optical properties are highly correlated with chlorophyll concentrations; this classification is often used to describe the clearer waters of the open ocean (Morel and Prieur, 1977).

The unreliability of remote sensing algorithms in case 2 waters was a problem identified by Morel and Prieur (1977), who distinguished between waters where optical variability is correlated with phytoplankton population density and those where this correlation is disrupted by the presence of a wider range of optically significant materials (*OSMs*). Shelf seas generally fall into the latter category. In the simplest analysis, *OSMs* fall into three classes: phytoplankton cells (measured as chlorophyll concentration, *CHL*), suspended mineral particles (measured as the dry weight of mineral suspended solids per unit filtered volume, *MSS*) and dissolved coloured organic material (measured as the absorption coefficient of filtered samples at 440 nm, *CDOM*).

Deriving reliable and accurate *OSM* concentrations from remote sensing reflectance (R_{rs}) signals, in the visible waveband, is a central problem in marine remote sensing and the principal focus of this thesis. The underlying hypothesis of the research presented here was that the inversion of remote sensing signals could be achieved by a process of spectral matching. This would involve the comparison of water-leaving radiance spectra

with a look-up table (*LUT*) of spectra that are calculated using radiative transfer theory for water columns of known composition (Mobely *et al.*, 2002). Specific optical cross sections that were representative of the Western UK shelf sea had been determined previously, but there were still a number of challenging problems to be solved. The problems addressed will include:

1) The need for an effective computational scheme for *LUT* searching.
2) Alternatives to radiative transfer calculations, which are time consuming when many runs have to be carried out, for *LUT* production.
3) Assessment of the degree to which ambiguities exist in the spectral matching process.
4) Robustness of a spectral matching approach to remote sensing inversion using modelled data to which varying degrees of statistical noise have been added.
5) The implications of applying *LUT*-based inversion to different geographical regions where water constituents may have significantly different optical properties.
6) Application of the spectral matching inversion algorithm to *in situ* data and the quality of the constituent matches retrieved.

The remainder of this chapter introduces the concept of forward and inverse radiative transfer modelling, where the complexity of the inverse problem is explored. The techniques that are currently employed to overcome the difficulties of remote sensing inversion will be discussed, as well as the technologies that make global ocean measurements possible. Some inversion techniques can be labour intensive and this, coupled with the associated computational burden is one of the primary reasons that a simple spectral matching inversion algorithm has been developed in this thesis. An easily adaptable inversion algorithm is highly desirable for the investigation of ocean colour, where fast and reliable results can be obtained without the time constraints that are associated with the more complex techniques.

1.2 Direct and Inverse problems in marine remote sensing

The radiative transfer forward model uses *IOPs* and boundary conditions to calculate radiance distributions within and leaving a water body. This forward model provides a physically-derived radiance distribution for a given set of *IOPs* and boundary conditions. The physical properties of *OSMs*, such as the volume scattering function (*VSF*) and particle size distribution are used to derive the *IOPs* for the water body of interest. This 'direct' problem of radiative transfer, for the calculation of radiance distributions, is described in Mobley *et al.*, (2005) and outlined in Figure 1.1.

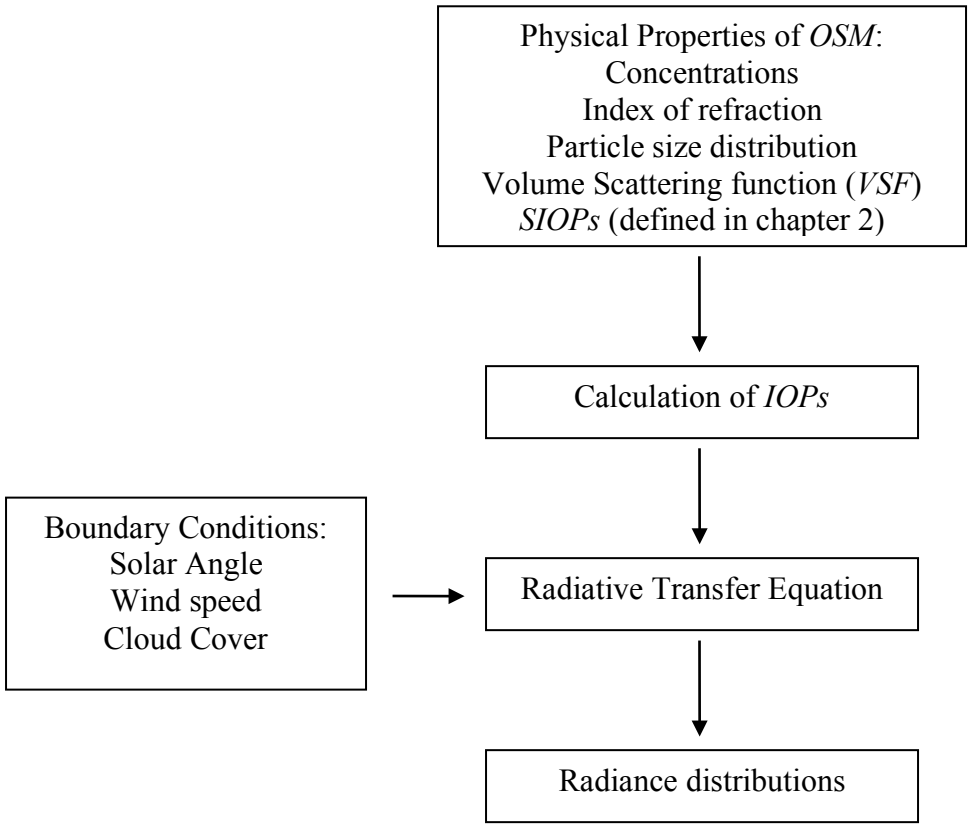

Figure 1.1: A simplified overview of the forward 'direct' radiative transfer problem (Mobley *et al.*, 2005).

The inverse problem of radiative transfer, in contrast to the forward model, attempts to identify water constituents from radiance distributions that are obtained from satellites or radiometric instruments. Natural variability in the illumination conditions, such as the solar angle, means that the radiance distribution can be different even though the *IOPs* remain the same. Consequently, two significant questions associated with this inversion process are the uniqueness of the solution obtained and its sensitivity to measurement errors. The stages of radiative transfer inversion, for the determination of ocean properties such as *OSM* concentrations, are outlined in figure 1.2 (Mobley *et al.*, 2005).

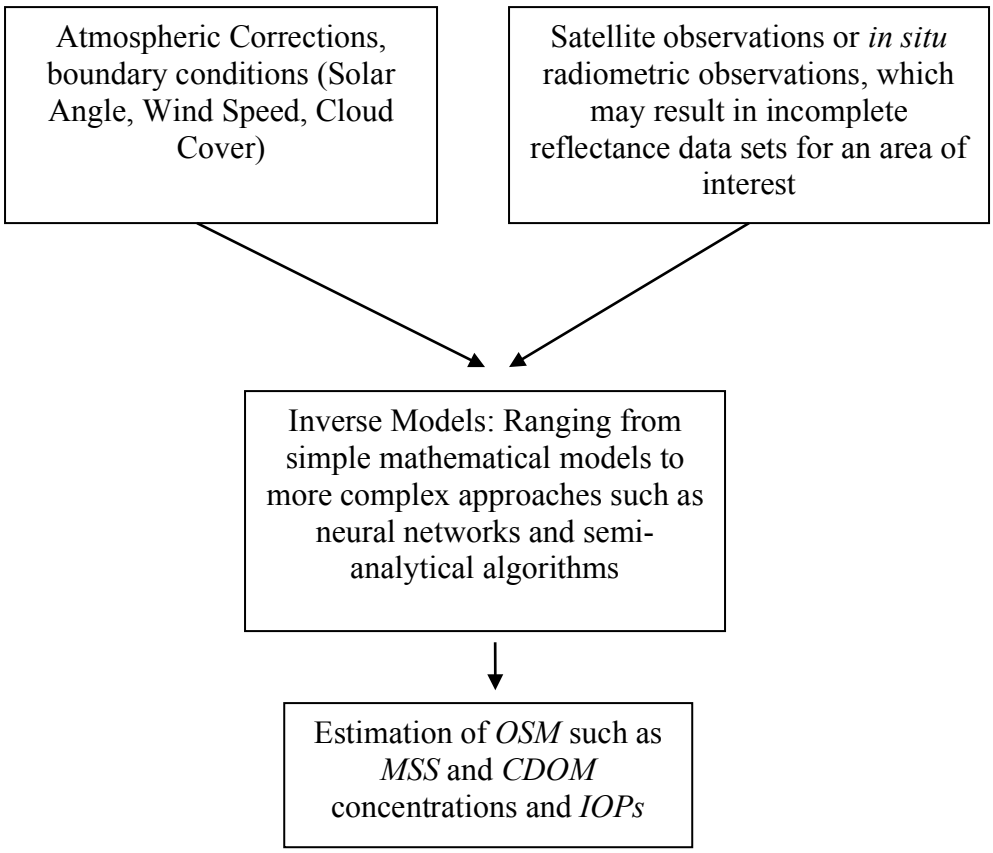

Figure 1.2: A simplified overview of the inverse radiative transfer problem (Mobley *et al.*, 2005).

1.3 Modern approaches to ocean colour inversion

Early approaches to ocean colour inversion were empirical, relying on statistically derived relationships between ocean colour signals and *OSM* concentrations. These approaches were relatively successful in retrieving chlorophyll concentrations in ocean basins, but performed poorly when applied to coastal waters. More recently, attempts have been made to recover *OSM* concentrations by matching the observed spectra with the predictions of models that are based on hypothesised *OSM* concentrations (Garver and Siegel, 1997). Consequently, the spectral matching approach to the inversion of remotely sensed data for the purposes of ocean colour interpretation can be described in three stages:

1. Implementation of a forward model for the generation of spectra that will be used for comparative purposes.
2. Derivation of an objective function that is to be minimized in the matching process.
3. Development of a search algorithm that will optimise the quality of spectral matching achieved.

A number of spectral matching algorithms for stage three of the inversion process will be discussed in chapter 5, where it is noted that the choice of matching algorithm has little effect on the quality of matches obtained. In addition to spectral matching, there are a number of other, more complex methods that can be used to interpret remotely sensed radiance data. These methods include: the Levenberg-Marquardt (*LM*) multivariate optimisation algorithm, genetic algorithms, particle swarm optimisation and neural networks (Chen *et al.*, 2009). Following a brief description of each method, the benefits of adopting a simple *LUT*-based spectral matching approach, instead of more complex techniques, shall be highlighted.

a) *Levenberg-Marquardt (LM)* multivariate optimisation

The *LM* multivariate optimisation algorithm operates as an iterative process, whereby an interpolation is performed between a Gauss-Newton algorithm and a gradient descent method. The procedure is initiated when the user supplies the algorithm with an initial value for the parameter β. This parameter is then changed at each iteration step with new estimates, $\beta + \sigma$. The σ factor is determined by the linearisation of the functions:

$$f\left(x_i, \beta + \sigma\right) \approx f\left(x_i, \beta\right) + j_i \sigma \tag{1.1}$$

where,

$j_i = \dfrac{\partial f\left(x_i, \beta\right)}{\partial \beta}$, is the gradient of f with respect to β. (1.2)

A value of 0 will be obtained when the sum of squares $S(\beta)$, which is the gradient of S with respect to σ, is at its minimum. This first order approximation of $f\left(x_i, \beta + \sigma\right)$ gives:

$$S\left(\beta + \sigma\right) \approx \sum_{i=1}^{m} \left(y_i - f\left(x_i, \beta\right) - j_i \sigma\right)^2 \tag{1.3}$$

and taking the derivative, with respect to σ and setting the result to 0, gives the Levenberg-Marquardt optimization which is a set of linear equations that can be solved for σ:

$$\left(J^T J + \lambda diag\left(J^T J\right)\right)\sigma = J^T \left[y - F\left(\beta\right)\right] \tag{1.4}$$

J is the Jacobian matrix which is a 1st order partial derivative matrix of a vector or a scalar valued function, with respect to another vector. F and y are the vectors with the i^{th}

component $f(x_i, \beta)$ and y_i respectively. The λ represents a damping factor: if one iteration has failed to reduce the residual difference sufficiently, this damping factor can be increased.

The *LM* algorithm is considered an established technique (Lourakis, 2005) that can be used to find a solution to a multivariate function for non-linear least squares problems (Levenberg, 1944; Marquardt, 1963). This type of optimisation is used in hydrological optics, including the GSM01 algorithm (for chlorophyll retrieval), where it is used to fit modeled remote sensing reflectance (R_{rs}) data to measured R_{rs} spectra and to retrieve absorption and scattering properties of R_{rs} spectra (Maritorena *et al.*, 2002; Slade, 2004; Kormick *et al.*, 2009). Korosov *et al.* (2009) used a semi empirical algorithm that was based on *LM* optimisation for the retrieval of *OSMs* from satellite remote sensing data.

b) Genetic Algorithms

Genetic algorithms are another type of multivariate optimization, which in this case, follow Darwinian-style natural selection. Populations of potential solutions are assessed by their 'fitness' in accordance with the objective *COST* function (Kostadinov *et al.*, 2007):

$$COST = 0.2Nneg + \sum_{k=1}^{N_\theta} \left(\left|1 - R_k^2\right| + 1.5\left|1 - a_k\right| + RMS_K \right) + 0.2\sqrt{\frac{\sum_{i=1}^{N_\psi} \left(\frac{\hat{\psi}_i - \psi_i}{\psi_i} \right)^2}{N_\psi}} \qquad (1.5)$$

where R_k^2 is the square of the correlation coefficient between the k^{th} measured and retrieved variable, *Nneg* is the number of negative retrievals, RMS_k is the root mean square for the *kth* value and a_k is the slope of the type II regression of the *kth* retrievals on the measurements. An *a priori* penalty is incurred when there is large deviations of the optimized parameters (ψ) from parameters of a pre-calculated data set and while N_θ

is the number of variables to be retrieved (Kostadinov *et al.*, 2007). In the context of hydrological optics, the number of variables would be three: *CHL*, *MSS* and *CDOM*. In contrast to other techniques, generic algorithms do not require a library or database of pre-calculated data to be constructed. However, the methodology consists of three parts: a forward model for the generation of spectra, the objective function that is to be minimised and a search algorithm that performs the optimization, and is therefore consistent with the standard approach to solving the inverse problem of remote sensing. Zhan *et al.*. (2003) used genetic algorithms to obtain apparent optical properties (*AOPs*, described in Chapter 2) from measurements of ocean colour. Their results showed that genetic algorithms could be successfully employed to retrieve optical properties from remote sensing reflectance. The authors claim to have a 60% accuracy for predicting *CHL*, 76% for the prediction of the particulate backscattering coefficient (443nm) and 95 % accuracy for the *CDOM* absorption coefficient.

c) Particle Swarm Optimisation

Particle swarm optimisation (*PSO*) is an adaptive algorithm which shares some features with genetic algorithms. In *PSO*, a population of 'individuals' adapt by random searches in regions of the search area (i.e. a database). 'Individuals' move randomly forwards from their original or previous optimum position in conjunction with the optimum position for the total swarm. A 'neighborhood' approach can also be adopted which involves directional movement to the best position that has been determined by the swarm within a group of particles, the 'neighborhood'. The fundamental principle of *PSO* is that a particle will constantly refine its search efforts within the 'neighborhoods', with each individual component of the overall swarm representing a solution to the optimisation problem. The movement of each particle in the search area, is determined by the 'position update rule' (equation 1.6), the fundamental aspect of the *PSO* algorithm (Slade *et al.*, 2004).

$$\vec{x}_i(t+1) = \vec{x}_i(t) + \Delta\vec{x}_i(t+1)$$

$$\Delta\vec{x}_i(t+1) = \chi\left(\Delta\vec{x}_i(t) + \Phi_1\left(\vec{x}_{i,best}(t) - \vec{x}_i(t)\right)\right) + \Phi_2\left(\vec{x}_{G,best}(t) - \vec{x}_i(t)\right)\Big) \quad (1.6)$$

where,

$$\Phi_m = c_m \begin{bmatrix} r_{m,1} & 0 & 0 & 0 \\ 0 & r_{m,2} & 0 & 0 \\ 0 & 0 & O & 0 \\ 0 & 0 & 0 & r_{m,D} \end{bmatrix}$$

where $\vec{x}_{i,best}(t)$ is the individual best position of the 'individual' and $\vec{x}_{G,best}(t)$ is the best position of the entire swarm, c_1 and c_2 represent weighting factors for the individual and global best positions, respectively. The $r_{m,j}$ represents random scalars between 0 and 1. The $\Phi_2\left(\vec{x}_{G,best}(t) - \vec{x}_i(t)\right)$ term refers to a 'social influence' and draws the 'individual' to the globally best solution (the swarm), whereas $\Phi_1\left(\vec{x}_{i,best}(t) - \vec{x}_i(t)\right)$ represents the 'individual' particle 'thinking' for itself. A change in direction $\Delta\vec{x}_i(t+1)$ is due to the inertial component $\Delta\vec{x}_i(t)$, the directional movement of the swarm (neighborhood) best $\vec{x}_{G,best}(t)$ and the directional movement of the 'individual' best, $\vec{x}_{i,best}(t)$ (figure 1.3) (Slade *et al.*, 2004). Slade *et al.* (2004) compared the performance of genetic algorithms and particle swarm optimisation for the inversion of ocean colour observations, with particle swarm optimisation performing the best and being the more expedient of the two methods.

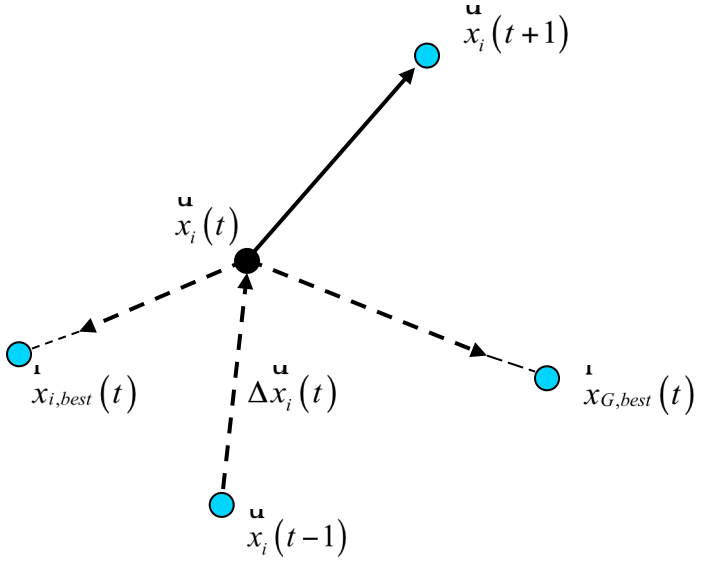

Figure 1.3: This is a pictorial representation of how the *PSO* procedure behaves based on the trajectory of the individual particles (Slade *et al.*, 2004).

d) Neural Networks

Artificial neural networks (*ANN*) such as the one represented in figure 1.4, consist of many inputs. The number of individual inputs (R) are weighted (W) in the weight function matrix, before going into the transfer function f, where n is the net input of the summed weighted inputs and bias b (Hagan et al., 1996). *ANNs* require to be trained before use. If a single neuron with multiple inputs is insufficient, layers of S neurons can be generated (Figure 1.5). Such *ANNs* can be used to determine water constituent properties, such as *CHL* from R_{rs} spectra (Ressom et al., 2006). Schiller and Doerffer (1997) used neural networks to determine *OSM* concentrations from remote sensing reflectances. They trained their network with pre-calculated R_{rs} data that covered a predefined *OSM* range. Their inversion algorithm performed well and showed accurate retrieval for *OSMs*. However, the initial training of neural networks requires a significant amount of time and a large data set which requires the time burden and expense of *in situ* data collection (Kempeneers et al., 2005).

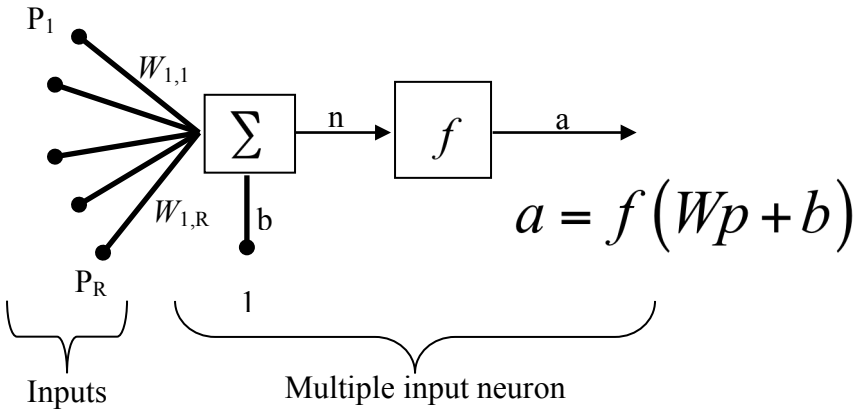

Figure 1.4: A multiple input neuron (Hagan *et al.*, 1996).

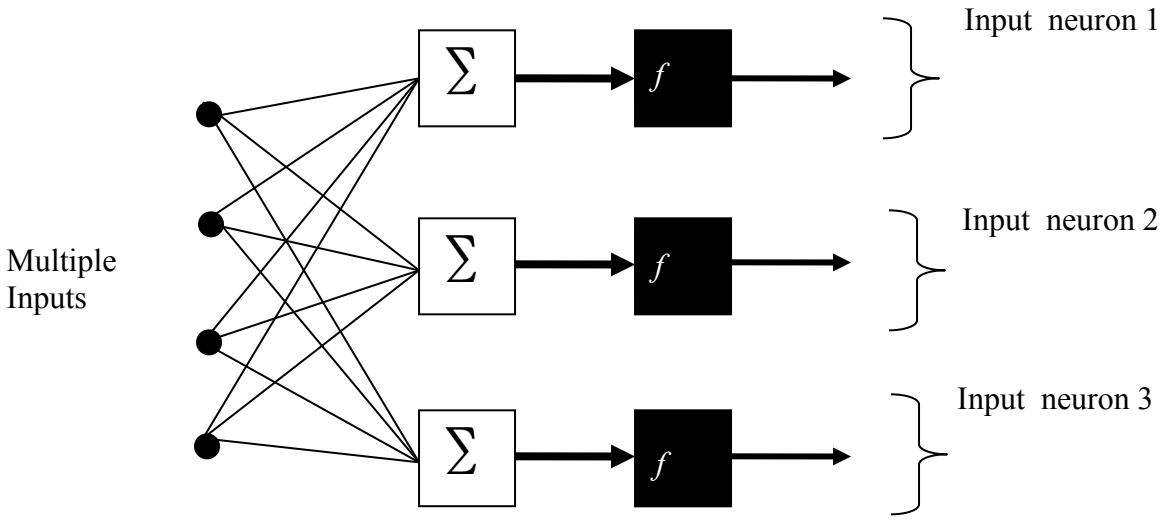

Figure 1.5: A multiple input neuron in multiple layers (Hagan *et al.*, 1996).

In comparison to a *LUT* approach, the above techniques, including neural networks and genetic algorithms, require a significant construction effort and are dependent on specific data sets. Consequently, if the database has to be changed for any reason, the time consuming process of generating a new data set and retraining the neural network will have to be repeated. In contrast, *LUT*s can be generated rapidly and at a high resolution for specific geographical regions (Philpot et al, 2004). From this point forward only simple methods of spectral matching shall be considered in an attempt to avoid the computational burden associated with more complex ocean colour inversion approaches.

1.4 Review of current technologies for satellite remote sensing

Remote sensing technology is an important asset for oceanographers and Earth scientists. It can provide investigators with information on costal ecosystems as well as the data required to interpret ocean colour and monitor coastal environments (Hayes *et al.*, 2010). Technology for the remote sensing of coastal regions is dominated by sensors that enable coverage of large geographical areas at relatively low resolution. Such sensors include: The Ocean Color and Temperature Sensor (*OCTS*), Sea-viewing Wide Field-of-view Sensor (*SeaWiFS*), Moderate Resolution Imaging Spectro-radiometer (*MODIS*), Global Imager (*GLI*), and Medium Resolution Imaging Spectrometer (*MERIS*). These sensors are used for the development of ocean colour inversion algorithms and ocean colour interpretation, with *SeaWiFS* delivering what is believed to be the highest quality ocean colour data until the mission was terminated in 2011 (McClain, 2009).

OCTS was in commission from 1978 to 1986 and contributed significantly to ocean sciences. *OCTS* offered the necessary means for scientists to begin to understand ocean processes and propelled the advancement of oceanography by providing the optics community with an invaluable data set. The objective of the *SeaWiFS* sensor was to monitor global changes in oceanic processes as well as the influence that such processes have on the global carbon and biogeochemical cycles. *SeaWiFS* data can be used to monitor spring blooms and track populations of phytoplankton and their primary production. The *MODIS* sensor benefited from the knowledge and experience gained in the *SeaWiFS* project and is carried on the Terra and Aqua satellites. This assemblage allows the surface of the earth to be viewed every 1 to 2 days, measuring in 36 spectral bands. The *MERIS* sensor, onboard the Envisat satellite launched by the European Space Agency (*ESA*) in February 2002, measures the Earth's reflection of solar radiation in 15 spectral bands, obtaining a global image every three days. The primary objective of *MERIS* is the measurement of ocean colour, chlorophyll and sediments for the

understanding of the ocean carbon cycle. These sensors were designed and built to enhance knowledge and understanding of ocean processes and dynamics for the purpose of developing earth system models that can accurately predict global changes. Correct information is important to allow governments and councils to make the right decisions when dealing with environmental and climate issues McClain, 2009). Table 1.1 details a list of the current and future sensors that are used for ocean colour modeling.

Sensor/Satellite	**Agency**	**Launched**	**Swath (km)**	**Spatial Resolution (m)**	**Bands (Visible/total)**	**Spectral Coverage**
MODIS/Terra 1	NASA (USA)	1999	2330	250/500/1000	9/36	405-14385
OCM-/IRS-P4-2	ISRO (India)	1999	1420	360/4000	7/8	412-885
MERIS/2	ESA (Europe)	2002	1150	300/1200	12/15	412-1050
MODIS/Aqua 1	NASA (USA)	2002	2330	250/500/1000	9/36	405-14385
OCM-2/Oceansat2/2	ISRO (India)	2009	1420	360/4000	7/9	400-900
VIIRS/NPP/1	NOAA/NASA (USA)	2011	3000	370/740	22	412-11800
OLC1/Sentinel-3A/2	ESA/EUMETSAT (Europe)	2013	1270	300/1200	21	400-1020
S-GLI/GCOM-C	JAXA (Japan)	2014	1150-1400	250/1000	19	375-12500
VIIRS/JPSS/1	NOAA/NASA (USA)	2016	3000	370/740		412-11800
OLC1/Sentinel-3B/2	ESA/EUMETSAT (Europe)	2017	1265	260	21	390-1040
PACE/2	NASA (USA)	2019				
VIIRS/JPSS1/1	NOAA (USA)	2019	3000	370/740	22	412-11800
ACE/2	NASA (USA)	202X		1000	Hyperspectral	350-2130
HyspIRI	NASA (USA)	Unk	600	60	Hyperspectral	380-2500

Table 1.1. Ocean Colour Sensors in space (extracted from National Research Council. *Assessing Requirements for Sustained Ocean Color Research and Operations*).

Improving the quality of remote sensing data is paramount to the successful implementation of ocean colour algorithms. The following proposed advancements are likely to provide such an opportunity and present the future of ocean colour science as an exciting prospect (McClain, 2009):

1. Hyperspectral sensors: The introduction of additional information using hyperspectral data may improve retrieval and correction algorithms.
2. Geostationary platforms: These have the potential to significantly improve data for regions which are persistently cloudy and therefore increase the frequency in which images can be obtained for a region. The Hyperspectral Environmental Suite (*HES*) and the Korea Geostationary Ocean Colour Imager (*KGOCI*) are potential geostationary platforms.
3. Smaller satellites: These are easier to launch than the larger satellites and therefore, if hardware advancements are continued to the point where data quality matches that of the larger satellite outputs, ocean colour satellites will become cheaper and faster to design and launch.
4. Unmanned airborne vehicles (*UAV*): Due to the current predominant use of *UAVs* for military applications, this technology is expensive. However, *UAVs* offer potentially very high spatial resolutions of specified regions.

Remote sensing provides temporal coverage that can be used in conjunction with *in situ* measurements of optical properties. *In situ* measurements of ocean properties can also be made using autonomous underwater vehicles (*AUVs*) (McClain, 2009).

1.5 Outline of Thesis

The topics covered in this thesis, and their distribution between chapters are shown below:

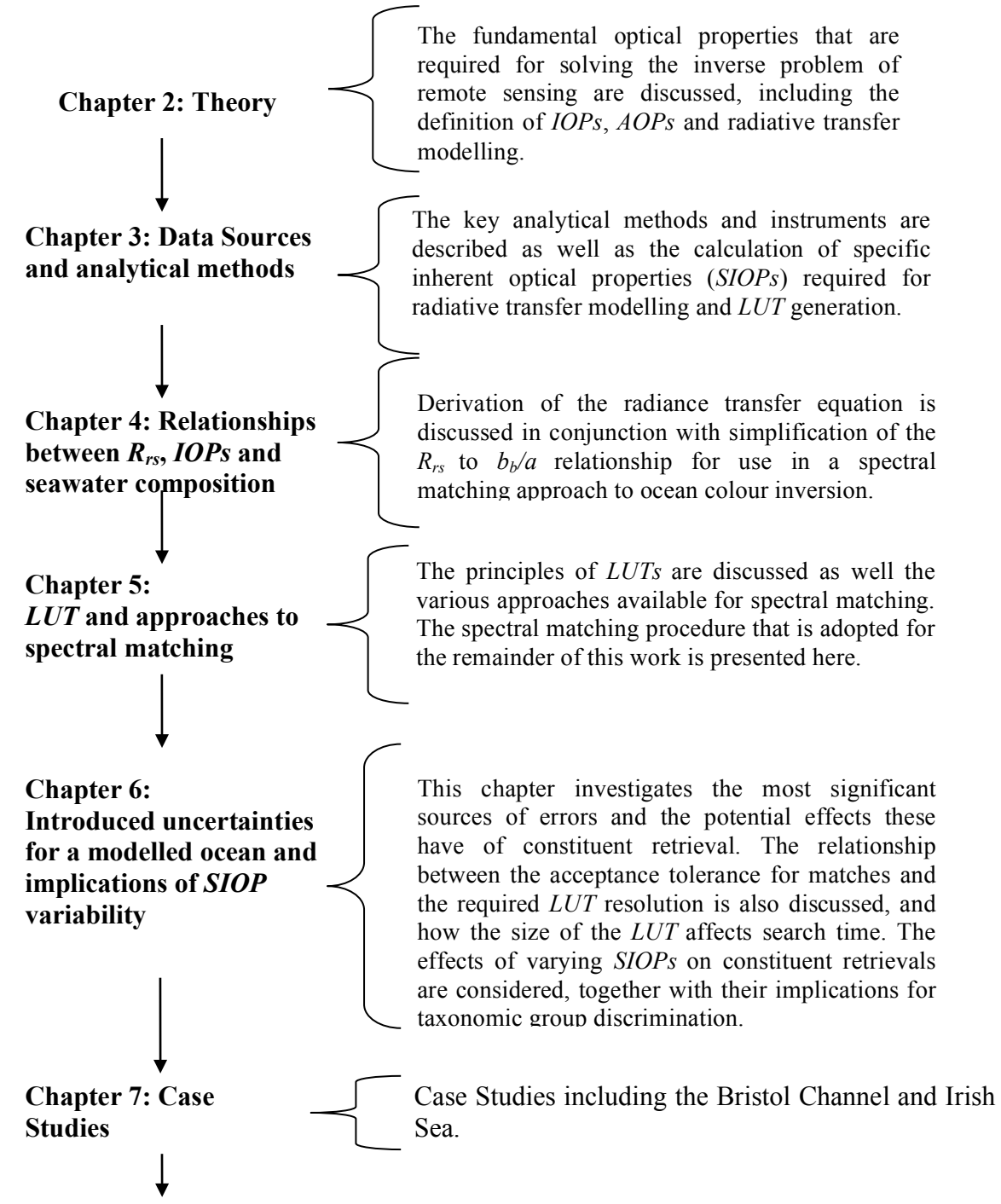

Chapter 2

Optical Theory

The absorption ($a(\lambda)$), scattering ($b(\lambda)$) and backscattering coefficients (b_b (λ)) are inherent optical properties (*IOPs*) which, in conjunction with the volume scattering function (β), control the way in which light propagates in natural water (Preisendorfer, 1961). These properties depend only on the medium and are independent of the ambient light field, i.e. radiance distribution variations, within the water (Mobley, 1994; Preisendorfer, 1961). In addition to water itself, the main optically significant materials (*OSMs*) in coastal (case 2) waters are suspended mineral particles, phytoplankton cells and coloured dissolved organic matter (*CDOM*). These are conventionally measured using proxy variables: phytoplankton cells are measured as chlorophyll-*a* concentration, *CHL*; suspended mineral particles are measured as the dry weight of mineral suspended solids per unit filtered volume, *MSS,* and dissolved coloured organic material is measured as the absorption coefficient of filtered samples at 440 nm, *CDOM* (Kirk, 1983; Spinrad *et al.*, 1994; Bukata, 1995). The coefficients of radiance and irradiance attenuation are apparent optical properties (*AOPs*) which, unlike *IOP*s, are not independent of changes in the radiance distribution (Preisendorfer, 1961). The behaviour of light and its interaction with water depends on the detailed characteristics of the optically significant materials, such as the Particle size distribution (*PSD*), shape, composition and index of refraction (n) of the suspended particles. Due to the variability of particle morphology and composition, the same mass concentration of particles in the ocean can produce a large variation in the *IOPs*, particularly the scattering and the backscattering coefficients. Understanding the variability of such characteristics is fundamental for ocean colour remote sensing, (Kirk, 1983; Spinrad *et al.*, 1994; Bukata, 1995; Jerlov, 1968). When considering coastal zones, the water generally has a high

turbidity due to the presence of uncorrelated concentrations of inorganic and dissolved material. Consequently, empirical methods that develop statistical relationships between reflectance and optical properties can be unreliable in such optically complex waters. For example, Morel and Gordon (1980) introduced an empirical method for the estimation of constituent concentrations of seawater through reflectance measurements taken from case 1 waters where optical properties are dominated by phytoplankton and its associated products. This empirical method enabled the retrieval of phytoplankton concentrations from clear water, but the authors found that such algorithms can be ambiguous in coastal zones (case 2 waters) where processes such as runoff or wind induced sediment re-suspension may be an influential factor (Morel and Gordon, 1980). Statistical relationships are more reliable in the open ocean, where phytoplankton and phytoplankton related products are the main contributors to *IOP* variability. For case 2 waters, it appears that relationships between the *IOPs* and the reflectance are best established through semi-analytical algorithms based on radiative transfer theory (Wernand *et al.*, 2008; Garver and Siegel, 1997). As light propagation is strongly influenced by the absorption, scattering and backscattering by the suspended particles it is important that appropriate values of these coefficients are used. The following chapter will:

1. Define *IOPs*, *AOPs* and the radiative transfer equation that can be used to describe the propagation of light in seawater.

2. Describe the radiometric quantities used to measure ocean colour: irradiance reflectance, radiance reflectance, remote sensing reflectance and normalised water-leaving radiance.

3. Introduce numerical models for solving the radiance transfer equation with focus on the spectral characteristics of the *IOPs*.

4. Present the basic requirements for analytical modelling of ocean colour.

2.1 Inherent Optical Properties (*IOPs*)

Consider a collimated beam of monochromatic light incident at right angles on an infinitesimally thin layer of water, of thickness *dr* (Figure 2.1).

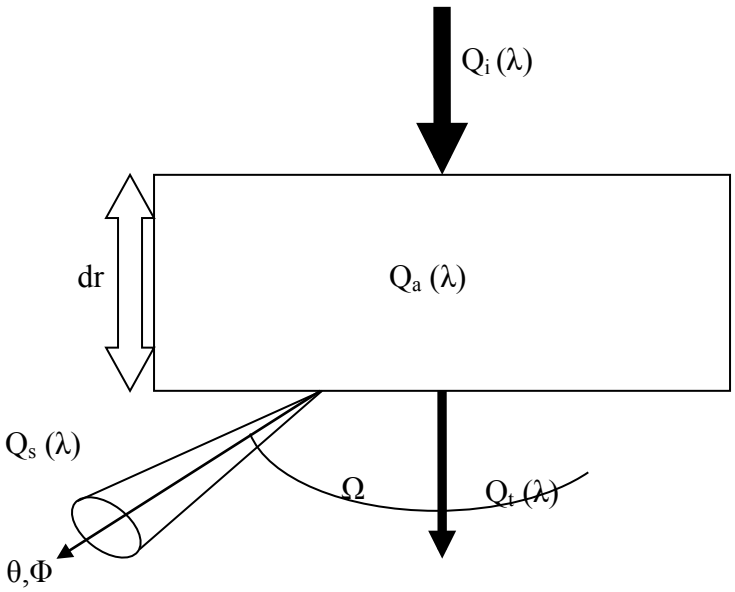

Figure 2.1: Diagrammatic representation of the interaction of a beam of monochromatic light incident at right angles on an infinitesimally thin layer of water (adapted from Mobley, 1994).

The illuminating beam has a spectral radiant power Q_i (λ), W nm^{-1}. The spectral absorptance, A (λ) is defined as the fraction of Q_i (λ) that is absorbed, Q_a (λ) by the medium (Mobley, 1994):

$$A(\lambda) = Q_a(\lambda) / Q_i(\lambda) \qquad (2.1)$$

The spectral scatterance, B (λ), is defined as the fraction of Q_i (λ) that is scattered out of the collimated beam, Q_s (λ).

$$B(\lambda) = Q_s(\lambda) / Q_i(\lambda) \qquad (2.2)$$

The remaining spectral radiant power is transmitted Q_t (λ), with no directional change and is referred to as the transmittance:

$$T(\lambda) = Q_t(\lambda) / Q_i(\lambda) \tag{2.3}$$

A, *B* and *T* are the fraction of incident power absorbed, scattered and transmitted, respectively. The sum of *A* and *B* is the attenuance, *C*, which is the combined fractional loss due to absorption and scattering from the incident beam. The *IOPs* predominantly used in ocean optics are the spectral absorption coefficient, $a(\lambda)$, spectral scattering coefficient, $b(\lambda)$ and spectral beam attenuation coefficient, $c(\lambda)$. They are defined as follows (Mobley, 1994; Kirk, 1983):

$$a(\lambda) = \lim_{dr \to 0} A(\lambda) / dr \ \ (\mathrm{m}^{-1}) \tag{2.4}$$

$$b(\lambda) = \lim_{dr \to 0} B(\lambda) / dr \ \ (\mathrm{m}^{-1}) \tag{2.5}$$

$$c(\lambda) = a(\lambda) + b(\lambda) \quad (\mathrm{m}^{-1}) \tag{2.6}$$

The angular distribution of Q_s is described by expressing the angular scatterance as a function of distance and unit solid angle, from which the volume scattering function (*VSF*) of the medium, $\beta(\phi, \lambda)$, as *dr* approaches 0 and $d\Omega$ approaches 0, can be derived (Mobley, 1994; Kirk, 1983);

$$\beta(\phi,\lambda) = \lim_{dr \to 0} \lim_{d\Omega \to dr} \frac{Q_s(\phi,\lambda)}{Q_i(\lambda) dr d\Omega} \tag{2.7}$$

where, $d\Omega$ is the solid angle. The shape of the *VSF* is often expressed as the scattering phase function ($\dot{\beta}$):

$$\dot{\beta}(\phi,\lambda) = \frac{\beta(\phi,\lambda)}{b(\lambda)} \ (\mathrm{sr}^{-1}) \tag{2.8}$$

Note that the *IOPs* defined above are dependent only on the composition of the medium and not on the properties of the light field.

2.2 Specific Inherent Optical Properties (*SIOPs*)

Coastal regions can exhibit large spatial and temporal variability in their optical properties (Aurin *et al.*, 2005) and it is frequently necessary to calculate the absorption, scattering and backscattering properties of the water body of interest (Brando and Dekker, 2003). This requires appropriate use of specific inherent optical properties *(SIOPs)* for the optically significant materials (*OSMs*). The total *IOPs* of a given volume of water can be expressed as the sum of the products of the concentrations of the *OSMs* and their *SIOPs*. This is written as:

$$a(\lambda) = a_w(\lambda) + \left(a^*_{chl}(\lambda) \times CHL\right) + \left(a^*_{mss}(\lambda) \times MSS\right) + \left(a^*_{cdom}(\lambda) \times CDOM\right) \quad (2.9)$$

$$b(\lambda) = b_w(\lambda) + \left(b^*_{chl}(\lambda) \times CHL\right) + \left(b^*_{mss}(\lambda) \times MSS\right) \quad (2.10)$$

$$b_b(\lambda) = b_{b,w}(\lambda) + (b^*_{b,chl}(\lambda) \times CHL) + (b^*_{b,mss}(\lambda) \times MSS) \quad (2.11)$$

It is common for an asterisk (*) to designate *SIOPs*, so that a^*_{chl}, a^*_{mss} and a^*_{cdom} are the specific inherent absorption by phytoplankton, suspended minerals and coloured dissolved organic matter , b^* and b_b^* represent specific scattering and backscattering, and *CHL*, *MSS* and *CDOM* represent the constituent concentrations.

2.3 Apparent Optical Properties (*AOPs*)

Apparent optical properties (*AOPs*) depend on both the optical characteristics of the medium (*IOPs*) and the directional structure of the ambient light field (Mobley, 1994). The direction of photons in a light field is characterised by the zenith (θ) and azimuth (Ψ) angles (figure 2.2). Backscattering, or in some cases, multiple forward scattering, causes a fraction of incident photons to be returned across the water air boundary. However, not all light that is backscattered exits the water. The fraction that does is detected in remote sensing as the water leaving radiance (L_w) (Kirk, 1983; Mobley, 1994; Spinrad *et al.*, 1994; Bukata, 1995).

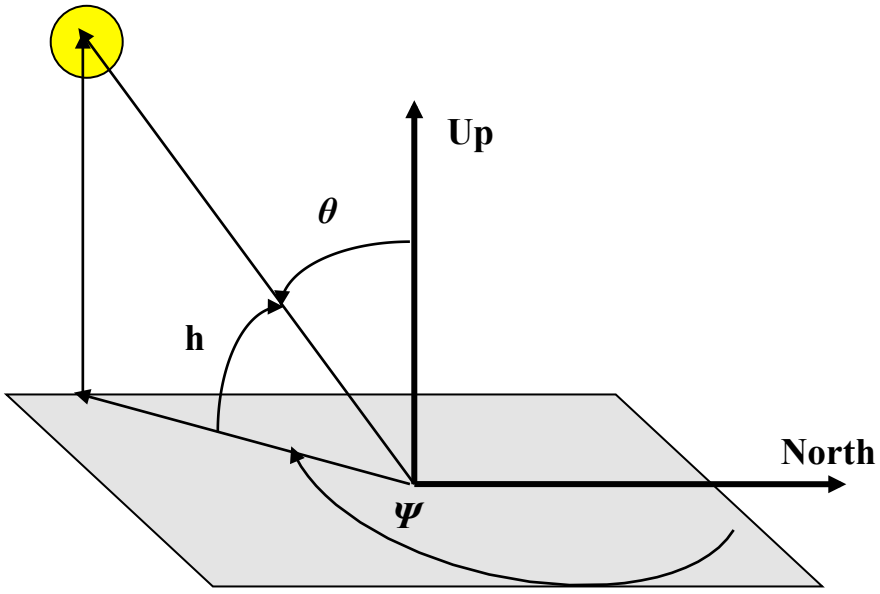

Figure 2.2: The zenith angle (θ), is measured from the vertical (up), the azimuth angle (Ψ), is measured clockwise from North and the elevation, h, is measured up from horizon.

The radiant flux (Φ ,W) specifies the transfer of radiant energy (Q, J) per unit time in a given direction (θ,Ψ). The radiant intensity (I) is the measure of the Φ per unit solid angle in a specified direction (Kirk, 1983; Mobley, 1994):

$$I = \frac{d\Phi}{d\Omega} \text{ (W sr}^{-1}\text{)} \tag{2.12}$$

The radiance, L (W m^{-2} sr^{-1}), from a point in a surface is defined as the radiant flux per unit solid angle, per unit projected area of a given area (dS), in a given direction L (θ, Ψ) (Kirk, 1983):

$$L(\theta,\Psi) = \frac{d^2\Phi}{dS\cos\theta d\Omega} \text{ (W m}^{-2}\text{ sr}^{-1}\text{)} \tag{2.13}$$

where cos θ is the cosine of the zenith angle. Horizontal variations in the environment and in the optical properties of seawater are usually much less than vertical variations (Mobley, 1994). Therefore, radiance signals are often defined as a function of depth (z) only. The radiant flux crossing an element of surface dS is the irradiance, E (W s^{-1} m^{-2}):

$$E = \frac{d\Phi}{dS} \text{ (W}^{1}\text{ m}^{-2}\text{)} \tag{2.14}$$

The planar irradiance due to downwelling light (E_d) and upwelling light (E_u), are defined as follows:

$$E_d = \int_{2\pi} L(\theta,\Psi)\cos\theta d\Omega \tag{2.15}$$

$$E_u = -\int_{-2\pi} L(\theta,\Psi)\cos\theta d\Omega \tag{2.16}$$

where downward and upward irradiances at a point on the surface are integrated with respect to solid angle (Ω) over the whole upper and lower hemispheres, respectively (Kirk, 1983; Bukata *et al.*, 1995). E_d is the integral of the radiance, weighted by the

cosine of the zenith angle over the upper hemisphere. E_u is the integral of the radiance, weighted by the cosine of the nadir angle (π-θ), over the lower hemisphere (Morel and Smith, 1982). Scalar irradiances are the integrals of the radiance distribution over the upper and lower hemisphere without the cosine weighting (Morel and Smith, 1982) and are defined as:

$$E_0 = \int_{4\pi} L(\theta,\psi)\, d\Omega \tag{2.17}$$

$$E_{0d} = \int_{2\pi} L(\theta,\psi) d\Omega \tag{2.18}$$

$$E_{0u} = -\int_{2\pi} L(\theta,\psi) d\Omega \tag{2.19}$$

where, $d\Omega$ equals cos θ sin θ d θ. The average cosine, $\bar{\mu}$, is the ratio of the net downwards irradiance to scalar irradiance:

$$\bar{\mu} = \frac{\overset{\mathbf{u}}{E}}{E_0} = \frac{E_d - E_u}{E_0} \tag{2.20}$$

This ratio helps to specify the angular distribution of the light field and indicates that the average cosine is equal to the net downward irradiance divided by the scalar irradiance (Kirk, 1983; 1991; Morel and Smith, 1982). The average cosine may be regarded as the average value of the cosine of the zenith angle of all photons for the total light at a specific point in the light field in an infinitesimally small volume element (Kirk, 1983). The reciprocals of the average cosine for upwelling and downwelling light, $\frac{1}{\bar{\mu}_u}$ and $\frac{1}{\bar{\mu}_d}$ respectively, are proportional to the mean path length per vertical meter of the upward or

downward flux of photons (per unit of horizontal area per second) (Kirk, 1991). Some of the important *AOPs* discussed here and their derivations are listed in table 2.1. The diffuse attenuation coefficients, represented by the symbols K, K_d, and K_u, essentially provide an estimate of the turbidity of the water by measuring the attenuation of irradiance with depth (Mobley, 1994).

Quantity	SI units	Symbol	Equation
Irradiance reflectance	Dimensionless	$R(\lambda)$	$R = \frac{E_u(\lambda)}{E_d(\lambda)}$
Radiance reflectance	sr^{-1}	$R_{rs}(\lambda)$	$R_{rs}(z,\lambda) = \frac{L_u(z,\lambda)}{E_d(z,\lambda)}$
Diffuse attenuation coefficient of radiance $L(z;\theta,\psi)$	m^{-1}	$K(z,\lambda)$	$K(\theta,\Psi) = -\frac{1}{L(z,\lambda)}\frac{dL(z,\lambda)}{dz}$
Diffuse attenuation coefficient of downward irradiance $E_d(z,\lambda)$	m^{-1}	$K_d(z,\lambda)$	$K_d = -\frac{1}{E_d(\lambda)}\frac{dE_d(\lambda)}{dz}$
Diffuse attenuation coefficient of upward irradiance $E_u(z,\lambda)$	m^{-1}	$K_u(z,\lambda)$	$K_u = -\frac{1}{E_u(\lambda)}\frac{dE_u(\lambda)}{dz}$

Table 2.1: *AOP* symbols, terms and derivations (Mobley, 1994).

2.4 Radiative Transfer Equation

Integro differential equations of radiative transfer are used to describe the propagation of light in the ocean. The radiative transfer equation (*RTE*), which establishes the relationships between *IOPs* and *AOPs*, is defined as follows (Kirk, 1983):

$$\frac{dL(z,\theta,\Psi)}{dr} = -cL(z,\theta,\Psi) + L^*(z,\theta,\Psi) \tag{2.21}$$

with units as follows:

$$\left\{ \begin{array}{l} \dfrac{dL(Wm^{-2}sr^{-1}nm^{-1})}{dr(m^{-1})} : Wm^{-3}sr^{-1}nm^{-1}(L.H.S) \\ \\ c(m^{-1}), L(Wm^{-2}sr^{-1}nm^{-1}) : Wm^{-3}sr^{-1}nm^{-1}(R.H.S) \end{array} \right\}$$

where L (z, θ, Ψ) represents the radiance at depth z, with angular coordinates (θ, Ψ) accounting for the direction of the photon beam. The rate of change of radiance with distance r, is represented by dL/dr and the path is specified by zenith and azimuth angles at depth z. The term, $-cL$ (z, θ, Ψ) accounts for the loss of photons as a result of attenuation, c, whereas, L^* (z, θ, Ψ) represents the gain in radiance (over dr) by scattering from adjacent paths. (Kirk, 1983; Spinrad *et al.*, 2004). This term can be expanded as

$$L^*(z, \theta, \Psi) = \int_{4\pi} \beta(z,\theta,\Psi;\theta',\Psi')L(z,\theta',\Psi')d\Omega(\theta',\Psi') \tag{2.22}$$

with units as follows:

$$\left\{ L(Wm^{-3}sr^{-1}nm^{-1}) : \beta(sr^{-1}m^{-1}) * L(Wm^{-2}sr^{-1}nm^{-1}) * d\Omega(sr) \right\}$$

$\beta(z,\theta,\Psi;\theta',\Psi')$ indicates scattering from one direction (θ,Ψ) to another direction (θ',Ψ') and $L(z,\theta',\Psi')$ is the radiance value in the direction from which the scattering originates. The radiative transfer modeling programme, Hydrolight, is used in this work for the numerical solution of problems involving the *RTE*.

2.5 Optical properties of natural waters

Many inversion algorithms depend on accurate spectral descriptions of the absorption, scattering and backscattering coefficients of water constituents (Lee *et al.*, 2002). Consequently, the following sections describe the spectral characteristics of absorption, scattering, backscattering and the backscattering to scattering ratio.

a) The absorption coefficient

The absorption of underwater light can be analysed by separating the total absorption into the contributions by individual components (Cannizzaro *et al.*, 2008; Chami *et al.*, 2006; Gallegos, 2005). Since the absorption by the different constituents is additive. the total absorption as a function of wavelength can be written (Kirk, 1983):

$$a_{total}(\lambda) = a_{ph}(\lambda) + a_{TSM}(\lambda) + a_{CDOM}(\lambda) + a_{w}(\lambda) \tag{2.23}$$

where the subscripts *ph*, *TSM*, *CDOM* and *w* represent phytoplankton, total suspended material (*TSM*), *CDOM* and water, respectively (Cannizzaro *et al.*, 2008; Doxaran *et al.*, 2009). Values for a_w are commonly taken from Pope and Fry (1997). The optical characteristics of the main components are described below.

Phytoplankton absorption

The absorption due to phytoplankton can be determined using the quantitative filter technique (Yentsch 1962). If pigments are extracted from the filtered material by organic solvents (e,g, Kishino et al., 1985) or bleached using sodium hypochlorite (Tassan and Ferrari 1998), the phytoplankton absorption coefficient, a_{ph} is obtained by subtracting the non-algal particle absorption (a_{na}) from the total absorption (a_t):

$$a_{ph}(\lambda) = a_{t}(\lambda) - a_{na}(\lambda) \tag{2.24}$$

This technique has a degree of uncertainty due to the requirement for path length amplification correction (β) due to the highly scattering nature of the filter (Tassan and Ferrari 1998, Lohrenz 2000).

Kishino *et al.* (1985) investigated three cultured phytoplankton species (using methanol extraction). They found typical phytoplankton absorption spectra to have peaks due to chlorophyll absorption in the blue (430 nm) and red (675 nm) with relative minima between 550 nm (*Dunaliella tertiolecta*) and 600 nm (*Skeletonema costatum*) depending on species. The authors noted that the efficiency of extraction of photosynthetic pigments by the methanol method was as high as 95.5% for some cultured species.

CDOM absorption

CDOM is a significant contributor to light absorption in coastal regions, absorbing strongly at blue wavelengths. Jerlov (1957) first suggested that an exponential function of wavelength could be used to describe the *CDOM* absorption spectrum:

$$a_{cdom}(\lambda) = a_{cdom}(\lambda_r) e^{-\gamma(\lambda_r - \lambda)} \tag{2.25}$$

where γ is the slope of $a(\lambda)$ and λ_r is a reference wavelength (Aas *et al.*, 2005, Bricaud 1981). Extensive studies of *CDOM* absorption have shown that the coefficient for the spectral slope can vary from 0.01 to 0.02, with the majority of the values falling between 0.012 and 0.015 (Binding *et al.*, 2003; Bricaud *et al.*, 1981; Carder *et al.*, 1981).

Mineral particle absorption

The specific absorption coefficient for suspended minerals (*MSS*) can be derived from spectrophotometric absorption measurements on filtered material following extraction or

bleaching of phytoplankton pigments. *MSS* absorption spectra usually have a similar exponential shape to *CDOM* but with a smaller spectral slope and generally smaller numerical value (Brown, 2010).

Spectrophotometer measurements by Binding *et al.* (2003) for mineral particles in the Irish Sea show that the specific absorption coefficient of *MSS* (a^*_{MSS}) increases steadily from red wavelengths to the blue wavelengths in accordance with a power law function, accounting for 98% of the spectral variation in a^*_{MSS}:

$$a^*_{MSS} = 3\times10^7 \lambda^{-3.2439} \tag{2.26}$$

On the other hand, the data in Neil *et al.* (2011) suggests an equation of the form

$$a^*_{MSS} = 7\times10^{12} \lambda^{-5.3} \tag{2.27}$$

for mineral particles in the same region. The discrepancy can probably be attributed to the fact that Neil *et al.* removed organic pigments from their samples by acetone extraction, whereas Binding *et al.* combusted the material at 500^{o}C. Combustion is known to change the absorption properties of mineral particles (Bowers and Binding, 2009).

b) The scattering coefficient

Scattering from suspended particles plays a key role in determining the propagation of light in the water column. Consequently, it is necessary to understand the spectral shape of the scattering coefficient in natural waters, $b(\lambda)$, and the factors that might influence it. The wide variation in the characteristics of the constituent particles in the ocean is one of the factors that makes coastal waters optically complex (Peng *et al.*, 2009).

The total scattering coefficient (b_{tot})(λ) can be separated into contributions from individual components such as water and particulates. *CDOM* is considered a non - scattering substance and is therefore not included (Bricaud *et al.*, 1981). Consequently, the spectral dependence of b_{tot} can be written as:

$$b_{tot}(\lambda) = b_{chl}(\lambda) + b_{sed}(\lambda) + b_{w}(\lambda) \tag{2.28}$$

where b_{chl}, b_{sed} and b_w represent scattering due to chlorophyll, sediment and water respectively. However, the partitioning of scattering between components can be difficult due to the absence of methods for routinely separating different classes of particles in natural hydrosols. Studies conducted by Snyder *et al.* (2008) and Pierson *et al.* (2008), which involved the division of the particulate scattering into organic and inorganic contributions, demonstrated the variability that can occur between geographical locations. (Sun *et al.*, 2010). Further discussion of partitioning total scattering will be given in section 2.6.

Snyder *et al.* (2008) used *in situ* ac-9 measurements to calculate the bulk particulate scattering (b_p(λ)) from:

$$b_p = c - c_{cdom} - a_p \tag{2.29}$$

where, c is the attenuation, c_{cdom} is the attenuation due to *CDOM* and a_p is the particulate absorption. A wavelength proportional scattering correction was applied that assumed a_p (712 nm) is zero and that the scattering phase function is the same at all wavelengths. The authors found that a previous assumption of a wavelength independent phase function is incorrect due to an under-correction of scattering at blue wavelengths (Snyder *et al.*, 2008). Without comprehensive scattering phase function measurements the authors determined that it would be impossible to apply a correction and instead,

they developed a method to estimate this effect using the light scattering correction proposed by McKee *et al*. (2003), in conjunction with a suitable Fournier-Forand phase function. Snyder *et al.* (2008) used a power-law function ($f(\lambda) - f(\lambda/550)^{\gamma}$) to describe the wavelength dependence of $b_p(\lambda)$ spectra. This function incorporates the amplitude at 550nm (f_{550}, in reciprocal metres) and a power law exponent (γ, dimensionless). The application of a power law fit allows a wavelength specific measurement for the average degree of departure from a simple power law form, allowing variation between spectra to be quantified. Consequently, Snyder *et al*. (2008) calculated, at each wavelength, the extent to which each spectrum deviated from the power-law function as a measure of spectral variance. For each wavelength, the measure of the fractional difference (*fd*), i.e. the observed signal from the expected (using the best fit power-law functional form) was calculated as follows:

$$fd(\lambda) = \frac{f_{obs}(\lambda) - f_{pred}(\lambda)}{f_{pred}(\lambda)} \tag{2.30}$$

where f_{obs} is the measured value and f_{pred} is calculated from the power law fit (Snyder *et al*, 2008). Likewise, Defoin-Platel and Chami (2007) calculated scattering due to *Chl-a* and sediment (b_{Chl} and b_{sed}, respectively) using a power law function:

$$b_{chl}(\lambda) = b_{chl}(443)\left(\frac{\lambda}{443}\right)^{-Sbchl} \tag{2.31}$$

$$b_{sed}(\lambda) = b_{sed}(443)\left(\frac{\lambda}{443}\right)^{-S_{bsed}} \tag{2.32}$$

where, S_{Chl} and S_{Sed} are the spectral slopes for *Chl-a* and sediment, respectively. The spectral slope for the particulate scattering was then accurately approximated using nonlinear regression (Defoin-Platel and Chami, 2007):

$$Sb_p = \frac{b_{Chl}(443)Sb_{Chl} + b_{Sed}(443)Sb_{Sed}}{b_{Chl}(443) + b_{Sed}(443)} \quad (2.33)$$

Sun *et al.* (2009) developed a model that could determine the particulate scattering spectra in Lake Taihu, a very turbid and productive lake. Sampling was done at various stations across the lake. They tested 2 types of models for the simulation of scattering spectra, a linear one and a power one. The mean percentage error between the modelled and measured scattering values for the power model was in the range of 0.1% to 4.2% at all wavelengths. The wavelength dependency was found to be similar to other studies: Morel *et al.* (2006) studied the $b_p(\lambda)$ shape in case 2 waters and found that the normalised scattering spectra corresponded approximately to a $\lambda^{-0.6}$ dependency, very similar to the slope of the power model (-0.729) by Sun *et al.* (2009). It is suggested that the similarities of their linear model to a study by Gould *et al* (1999) for case 2 waters supports the generalisation that spectral dependency of $b_p(\lambda)$ generally changes little in some case 2 waters. This conflicts with the conclusions of Snyder *et al* (2008) above, who reported variation in US coastal zones for $b_p(\lambda)$ spectra.

The way in which the spectral shape of the particulate backscattering coefficient has been described by various authors includes:

1. Spectral variations that follow an inverse power-law function (Morel, 1973)

2. The application of a power-law function with spectral slopes varying between 0.1 and 1.4 reproduced the spectral variations in the near infrared b_p spectral shape (Doxaran *et al*, 2009)

3. There is a strong correlation between a decrease in b_p (or b^*p) and high a_p (Babin *et al.*, 2003; and Stramski *et al.*, 2007) when the particle population is dominated by phytoplankton cells.

While there is debate amongst the community as to the shape of the scattering spectra there is also debate with respect to the spatial variability. The work presented here highlights the need for further investigation of this topic, and the standardisation of the methods used would facilitate the development of algorithms based on the information obtained.

Much of the theoretical work on marine light scattering is based on Mie theory. Gustav Mie used Maxwell's equations, complemented by the appropriate boundary conditions, to derive an analytical solution for light scattering by homogenous spherical particles. Mie scattering theory is of interest in ocean optics for the calculation of volume scattering functions (*VSF*) and for the inverse problem of particle size analysis (*PSA*). The implementation of Mie theory to analyse mono or poly-dispersed particles, of a given refractive index (n), is based on a few key assumptions:

1. Particles scatter independently, which requires a distance between spheres of at least three times their radii. This allows the intensities scattered by particles to be added (Van De Hulst, 1957).
2. The wavelengths for the scattered and incident light are the same (elastic scattering).
3. Only spherical and homogenous particles are considered.
4. No multiple scattering is considered as it is assumed the particles are only irradiated by the original beam (Jerlov, 1968).

c) The influence of absorption on the scattering coefficient

Early investigations by Morel (1973) found that, for a mixture of non-absorbing particles that have an identical index of refraction (n) and a *PSD* which follows an inverse power-law function, spectral variations in b (λ) also follow an inverse-power law function. If particle absorption cannot be neglected (for example phytoplankton cells), spectral

variation in scattering by marine particles can be described in terms of normal and anomalous dispersion:

1. Normal dispersion occurs when there is a monotonous decrease in the complex refractive index n, when moving from the ultraviolet part of the spectrum towards the red (i.e. as a function of wavelength) for weakly absorbing particles.

2. Aas *et al* (1996*)* concluded that anomalous dispersion will only influence the scattering properties of small phytoplankton in the vicinity of strong absorption bands. With the algal components, anomalous dispersion is expected to cause a minimum and maximum in scattering efficiencies at the short and long wavelength sides of the chlorophyll c absorption peaks. Gordon *et al*. (2009) found a slight reduction of particulate backscattering in the region influenced by phytoplankton absorption.

Doxaran *et al.* (2009) investigated the influence that light absorption (in the visible spectrum) has on $b_p(\lambda)$ properties, and found a departure from the power law function at wavebands with high absorption. The authors used Mie computations to determine efficiency factors for scattering and absorption (Q_b and Q_a, respectively), calculating the coefficients by integration over the size distribution. Effects of $a_p(\lambda)$ on scattering were shown to significantly increase with decreasing values of n. This is related to variations of Q_a and Q_b with respect to particle diameter. The authors observed a decrease in $b_p(\lambda)$ at short visible wavelengths in the North Sea and Bristol Channel with a discontinuity systematically observed at 440 nm (440 nm corresponds to strong light absorption by phytoplankton). The authors supported their findings with those of Babin *et al.* (2003) and Stramski *et al.* (2007) whose field and laboratory data found a correlation between a decrease in $b_p(\lambda)$ and a corresponding high $a_p(\lambda)$.

On comparison with field data, the relationship between visible and infra-red spectral slopes for $b_p(\lambda)$ is linear (slope close to 1) based on the condition that wavebands with

$a_p(\lambda)$ are avoided (440 nm for example). Doxaran *et al* (2009) claim that in the visible part of the spectrum, the $a_p(\lambda)$ effects on $b(\lambda)$ properties are systematically significant. In their sampled coastal areas, differences on average of 10% and up to 35% were observed at 440 nm between actual $b_p(\lambda)$ values and $b_p(\lambda)$ values modelled using a power-law function fitted onto the near-IR waveband and extrapolated to 440nm. The authors concluded that this departure from the power-law function is almost equal to the $a_p(\lambda)$ when the *PSD* presents a high proportion of coarse particles (ones that follow a Junge size distribution). Smaller particles are poorer absorbers of light, thus, light scattering by sub micrometric particles are less affected by $a_p(\lambda)$. This study allowed them to present a new model for the determination of spectral variations in $b_p(\lambda)$ from the near-IR to visible spectral domains:

$$b_p(\lambda) = b_p(\lambda_{ref})\left(\frac{\lambda}{\lambda_{ref}}\right)^{-\gamma} - \left[1 - \tanh\left(0.5 \times \gamma^2\right)\right] \times a_p(\lambda) \tag{2.34}$$

With λ_{ref} a reference wavelength and γ the spectral slope of $b_p(\lambda)$ in a spectral domain where $a_p(\lambda)$ is almost negligible (near IR). The authors claim this model will accurately correct for $a_p(\lambda)$ effects when marine particles follow a Junge size distribution and that it reproduced field measured $b_p(\lambda)$ with an error lower than 6% (Doxaran *et al*, 2009).

d) The backscattering coefficient

Total scattering, $b_{tot}(\lambda)$ can be partitioned into the spectral forward scattering coefficient, $b_f(\lambda)$ and the spectral backscattering coefficient $b_b(\lambda)$ as follows (Kirk, 1983):

$$b_{tot} = b_b + b_f \tag{2.35}$$

$$b_f = 2\pi\int_0^{\frac{\pi}{2}} \beta(\theta)\sin\theta d\theta \tag{2.36}$$

$$b_b = 2\pi \int_{\frac{\pi}{2}}^{\pi} \beta(\theta) \sin\theta d\theta \tag{2.37}$$

Furthermore, the backscattering coefficient can be separated into water and particle contributions which is expressed as:

$$b_{bp}(\lambda) = b_b(\lambda) - b_{bw}(\lambda) \tag{2.38}$$

where $b_{bw}(\lambda)$ is the backscattering of light due to water, with $b_{bw}(\lambda) = 0.5_{bw}(\lambda)$ (Aas *et al.*, 2005; Carder *et al.*, 2003).

Sources of particulate backscattering in the ocean include gas bubbles, phytoplankton cells, mineral particles, bacteria, viruses and colloids and they vary in size by several orders of magnitude (Stramski *et al.*, 2004). Boss *et al.* (2004) point out that theoretical studies are the predominant source of $b_b(\lambda)$ knowledge, with Mie theory a popular choice for analysis. The solutions to such theoretical studies have shown that particle size, composition and refractive index all affect $b_b(\lambda)$.

While theoretical studies are the predominate source of knowledge, research has been conducted to investigate backscattering properties by more physical means. Maffione and Dana (1997), proposed the use of a fixed angle backscattering sensor for the estimations of backscattering from the *VSF* at 140^o from the forward direction, $\beta(140°)$, and argued that:

$$\frac{b_b}{\beta(140°)} \approx 2\pi 1.08 = 6.79 \tag{2.39}$$

The most accurate measurements are made when there is the least angular variability in the shape of the *VSF*, i.e. between 110° and 160° approximately (Gordon *et al.*, 2009). Following on from this, another parameter of interest is the proportion of backscattering that accounts for the total scattering, i.e. the backscattering ratio: b_{bp}:b_p which will be discussed in the following section.

Physical measurements were also carried out by Loisel *et al.* (2007) who studied three optically distinct regions using an ECO-VSF to measure backward scattering at three angles (100˚, 125˚ and 150°). From this, estimations of the shape of the *VSF* could be made for the backscattering area which in turn enabled b_{bp} to be calculated. The authors also used a Hydroscat-6 to allow comparisons to be made between retrieved values of b_{bp} and the estimated values. Similar results were obtained from the two instruments with values on average only slightly higher (approximately 1.54%) for the Hydroscat-6.

e) The backscattering to scattering ratio

The particulate backscattering to scattering ratio, b_{bp}:b_p, is of fundamental importance in ocean optics.

1. It can provide information on particle size distribution and composition
2. It enables the derivation of approximate phase functions (Loisel *et al.*, 2007; Mobley *et al.*, 2002)
3. It is essential for radiative transfer calculations and is used in many semi-analytical algorithms for *IOP* retrievals (Gordon *et al.*, 1988; Loisel *et al.* 2007; Morel & Maritorena, 2001).

Boss *et al.* (2004) an*d* Mobley *et al*. (2002) compared measured backscattering data (from the coast of New Jersey, USA) with the results of radiative transfer modelling to conclude that the b_{bp}:b_p ratio varied by less than 10% and 24%, respectively. The low spatial variability was also demonstrated by Sun *et al.* (2009) who presented a variety of backscattering ratios from across the globe to document the extent of their variability.

Out of the six areas they documented, five had a b_{bp}:b_p range with a minimum of 0.005, with the maximum of the ranges reaching 0.060. These values represent a contribution of b_b to total scattering of 0.5% and 6%, respectively.

Mobley *et al* (2002) employed a range of Fournier-Forand phase functions to show that the exact choice of phase function in the backscattering direction does not have a great effect on the underwater light field but it is important to use the correct backscatter fraction. Although, the Fournier-Forand phase functions generally gave better agreement with measured quantities than the average Petzold phase function.

Chang and Whitmire (2009) modelled the backscattering ratio using Mie theory. Their work was based upon the assertion by Ulloa *et al.* (1994) that the backscattering ratio can vary strongly with monodispersions or in minerogenic dominated waters. They found that the b_{bp}:b_p ratio was spectrally flat for regions with larger particles and, when the *PSD* slope (ξ) was ≤ 3.25 for all particulate refractive indices (n_p). However, the authors observed spectral variability in the backscattering ratio for all other conditions. This research involved the use of Mie scattering theory and Hydrolight to calculate the *IOPs* for the hypothetical optical water types that varied by n and ξ. They found the accuracy for determination of b_{bp} is dependent on n_p and ξ. whereby, for $1.05 < n_p < 1.15$, the determination of b_{bp} was to within 25% of the true values.

The backscattering ratio has been shown to be an important component in ocean modeling. The following points provide an overview of this section:

1. Boss *et al.* (2004) and Mobley *et al.* (2002) concluded that the b_{bp}:b_p ratio varied by less than 10% and 24%, respectively and that the exact choice of the phase function in the backscattering direction does not have a great effect on the underwater light field.
2. Sun *et al.* (2009) presented backscattering ratios from a wide range of locations to document the extent of variability. Out of the six areas documented, five had a

b_{bp}:b_p ranges with minima of 0.005 and maxima reaching 0.060. These values represent a contribution by b_b to total scattering of 0.5% and 6%, respectively.

3. Chang and Whitmire (2009) found that a power law function could not always be fitted to backscattering spectra and that the b_{bp}:b_p ratio was spectrally flat for regions with larger particles, when the *PSD* slope (ξ) was $\leq$ 3.25, for all particulate refractive indices (n_p) but that the backscattering ratio for all other conditions varied spectrally.

For the purpose of this work, the variation of the phase function with wavelength will be investigated in chapter 4 to determine the extent to which this ratio affects the relationships used for the spectral matching inversion algorithm developed later in this thesis.

2.6 Attributing scattering to different water components

a) A reductionist approach

The heterogeneous nature of oceanic and coastal waters means that to understand the optical interactions, such as scattering and backscattering, it is necessary to separate the contribution of different classes of particulate materials (Martinez-Vicente *et al*, 2010). Stramski *et al.,* (2001) proposed a reductionist approach to this problem in which the *IOPs* are modeled using data for various planktonic species and there is partitioning of *IOPs* into the scattering coefficients of organic material and minerogenic substances (b_o and b_m, respectively). This is a difficult challenge as there are more than 10,000 species of phytoplankton (Jeffrey and Vesk, 1997) of varying shapes, composition, physiologies and sizes. This diverse group includes diatoms, dinoflagellates, cyanobacteria and coccolithophores. While phytoplankton can contain a range of pigments such as chlorophyll-*b* and xanthophylls, chlorophyll-*a* is considered the most important due to its role in photosynthesis (Jeffrey *et al*, 1997). These different characteristics of phytoplankton will affect their optical properties, and the significance of differences between taxa on spectral matching outcomes will be discussed in chapter 6.

The approach of Stramski *et al*. (2002) was a departure from the more traditional method of modeling *IOPs* in oceanic waters, where bio-optical models linked to chlorophyll concentration are used. By considering how specific particulate components affect ocean and coastal water *IOPs*, it potentially gives a better understanding of the variability in optical properties of seawater (Stramski *et al.*, 2001). A major problem arises, however, from the fact that it is not possible to physically separate different classes of scattering particles in a manner analogous to that used for absorption. Such partitioning is particularly important in coastal regions as the high sediment load present in the water column can have a detrimental effect of *Chl* retrieval algorithms. One possible approach was proposed by Stavn and Richter (2008), who investigated the

partitioning of b_p and b_{bp}, in Mobile Bay. The authors developed a multiple linear regression model that could be used to generate specific optical cross sections (using cruise data) that in turn could determine b_m and b_o (scattering due to the mineral, *m* and organic, *o* fractions, respectively). This method relied on the assumption that the composition of mineral matter was the same at each station, with only the concentration varying.

The 'reductionist' approach presented by Stramski *et al* (2001, 2004, 2007) was used by Martinez-Vicente *et al* (2010) to study a coastal station in the Western English Channel. For this region, they hypothesised that particulate scattering could be expressed as follows (a similar one can be used for b_{bp}):

$$b_p = b_{pSPM} = b_{pPOM} + b_{pPIM} = b_{p\varphi} + b_{pPOMnonliving} + b_{pPIM}$$
$$= \sum_{i=1}^{6} b_{ppla,i} + b_{pPOMnonliving} + b_{pPIM} = \sum_{i=1}^{6} C_{ppla,i\sigma b,pla,i} + C_{POMnonliving\sigma b,POMnonliving} + C_{PIM\sigma b,PIM} \quad (2.40)$$

where it is assumed that all scattering is attributed to suspended particulate matter (*SPM*), consisting of organic and inorganic materials (*POM* and *PIM*, respectively). The inorganic materials can consist of biogenic inorganic matter such as coccoliths or diatom frustules. The organic material contribution can also be broken down into phytoplankton contributions ($b_{p\varphi}$) and non-living bacterial particles ($b_{pPOMnonliving}$). However, the phytoplankton contributions can be further divided into the particle scattering coefficient ($b_{ppla,i}$) of the *i*th phytoplanktonic component. Consequently, the mass-specific scattering and backscattering of plankton can be defined in terms of phytoplankton carbon rather than Chlorophyll-*a*. Such an approach is useful because of its potential application to ecosystem models as well as bio-optical models where bio-optically accurate relationships are required for the characterisation of light propagation (Martinez-Vicente *et al*, 2010).

Peng *et al* (2009) documented a development in individual particle analysis (*IPA*) which involves a scanning electron microscope being interfaced with automated image and x-ray analysis (SAX) for the proposed purpose of directly measuring the light scattering features of minerogenic particles, such as the index of refraction, *PSD* and the shape and composition of particles. This technique was used in inland waters, the results of which were used as inputs into Mie theory calculations for minerogenic b and b_b efficiency factors (Q_{bm} and Q_{bbm}, respectively) of individual particles. This enabled the calculation of b_m and $b_{b,m}$. For b_m:

$$b_m(\lambda) = \frac{1}{V}\sum_{I=1}^{N_m} Q_{bm,i}(m_i, \lambda, d_i) PA_{m,i} \tag{2.41}$$

where N_m is the number of minerogenic particles per unit volume of water, $PA_{m,I}$ is the projected area of minerogenic particle i and V is the sample volume. As a development from the original 'reductionist' approach this SAX-Mie procedure can discriminate between sub-classes within the minerogenic component, for example, clay minerals and calcite. The authors tested the estimates generated from the above equation (2.40) using Case 1 empirical bio-optical models to independently estimate b_o and $b_{b,o}$ from the chlorophyll concentration and by comparing the summations of the minerogenic and organic components with bulk measurements of b_p and b_{bp}. An average deviation of 8.2% was observed between results from the two-component model and the observed values from measurements taken in Lake Superior, which is an optically complex fresh water system. They concluded that the model performed reasonably well and that the minerogenic component (in comparison to the particulate component), particularly comprising clay minerals, was more important for the total contribution to b_{bp} than b_p, with $b_{b,m}$ accounting for a variation of 42% to 64% of the bulk measurements over the sites analysed in Lake Superior.

Limitations in the SAX-Mie approach come from the differences that may arise in n for the *PSD*, for example, in the above situation, had montmorillonite been dominant rather

than clay minerals, the estimate of $b_{b,m}$ could have been biased 20% high. Also, Mie theory assumes the particles are perfect spheres. Deviations from a 'perfect' representation causes a shift in the volume scattering function (*VSF*) that will influence light scattered in the backward direction more than the forward. However, the integrated SAX-Mie approach offers great promise for understanding the role of minerogenic particles in influencing the underwater light field and remote-sensing signals, and has the potential to address origins of backscattering in oceanic waters (Peng *et al*, 2009).

b) Remote sensing reflectance and the $b_b(\lambda)/a(\lambda)$ relationship

Ocean colour can be quantified using radiometric measurements such as irradiance reflectance, R or remote sensing reflectance, R_{rs} (Mobley, 1994; Stramski *et al*, 2004). Spectral reflectances depend on the constituents of seawater and their concentrations (Morel, 1974; Stramski *et al*, 2004). In certain circumstances, when inelastic scattering, such as fluorescence and Raman scattering is neglected, the irradiance reflectance (R) just below the surface can be related to the backscattering coefficient (b_b) and absorption coefficient (a) using the apparently simple expression

$$R = \frac{E_u(w)}{E_d(w)} = f_{L,\beta}\frac{b_b}{a} \tag{2.42}$$

where $E_u(w)$ is the upward planar irradiance, $E_d(w)$ the downward planar irradiance in water and the factor $f_{L\beta}$ is a variable function of the radiance distribution and volume scattering function (Morel and Prieur, 1977). It must be pointed out, however, that the $f_{L\beta}$ term incorporates all the complexities associated with radiative transfer in turbid media, and it is rarely possible to derive values for this term analytically. The alternative is to compute values numerically by solving the radiative transfer equation on a case-by case basis. A number of investigations using Monte Carlo techniques (Gordon et al 1975, Morel and Prieur 1977, Kirk et al. 1981) have demonstrated that approximate solutions could be found of the form

$$R \approx C(\mu_0)\,\frac{b_b}{a} \tag{2.43}$$

For this approximation, the term $f_{L\beta}$ is replaced with $C(\mu_0)$ which depends on the mean cosine of the photon distribution just below the surface. $C(\mu_0)$ is strongly correlated with the zenith angle of the refracted solar beam and also varies with the *VSF*.

The subsurface irradiance reflectance expressed in equations 2.43 and 2.44 can be related to the remote sensing reflectance, R_{rs}, as follows

$$R_{rs} = \frac{L_u(a)}{E_d(a)} = \frac{T}{Q}R \tag{2.44}$$

where $L_u(a)$ and $E_d(a)$ are the vertical water-leaving radiance and downward irradiance in air just above the surface, Q is the ratio of upwelling irradiance to radiance just below the surface, and T represents the optical processes involved in light crossing the air-water interface (Mobley, 1999). The combination of equations 2.43 and 2.44 gives

$$R_{rs} = \left[\frac{C(\mu_o)T}{Q}\right]\frac{b_b}{a} \tag{2.45}$$

This expression only holds for a restricted set of conditions, including a fixed solar angle, cloud-free sky and restricted range of values for the inherent optical properties. Under these circumstances, all of the three terms in brackets can be considered as approximately constant (Kirk 1994, Mobley 1999) and it is possible to write the approximation

$$R_{rs} \approx \kappa \frac{b_b}{a} \tag{2.46}$$

The extent to which κ can be considered as a constant of proportionality in practice, varies from case to case and must be established numerically. Nevertheless, equation (2.46) suggests that under typical remote sensing conditions (which include high solar zenith angle and cloud free conditions, R_{rs} is largely a function of the total backscattering and absorption coefficients (b_b and a).

2.7 Summary of chapter 2

- The absorption ($a(\lambda)$), scattering ($b(\lambda)$) and backscattering coefficients (b_b (λ)) are the key inherent optical properties (*IOPs*) which, in conjunction with the volume scattering function (β), control the way in which light propagates in natural water (Preisendorfer, 1961).

- Apparent optical properties (*AOPs*) depend on both the intrinsic optical characteristics of the medium (in this case water) and the directional structure of the ambient light field (Mobley, 1994). Unlike *IOP*s, apparent optical properties (*AOPs*) are not independent of changes in the radiance distribution (Preisendorfer, 1961).

- In addition to water itself, the main optically significant materials (*OSM*) in coastal (case 2) waters are suspended mineral particles, phytoplankton cells and coloured dissolved organic matter (*CDOM*).

- The equation of radiative transfer is used to describe the propagation of light in the water column, and in all non-trivial cases it is solved numerically (e.g. using HydroLight).

- Particles in the ocean affect the way in which the light interacts with the water and consequently, remote sensing reflectance depends on the constituents present in seawater and on their concentrations (Morel, 1974; Stramski *et al.*, 2004). The inherent optical properties for the different constituents are additive. They are defined as a function of wavelength and are obtained from the product of the concentrations of the optically significant constituents and their specific inherent optical properties.

- Total scattering, $b_{tot}(\lambda)$ can be partitioned into the spectral forward scattering coefficient, $b_f(\lambda)$ and the spectral backscattering coefficient $b_b(\lambda)$ (Kirk, 1983), where the backscattering coefficient is usually a small fraction of the total scattering. Theoretical studies can be used to predict the backscattering coefficient and it can be measured to a reasonable degree of accuracy using *in situ* instruments. However, such studies usually involve the assumptions that (1) the particles can be modelled as equivalent spheres and (2) the size distributions can be described by a power law.

- Mineral particles are optically very significant. They can be present in great abundance in the water column and their high refractive index means they scatter light effectively (Wozniak and Stramski, 2004). There is a gradual decrease in the concentration of such minerals when moving from the shoreline out to deeper waters (Wozniak and Stramski, 2004).

- Approximate relationships between remote sensing radiance signals and the backscattering to absorption ratio arise from simplified radiative transfer theory. These relationships will be investigated as a potential way to develop a spectral matching inversion algorithm to recover *OSM* concentrations from remote sensing reflectance signals.

Chapter 3

Data sources and analytical methods

The following chapter provides an overview of the procedures and techniques that were necessary for the construction of a realistic model of radiative transfer in an optically complex water column. This numerical model was required for investigating ocean colour interpretation algorithms based on a simplified relationship between remote sensing reflectance signals and the inherent optical properties (*IOPs*) of the water column. The collection and analysis of field data was not part of the work undertaken for the current project, but since this thesis relies heavily on a pre-existing database of field observations, the underlying methodologies are presented in this chapter. The following topics are therefore addressed:

1. The analytical methods and instruments employed in determining seawater optical properties.
2. The derivation of a set of specific inherent optical properties (*SIOPs)*, calculated from *in situ* data collected from the Western Shelf Sea of the United Kingdom.
3. The mode of operation of the radiative transfer programme Hydrolight, which was used for numerical solution of the Radiative Transfer Equation (*RTE*), enabling relationships between radiance signals and *IOPs* to be established.
4. The approach adopted for the construction of a look-up table (*LUT*) of reflectance spectra for a modelled ocean.

3.1 Cruise Information

The work presented here required the calculation of *SIOPs* that were representative of the Western UK shelf seas. The data used for this purpose was recorded on previous ocean expeditions undertaken by the University of Strathclyde Environmental Optics group. These cruises encompassed 276 stations in the Clyde, Bristol Channel, Irish Sea and Scottish Sea Lochs (Figure 3.1). The instruments deployed included a SeaBird SBE 19 CTD, WET Labs ac-9 absorption and attenuation meter, HOBI Labs HS-2 backscattering meter and Satlantic *SPMR* profiling radiometer.

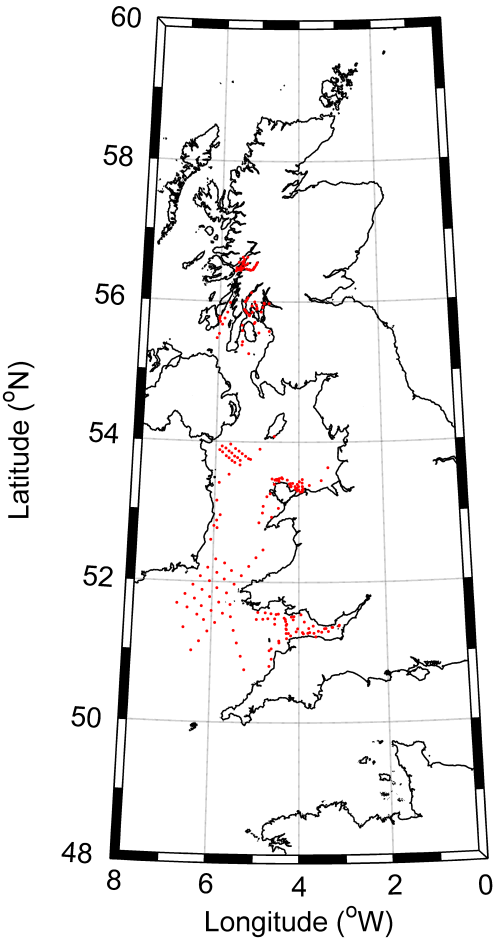

Figure 3.1: The locations of the 276 stations comprising the UK shelf data set (Ian Brown*, Strathclyde University*).

3.2 Key optical instrumentation

a) The ac-9

The *in situ* spectral absorption, $a(\lambda)$, and beam attenuation, $c(\lambda)$, coefficients (at nine wavebands) were measured relative to a pure water blank using a WET Labs *ac-9* absorption and attenuation meter. The scattering coefficient, $b(\lambda)$ was then obtained from:

$$b(\lambda) = c(\lambda) - a(\lambda) \tag{3.1}$$

The *ac-9* has a dual path optical configuration where each channel has its own source, optics and detectors. The optics for the beam performing the attenuation measurement and absorption measurement are shown in figures 3.2 and 3.3. A narrow band spectral output is created when light from a tungsten halogen bulb is collimated and then passed through a band-pass filter that is mounted on a continuously rotating filter wheel. This beam then passes through a beam splitter creating a reflected beam whose intensity is measured by a reference detector and a primary beam which passes into the flow tubes containing the sample of water. The flow tube for the attenuation measurement has a black internal surface which means any scattered light is absorbed and is not included in the measurement of transmitted intensity, and the transmitted beam is refocused through a lens onto the receiver detector after it reaches a second pressure window. The flow tube for the absorption measurement has a glass surface which results in the total internal reflection of forward scattered light that is collected by a diffuser and detector at the end of the tube (WET Labs *ac-9* User's Guide, 2008). Measurements obtained from an *ac-9* require a scattering correction to be applied to the absorption measurements since all the scattered light is not collected in the absorption tube (WET Labs ac-9 User's Guide, 2008).

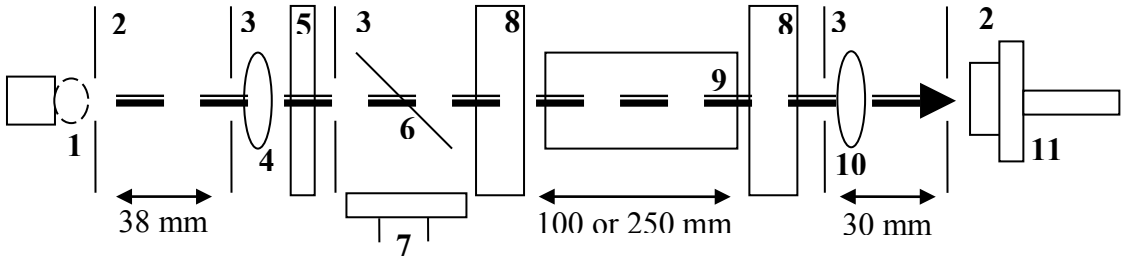

Figure 3.2: The optical path configuration for the measurement of attenuation. 1) Lamp 2) 1 mm aperture 3) 6 mm aperture 4) 38 mm singlet lens 5) Interference filter 6) Beam splitter 7) Reference detector 8) 6 mm quartz pressure window 9) Flow tube 10) 30 mm singlet lens 11) Signal detector (WET Labs ac-9 User's Guide, 2008).

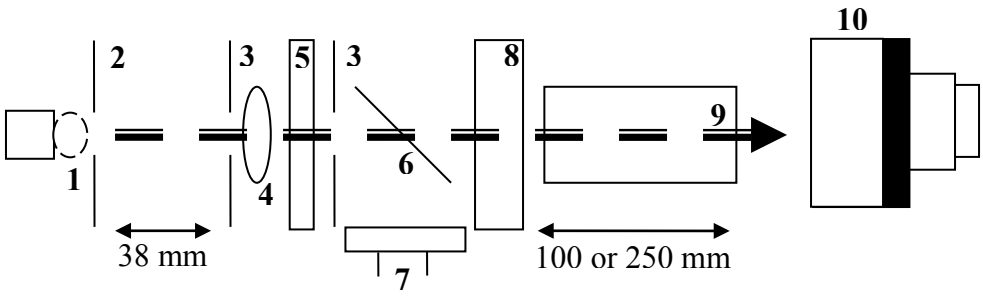

Figure 3.3: The optical path configuration for the measurement of absorption. 1) Lamp 2) 1 mm aperture 3) 6 mm aperture 4) 38 mm singlet lens 5) Interference filter 6) Beam splitter 7) Reference detector 8) 6 mm quartz pressure window 9) Reflective flow tube 10) Signal detector (WET Labs ac-9 User's Guide, 2008).

b) The Hydroscat 2

Optical backscattering was measured at two wavelengths (470 nm and 676 nm) using a HOBILabs HydroScat-2 backscattering sensor (figure 3.4). This sensor also measures *CHL-a* fluorescence at 676 nm. It has two separate channels, each with its own light emitting diode (*LED*) source. The *LED* enables a beam of light to be created in water and the receiver optics detect the light that is scattered. This beam of light is transmitted into the water with an approximate angle of 20 degrees to the normal and the divergences that occur from the source beam and the field of view of the receiver determine the scattering angles that the measurement is taken from. The HydroScat estimates the *VSF* at 140° which contributes to the calculation of the backscattering coefficient using equation 2.42 (HOBILabs User's Manual, 2008). HydroScat data processing includes a correction to compensate for the effects of light attenuation that occurs in the light path:

$$b_b = \sigma\left(K_{bb}\right).b_{bu} \tag{3.2}$$

where, b_{bu} is the uncorrected backscattering and $\sigma\left(K_{bb}\right)$ is a function of a) the sensor geometry and b) the *IOPs* of the sample volume which can be measured using an *ac-9* (HOBILabs User's Manual, 2008).

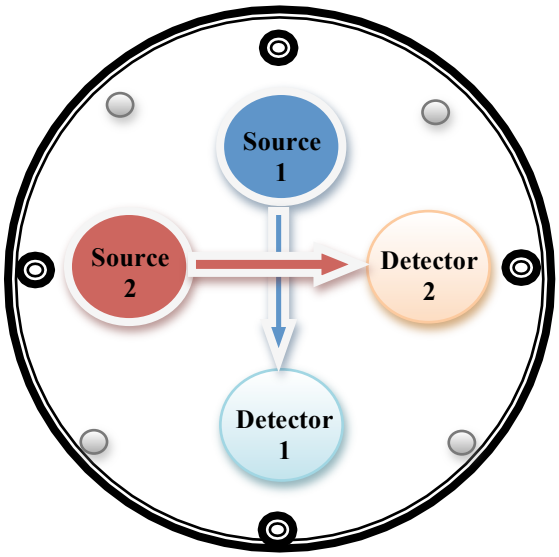

Figure 3.4: HOBILabs HydroScat-2 backscattering sensor (HOBILabs User's Manual, 2008).

3.3 In *situ* measurements

The SeaBird SBE 19 CTD was used to measure the temperature and salinity of each cruise station. The WET Labs ac-9 (or ac-9 plus) was calibrated using Milli-Q ultra pure water before collecting data for the water absorption and beam attenuation coefficients (a_{nw} and c_{nw}) at nine wavebands (412, 440, 488, 510, 532, 555, 650, 676 and 715 nm). The ac-9 WET Labs ac-9 user manual gives details for correcting temperature and salinity variations between the calibration water sample and the *in situ* station sample. This correction was applied using the Sullivan *et al*., (2006) coefficients and *CTD* profiles. Correction for the absorption measurements were required to account for inefficient measurements of scattered light. This correction is referred to as the proportional method, defined by Zaneveld *et al.*, (1994). This correction sets the water absorption at 715nm to zero, assuming negligible effects of suspended and dissolved particle absorption at the near-IR waveband. To obtain the non-water scattering coefficients (b_{nw}) the water absorption data was subtracted from the beam attenuation coefficients.

A HOBI Labs HS-2 backscattering meter was used to collect data for backscattering coefficients (b_b) at two wavebands. These bands were centered on 470 nm and 676 nm. Coefficients of a_{nw} and b_{nw} described above were used in conjunction with the *sigma correction method* to account for absorption and scattering. Particulate backscattering coefficients (b_{bp}) were obtained by subtracting the water contribution, which was taken to be half the total scattering values measured by Smith and Baker (1978). Extrapolation was required to overcome measurements at only two wavebands. Deployment of the *HS-2* alongside a Wet Labs ECO *BB9* instrument (backscattering at nine waveband as opposed to 2) in subsequent cruises confirmed that linear extrapolation between the *HS-2* channels at 470 nm and 676 nm gave values within +/-20% of those measured by the *BB9* within this wavelength range.

A Satlantic *SPMR* profiling radiometer, for the measurement of downwards-planar irradiance (E_d) and upward radiance (L_u), was used to collect *in situ* data at each cruise station. The profiler collected data centered on 412, 443, 490, 510, 554, 665 and 700 nm. *SPMR* casts were carried out at least 20 m from the ship to avoid shadow effects, and two casts were averaged for each station. As weather conditions along the Western UK coast is highly variable, collection of data was not always conducted in conditions conducive to satellite remote sensing. However, this data has been included in the overall data set. Values for water-leaving radiance and above-surface downward irradiance, which are required for calculations of remote sensing reflectance, were derived by extrapolating *SPMR* profiles through the air-sea interface using the expressions quoted in the Satlantic ProSoft manual.

3.4 Concentrations of Optically Significant Constituents

Triplicate measurements were conducted for the calculation of *CHL*. 25mm *GF/F* filters were used for filtering *in situ* water samples before they were frozen and stored until returned to the laboratory. Extraction of phytoplankton pigments was accomplished by soaking the filters for 24 h in neutralised acetone at 4^{o}C. Following this, the samples were centrifuged and the absorbance spectrum of the supernatant was measured, relative to an acetone blank, in 1 cm path length cuvettes. Acidification with dilute hydrochloric acid was performed and then the measurement was repeated. The trichromatic equations of Jeffrey and Humphrey (1975) were used to determine the Chlorophyll-*a* concentrations.

Five liters of *in situ* water sample was fltered through 90mm GF/F filters to obtain the mineral suspended particles. 500mls of distilled water was then used to rinse the filters before freezing them for return to the laboratory, where they were dried to a constant weight in an oven at 100°C. Samples were weighed in order to obtain the concentration of total suspended solids (*TSS*). The samples were then cooked in a furnace at 500 °C for 3 hours to allow reweighing and the determination of the total mineral suspended solids (MSS_T). The use of the furnace allows for the assumption that all organic material is removed.

For determinations of *CDOM*, seawater samples were filtered through 0.2 μm membrane filters, with the filtrate being collected in acid-rinsed glass bottles and stored under refrigeration. Absorption by *CDOM* was measured in a spectrophotometer using 10 cm cuvettes with UV treated ultrapure water as a reference. Care was taken to allow the sample and reference to reach the same temperature before the measurements were carried out.

3.5 Derivation of specific inherent optical properties (*SIOPs*)

Specific inherent optical properties were derived using the methodology developed by Brown (2009).

a) Specific absorption coefficients.

500ml of *in situ* water sample was filtered through a 25mm diameter Whatman *GF/F* filters to collect suspended particles. Samples were frozen and returned to the laboratory. Sample measurements were made using a custom-built spectrophotometer with a highly collimated single beam in which the filters were placed immediately adjacent to a *PTFE* diffuser backed by a photomultiplier detector. The suspended particle filters were moistened with filtered seawater and mounted onto a glass slide with the sample the first surface encountered by the illuminating beam. A clean filter was used as a blank. Acetone was then used to extract the pigments allowing optical density spectra to be measured before after, with the subtraction of these two spectra providing the phytoplankton pigment and non-algal particle measurements. As with the *ac-9* data, optical densities were set to zero at 715 nm. The relationship between filter optical density (OD_f) and the apparent absorption coefficient (a_f) for the material on the filter is given by

$$a_f(\lambda) = \frac{2.303 \times OD_f(\lambda) \times A}{V} \tag{3.3}$$

where A is the effective area of the filter and V the volume of sample filtered. The apparent absorption coefficients of particles collected on glass fibre filters is known to be greater than that of an equivalent concentration of particles in suspension (a_{sus}), the two coefficients being related by a path length amplification factor β

$$a_{sus}(\lambda) = \frac{a_f(\lambda)}{\beta} \tag{3.4}$$

whose numerical value varies with measurement methodology and filter loading (Bricaud and Stramski 1990, Lohrenz 2000). This variability could be reduced with Tassan and Ferrari's (1998) transmittance plus reflectance technique. For the work

reported here, we obtained a value for β by plotting the absorption coefficients derived with no pathlength compensation against the particulate absorption coefficients measured at the same location in situ using an *ac-9*. Spectrophotometer measurements were averaged over the 10 nm bandwidths covered by the ac-9 for this purpose. The resulting graph was clearly linear (Figure 3.5.), with a gradient derived by geometrical mean regression of $\beta = 1.73$ and a coefficient of determination $r^2 = 0.90$. This procedure allowed filter pad optical densities to be converted to absorption coefficients for phytoplankton (a_{ph}) and non-algal particulates (a_{nap}) using equations 3.3 and 3.4.

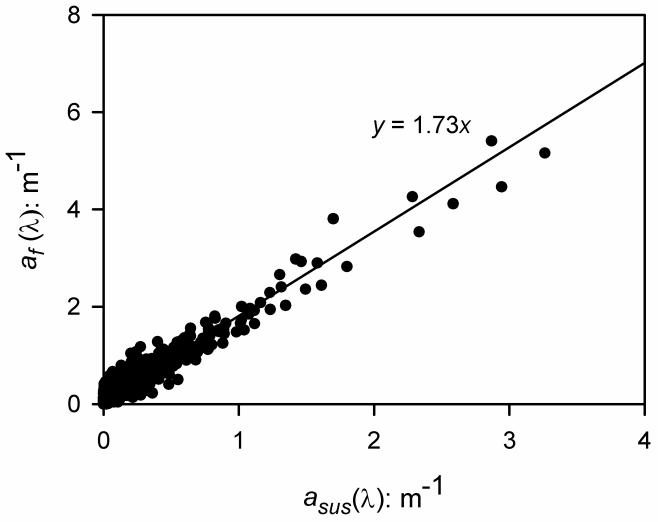

Figure 3.5. Apparent absorption coefficients of particles collected on filter pads, $a_f(\lambda)$, plotted against particulate absorption coefficients measured *in situ* using an *ac-9*, $a_{sus}(\lambda)$. The line, derived by geometric mean regression, has a slope of $\beta = 1.73$ and coefficient of determination r^2=0.9.

Specific absorption coefficients for phytoplankton and mineral particles, $a^*_{CHL}(\lambda)$ and $a^*_{MSSter}(\lambda)$) were calculated by dividing the absorption coefficients obtained from the analysis of samples on filters by the measured *OSM* concentrations. For *CDOM*, the spectral dependence of absorption was described by

$$\frac{a(\lambda)}{a(440)} = e^{-S(\lambda-440)} \tag{3.5}$$

(Bricaud *et al.* 1981) where $a(440)$ is the absorption coefficient at 440 nm and the exponent S serves as the equivalent of an *SIOP*. The calculation of remote sensing reflectance from *in situ* measurements is described in section 2.6 (b) and can be defined as:

$$R_{rs} \approx \kappa \frac{b_{b\,W} + b^*_{b\,MSS_T} MSS_T + b^*_{b\,CHL} CHL}{a_W + a^*_{MSS_T} MSS_T + a^*_{CHL} CHL + a^*_{CDOM} CDOM} \tag{3.6}$$

b) Specific scattering and backscattering coefficients.

Currently, it is not possible to separate the different contributions to the scattering coefficients by the varying types of particles. However, by plotting MSS_T against *CHL* for all stations (Figure 3.6), it is possible to identify groups of points characterised by relatively high *CHL* and low MSS_T (Cluster 1) and by low *CHL* accompanied by high MSS_T (Cluster 2). Stations falling into these groups were selected by setting thresholds of *CHL* >4 mg m^{-3} for Cluster 1 and MSS_T >4 g m^{-3} for Cluster 2.

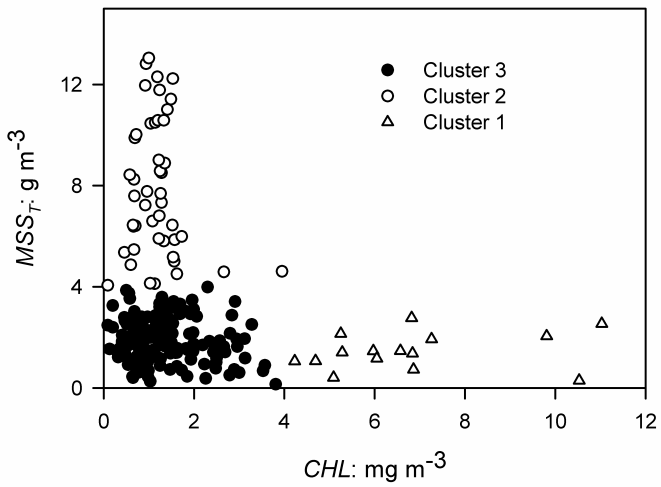

Figure 3.6: Particulate backscattering at 676 nm ($b_{bp}676$) plotted against total suspended mineral concentrations (MSS_T).

Cluster 1 stations were located mainly in deep Scottish sea lochs, which generally have low concentrations of suspended sediment, while those in Cluster 2 were from relatively shallow, coastal areas of the Irish Sea and Bristol Channel with high suspended sediment concentrations. It was assumed therefore, that the scattering properties of Cluster 1 were primarily determined by phytoplankton cells (measured as *CHL*) and those of Cluster 2 by mineral particles of a terrigenous origin (MSS_{ter}). Specific scattering coefficients, $b^*MSS_{ter}(\lambda)$ and $b^*CHL(\lambda)$ and backscattering coefficients, $b_b^*MSS_{ter}(\lambda)$ and $b_b^*CHL(\lambda)$, for these two classes of material were estimated from the ratio of *IOPs* to *OSMs* for the stations in the two groups. The remaining stations (Cluster 3) were not classifiable as being dominated by phytoplankton or suspended sediment. Most of these stations were located in areas of the Irish Sea with depths over 30 m, and optical microscopy indicated that they contained a high proportion of colonial diatoms. We conclude that a significant fraction of the MSS_T measured at these stations consists of biogenic minerals in the form of diatom frustules and that the contribution of this material to scattering and absorption should logically be include in the phytoplankton-related *CHL* component.

c) Derived SIOPs

The set of specific inherent optical properties derived by the methods described above were used as an initial basis for radiative transfer modeling. They are illustrated in Figure 3.7 and 3.8, and listed in Table 3.1 below. Table 3.2 gives inherent optical properties for pure water in the same wavebands, using absorption data from Pope and Fry (1977) and scattering data from Smith and Baker (1978).

a) b)

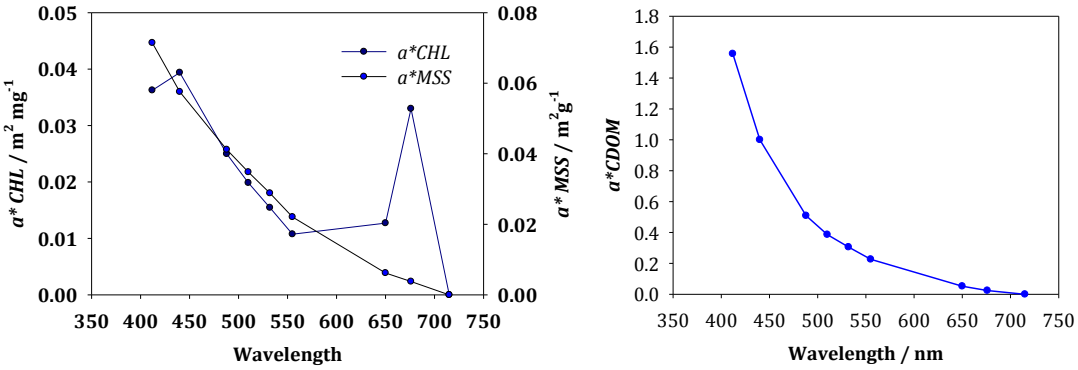

Figure 3.7 a) *Chl a* specific absorption coefficients, $a^*_{CHL}(\lambda)$ and *MSS*-specific absorption coefficients, $a^*_{MSS}(\lambda)$. (b) *CDOM*-specific absorption coefficients, $a^*_{CDOM}(\lambda)$.

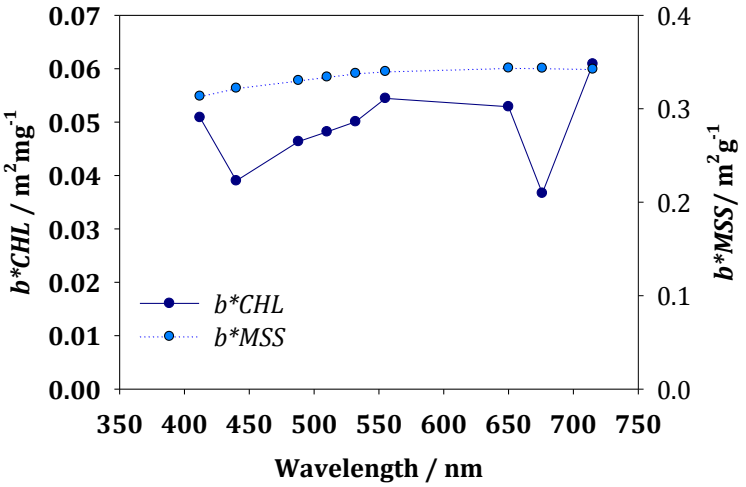

Figure 3.8: Mean specific scattering for *Chl*, $b^*_{CHL}(\lambda)$, and *MSS,* $b^*_{MSS}(\lambda)$. Evidence of anomalous dispersion is present where minima occur in the scattering cross sections associated with the chlorophyll absorption peaks (Gordon *et* al, 2009).

Wavelength (nm)	a^*_{CHL} ($m^2\ mg^{-1}$)	$b_b{}^*_{CHL}$ ($m^2\ mg^{-1}$)	b^*_{CHL} ($m^2\ mg^{-1}$)	a^*_{MSS} ($m^2\ g^{-1}$)	$b_b{}^*_{MSS}$ ($m^2\ g^{-1}$)	b^*_{MSS} ($m^2\ g^{-1}$)	a^*_{CDOM}
412	0.036	0.0012	0.0509	0.071	0.0154	0.3134	1.556
443	0.038	0.0012	0.0395	0.057	0.0145	0.3226	0.969
489	0.025	0.0012	0.0464	0.041	0.0133	0.3305	0.503
510	0.02	0.0011	0.0482	0.035	0.0127	0.334	0.386
555	0.011	0.0011	0.0544	0.022	0.0115	0.334	0.226
665	0.024	0.0011	0.0435	0.005	0.0086	0.3435	0.036
700	0.013	0.0011	0.0516	0.001	0.0077	0.3428	0.009

Table 3.1: Specific inherent optical properties for the three optically significant materials at SeaWiFs wavebands derived from cruises in the Bristol Channel and Irish Sea

Wavelength (nm)	a^*_{water}	$b_b{}^*_{water}$	b^*_{water}
412	0.005	0.0033	0.0067
443	0.007	0.0024	0.0048
489	0.015	0.0015	0.0031
510	0.033	0.0013	0.0026
555	0.059	0.0009	0.0019
665	0.425	0.0004	0.0008
700	0.624	0.0003	0.0007

Table 3.2: Specific inherent optical properties for pure seawater at SeaWiFs wavebands.

3.6 HydroLight

Hydrolight is a numerical software programme that solves the time independent, integro-differential radiative transfer equation to obtain the radiance distribution and derived quantities within and leaving any plane-parallel water body (Mobley and Sundman., 2001). To allowed different water bodies and different environmental conditions to be examined, *IOPs* that were representative of the coastal shelf of the UK were used as input parameters for Hydrolight modelling. The program has a built in graphical user interface (*GUI*) where a user can manually input the desired parameters including; absorbing and scattering properties, sky spectral radiance distribution and boundary conditions. However, the use of the *GUI* heavily restricts the number of runs that can be done as manual input imposes a significant time burden and also increases the chances of human error.

To bypass the Hydrolight *GUI*, Matlab scripts were written during the course of this project to streamline the input and output processes of Hydrolight. This approach had the following advantages:

1. Manual input using the *GUI* generates an I.txt file that has standard information for each run and also specific information relating to the selected input parameters. The Matlab script allowed the user to specify multiple values for cloud cover, solar angle and wind speed and then generated the required number of I.txt files in a few seconds. The Hydrolight program could then be run from these files.
2. The output files that are created from each run are in text format. The Hydrolight programme supplies an Excel macro to process this data but again, this is incredibly time consuming. Consequently, a Matlab script was created that selected the required information automatically and processed it into one output file. This reduced the manual burden of processing and removed human errors that can occur from copying and pasting data between files. A detailed flow chart of the processes used in this work is presented in figure 3.9.

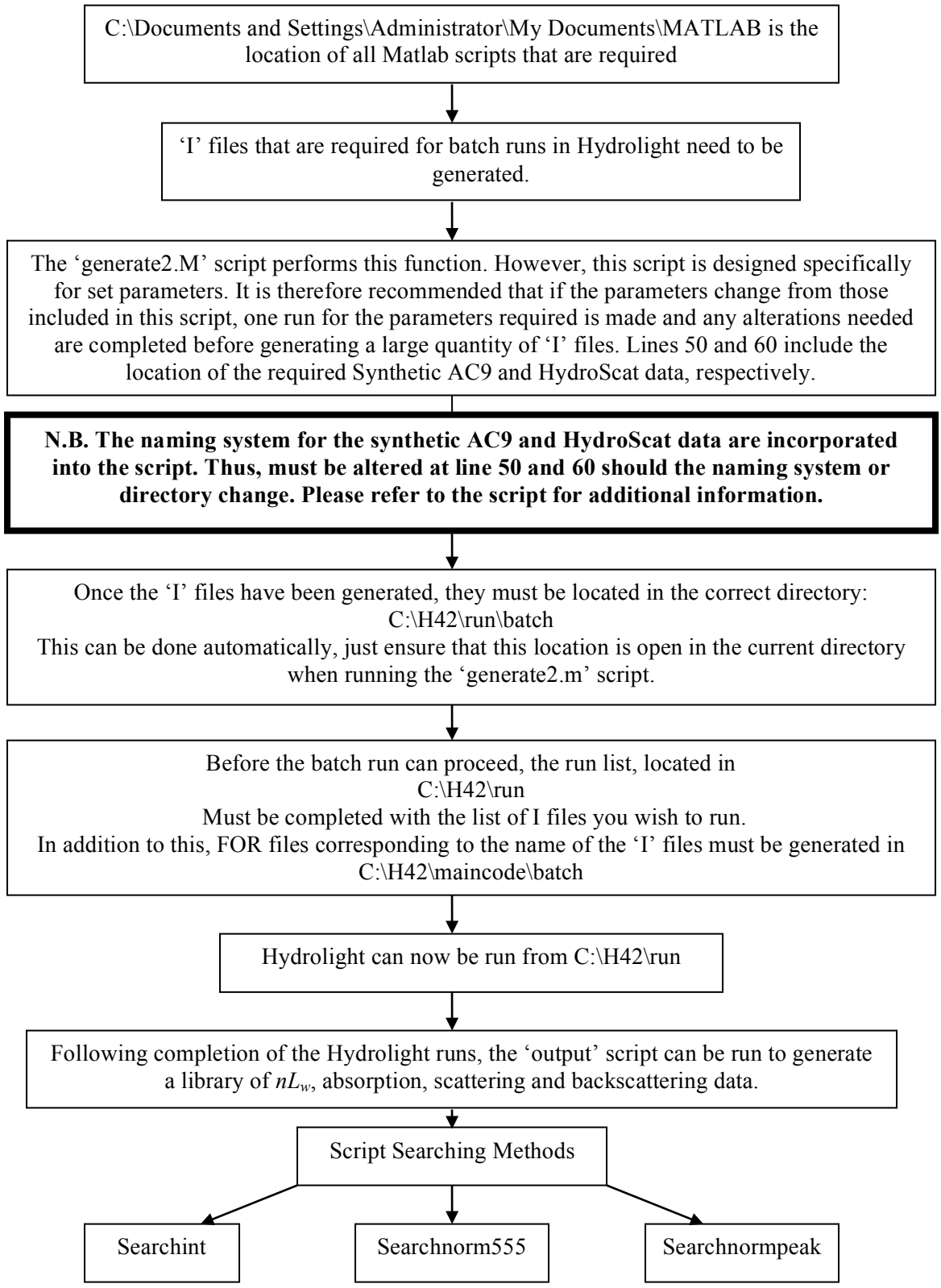

Figure 3.9. Flow diagram illustrating the use of the Matlab scripts used in this thesis.

The use of Matlab scripts allowed a large number of radiative transfer calculations to be performed without the significant time expenditure incurred using the *GUI* to manually set up each individual Hydrolight run. Radiative calculations were performed using the *SIOPs* listed in table 3.1 and the range of constituent concentrations listed in table 3.3. Hydrolight performed linear interpolations between the inherent optical properties supplied if this was required by the specification of the ouput wavebands. A new Fournier-Forand phase function was selected by Hydrolight when the b_b/b ratio varied by a specified amount (0.0005). The constituent combinations used (see Table 3.3) resulted in 1331 radiative calculations being performed for predefined environmental conditions that were based on cloud cover, wind speed and solar angle.

To assess the effect of environmental conditions (solar angle, cloud cover and wind speed) on the estimation of remote sensing signals, a variety of scenarios were investigated. Hydrolight simulations described above were repeated for every combination of environmental factor listed in table 3.4. This resulted in radiance distribution libraries for 75 different environmental conditions.

Constituents	**Range**	**Interval**
CHL	0 – 20 mg/m^3	2 mg/m^3
MSS	0 – 20 g/m^3	2 g/m^3
CDOM	0 – 1 m^{-1}	0.1 m^{-1}

Table 3.3. Range and intervals of the *OSM* concentrations used to perform radiance calculations in Hydrolight.

Environmental Condition	**Range**
Solar angle	25°, 35°, 45°, 55°, 65°
Cloud Cover	0%, 20%, 50%, 80%, 100%
Wind speed	1.1 m/s, 3.1 m/s, 5.1 m/s

Table 3.4. Range of environmental conditions used to perform radiative transfer calculations in Hydrolight.

3.7 Summary of Chapter 3

1. SIOPs were derived from *in situ* measurements collected from cruises that covered areas of the Western UK shelf seas including the Irish Sea and some Scottish Sea lochs. Spectral absorption and beam attenuation coefficients (at nine wavebands) were measured using a WETLabs ac-9 *in situ* absorption and attenuation meter which enables the calculation of the scattering coefficient. Optical backscattering was measured at two wavelengths (470 nm and 676 nm) using a HOBILabs HydroScat-2.

2. Matlab scripts were constructed to overcome the time burden of using the Hydrolight *GUI* and allow the efficient generation of runs for extensive combinations of input parameters. Hydrolight calculations were used to derive remote sensing reflectance spectra for a realistic range of constituent concentrations and environmental conditions.

Chapter 4

Relationships between R_{rs}, *IOPs* and seawater composition

This chapter investigates relationships between the ratio of the backscattering and absorption coefficients ($b_b(\lambda)/\ a(\lambda)$), the normalized water leaving radiance ($nL_w(\lambda)$) and the remote sensing reflectance ($R_{rs}(\lambda)$). Hydrolight was used to create extensive sets (which will be referred to as libraries) of $nL_w(\lambda)$ and $R_{rs}(\lambda)$ spectra that corresponded to specific spectral vaues of $b_b(\lambda)/\ a(\lambda)$ (and by implication, optically significant material (*OSM*) concentrations). The libraries were created using the *IOPs* and procedures explained in chapter 3. They allowed the influence of the *OSMs* on the relationship between $b_b(\lambda)/\ a(\lambda)$ and $R_{rs}(\lambda)$ to be explored for modelled data that were representative of the Western UK Shelf Sea. To overcome the time constraints associated with large numbers of Hydrolight runs, and to address the problem of *LUT* resolution, relationships were derived for $b_b(\lambda)/\ a(\lambda)$: nL_w and $b_b(\lambda)/\ a(\lambda)$: R_{rs}. These relationships allowed an *LUT* of $b_b(\lambda)/\ a(\lambda)$ vectors (consisting of values in seven wavebands), with their corresponding *OSM* concentrations, to be generated quickly in MATLAB for any range of constituents required. A remote sensing reflectance signal could therefore be converted to a $b_b(\lambda)/\ a(\lambda)$ signal using the generated relationship and then matched to a high resolution *LUT* to recover the appropriate *OSM* concentrations.

4.1 The effects of *OSM* concentrations on radiance signals

The spectral library generated for the range of constituents modelled in Hydrolight (table 3.3) is displayed in figure 4.1 for both nL_w (λ) and R_{rs} (λ) signals. These graphs show a large spread in the radiance values for the range of *OSM* concentrations used (*CHL* 0 mg m^{-3} to 20 mg m^{-3}, *MSS* 0 g m^{-3} to 20 g m^{-3} and *CDOM* 0 m^{-1} to 1 m^{-1}). To explore the individual effects of these *OSM* concentrations, i.e. the way in which they drive radiance signals a smaller selection of the R_{rs}(λ) spectra is shown in figure 4.2a. This graph shows R_{rs} (λ) *s*pectra for *CHL* set to 2 mg m^{-3}, with *CDOM* ranging from 0 m^{-1} to 1 m^{-1} and for fig.4.2b, *MSS* ranging from 0 g m^{-3} to 20 g m^{-3}. The plots in Fig. 4.2a do not include *MSS,* and so the variation between the spectra is caused by *CDOM*. Increasing the concentration of *CDOM* from 0 m^{-1} to 1 m^{-1} reduces the radiance signal in all wavebands, as indicated by the arrow. In Figure 4.2b, where the variation is due to *MSS*, individual spectra converge at the red end of the spectrum into distinct groups, highlighted by red circles. Each of these groups represents a different concentration of *MSS*, and the arrow indicates the increase in the R_{rs} (λ) produced by increasing the concentration of this constituent from 0 g m^{-3} to 20 g m^{-3}. The contrasting effects of *MSS* and *CDOM* on the radiance signals may be explained by the fact that changes in *MSS* affect absorption, scattering and backscattering whereas changes in CDOM affect only absorption (Kirk, 1994).

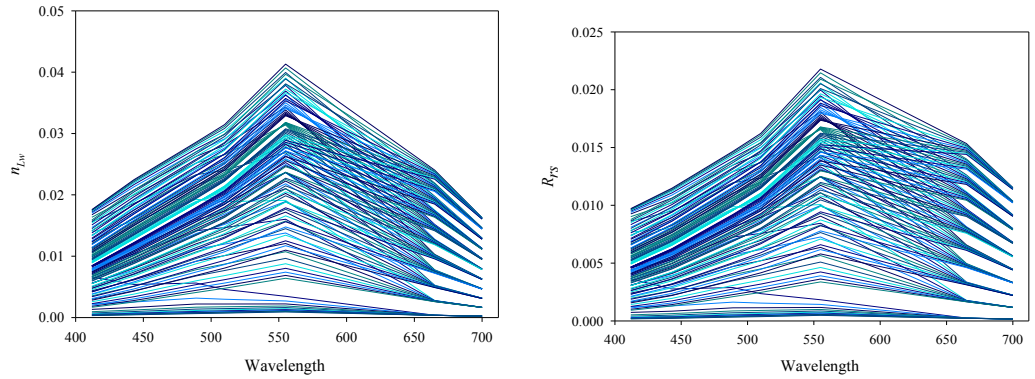

Figure 4.1: The distribution in the remote sensing signals of R_{rs} and nL_w for the full range of constituent concentrations: *CHL* 0 mg m^{-3} to 20 mg m^{-3}, *MSS* 0 g m^{-3} to 20 g m^{-3} and *CDOM* ranging from 0 m^{-1} to 1 m^{-1}.

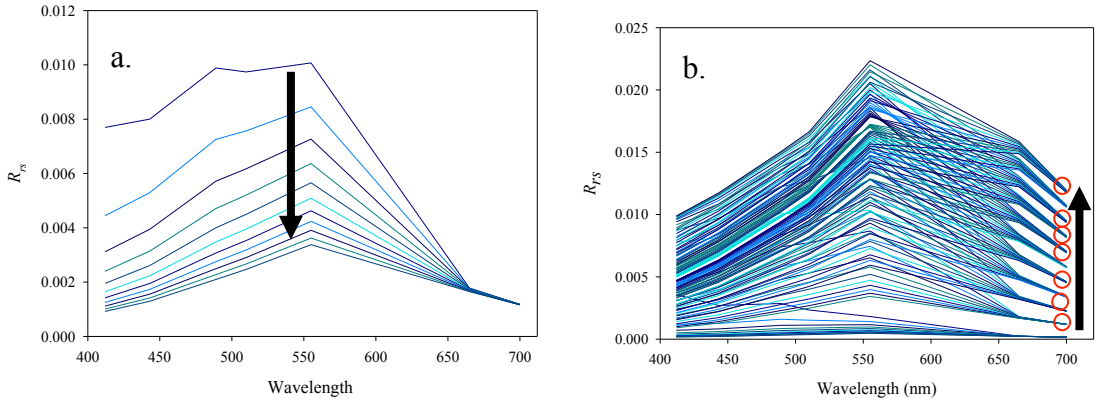

Figure 4.2: R_{rs} spectra representing varying *OSM* concentrations: a) *CHL* fixed at 2 mg m^{-3} with *CDOM* increasing from 0 m^{-1} to 1 m^{-1} b) *CHL* fixed at 2 mg m^{-3} with *MSS* ranging from 0 g m^{-3} to 20 g m^{-3}. The arrows indicate the effects of increasing the concentrations of the individual constituents on the overall spectral distribution.

a) Relationship between $b_b(\lambda)/a(\lambda)$ and R_{rs}

In order to avoid extensive radiative transfer calculations using Hydrolight, the possibility of establishing relationships between $b_b(\lambda)/a(\lambda)$ and R_{rs} was investigated. For simplicity, linear approximations to these relationships were derived initially. It was later found that polynomial relationships yielded better inversion results for the purposes of spectral matching, and this is discussed further in Chapter 5. The process involved the following stages:

1. Hydrolight runs were performed for the range of concentrations and environmental conditions listed in table 3.3 and 3.4.

2. Best-fit linear relationships were established at 7 (SeaWiFs) wavelengths between $b_b(\lambda)/a(\lambda)$ and $R_{rs}(\lambda)$.

Figure 4.3 illustrates the relationship at each wavelength and provides evidence of slight wavelength dependence. Table 4.1 lists the gradients and R^2 values for these relationships. This confirms the wavelength dependence and shows that the R^2 values are over 0.99 for each wavelength, indicating a good linear fit. Hydrolight inputs are predominately controlled by the user, who supplies a file in AC-9 format containing the absorption and attenuation coefficients and a file in HydroScat format containing the backscattering coefficients. Hydrolight then selects a wavelength-dependent phase function from the available Fournier-Forand functions (Fournier and Forand, 1994) with a $b_b/b(\lambda)$ ratio obtained from the user supplied HydroScat and AC-9 data files. In order to determine if wavelength dependence in the phase function selected could account for the slight variation evident in the $R_{rs}(\lambda)$ against b_b/a (λ) spectra, use was made of an in-built option of specifying a fixed $b_b/b(\lambda)$ ratio, which in turn results in a constant phase function. The effect of fixing the phase function on the relationship between $R_{rs}(\lambda)$ and $b_b/a(\lambda)$ is displayed in figure 4.4 (values are listed in table 4.2). These result show a near perfect linear relationship which is supported by the R^2 values. The gradients all fall between 20.3 and 21 giving a gradient variation of only 0.9 in comparison to the 2.1

variation when the phase function is not fixed (table 4.1). The b_b/b ratio used to fix the phase function was calculated by averaging the b_b and b values obtained from the Hydrolight outputs that were originally used to build the relationships between R_{rs} and b_b/a. This b_b/b ratio was calculated as 0.0343.

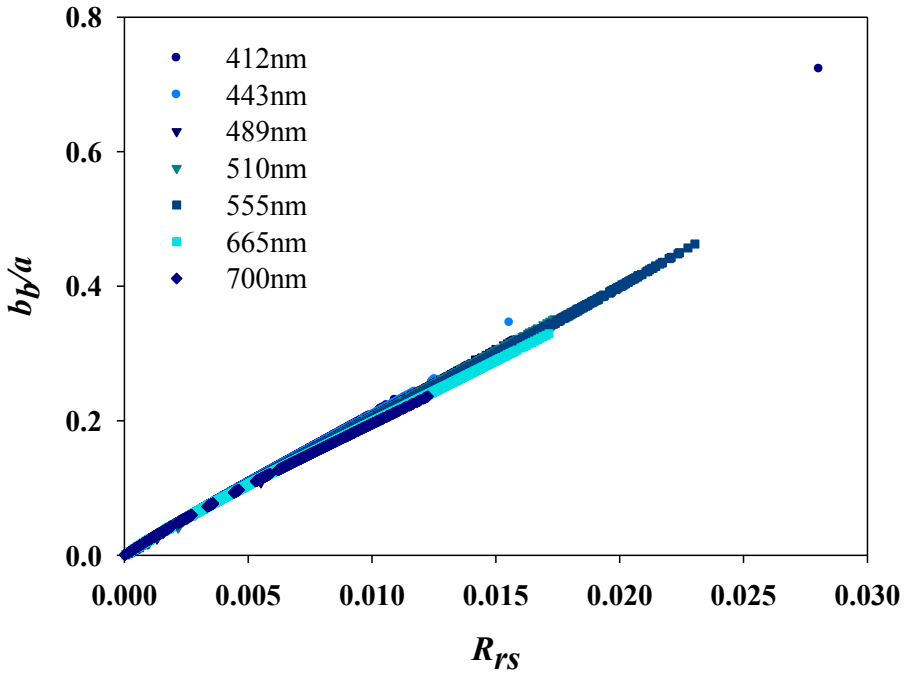

Figure 4.3: Relationship between b_b/a (λ) and R_{rs} (λ) when Hydrolight is allowed to select a new phase function at each waveband.

	412 nm	443 nm	489 nm	510 nm	555 nm	665 nm	700 nm
Gradient	21.44	20.81	20.27	20.03	19.56	19.30	19.31
R^2	0.9952	0.999	0.9995	0.9995	0.9997	0.9991	0.9988

Table 4.1. Gradient and R^2 values for the relationships between b_b/a (λ) and R_{rs} (λ) when Hydrolight selects for a new phase function at each waveband.

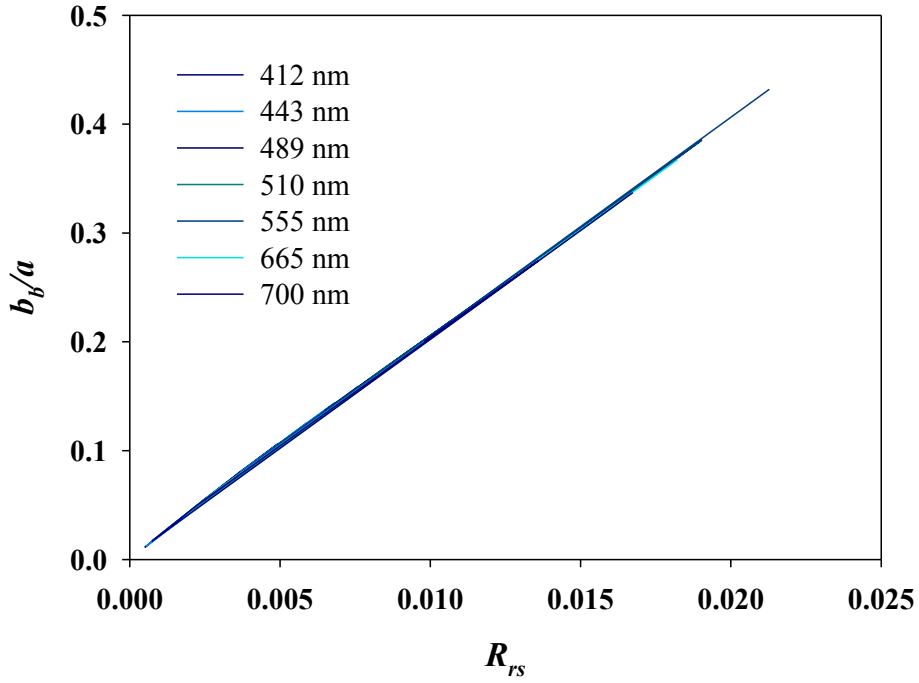

Figure 4.4: Relationship between b_b/a (λ) and R_{rs} (λ) when a fixed phase function is employed.

	412 nm	443 nm	489 nm	510 nm	555 nm	665 nm	700 nm
Gradient	20.71	20.52	20.34	20.38	21.02	20.63	20.51
R^2	0.9998	0.9999	1	1	.9995	0.9998	0.9999

Table 4.2. Gradient and R^2 values for the relationships between b_b/a (λ) and R_{rs} (λ) when the function is fixed.

b) Relationship between $b_b(\lambda)/\ a(\lambda)$ and nL_w

The normalized water leaving radiance (nL_w) is derived using:

$$nLw(\lambda) = \frac{L_W(\lambda)}{E_d(\lambda)} F_0(\lambda) \tag{4.1}$$

where F_0, the extraterrestrial solar irradiance, is corrected for the earth–sun orbital distance and eccentricity. The extraterrestrial solar irradiance values were taken from the Gregg and Carder (1990) sky irradiance model. The F_o term accounts for the attenuation that occurs within the atmosphere and the radiation from the sky. This attenuation is due to absorption and scattering by marine aerosols, Rayleigh scattering by atmospheric gases, and absorption by ozone, oxygen and water vapour. In cloud-free conditions, the solar energy that reaches the sea surface is predominantly derived from the direct solar beam that remains after these processes occur (Kirk, 1983).

Computed relationships between (nL_w) and $b_b(\lambda)/\ a(\lambda)$ are shown in Figure 4.5. A large part of the spectral variation that is evident in this relationship is due to the extraterrestrial solar irradiance value F_0, whose wavelength dependence is shown in figure 4.6.

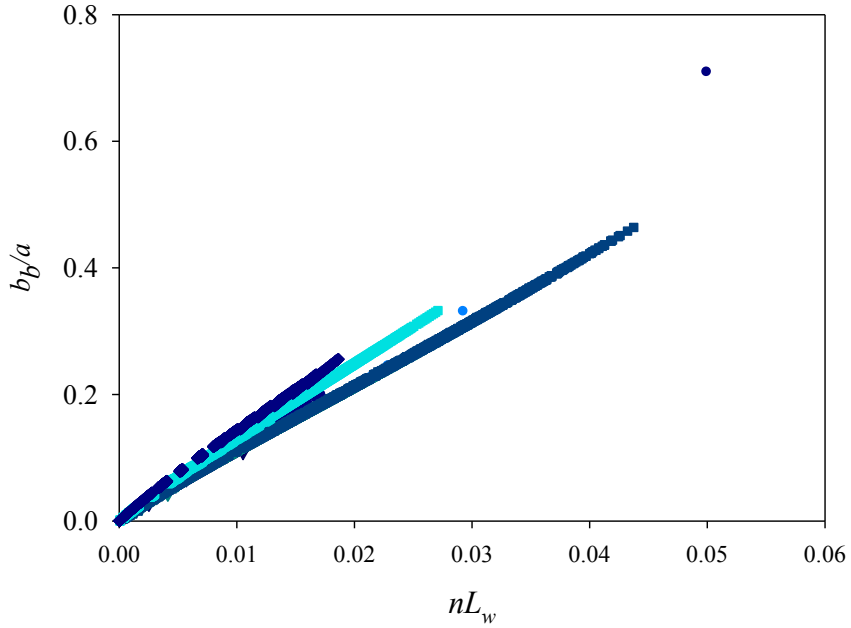

Figure 4.5: $b_b/a(\lambda)$ against nL_w (λ)for the 7 SeaWIFs wavelengths. A significantly different gradient was observed for three of the wavelengths (412nm, 665nm and 700nm).

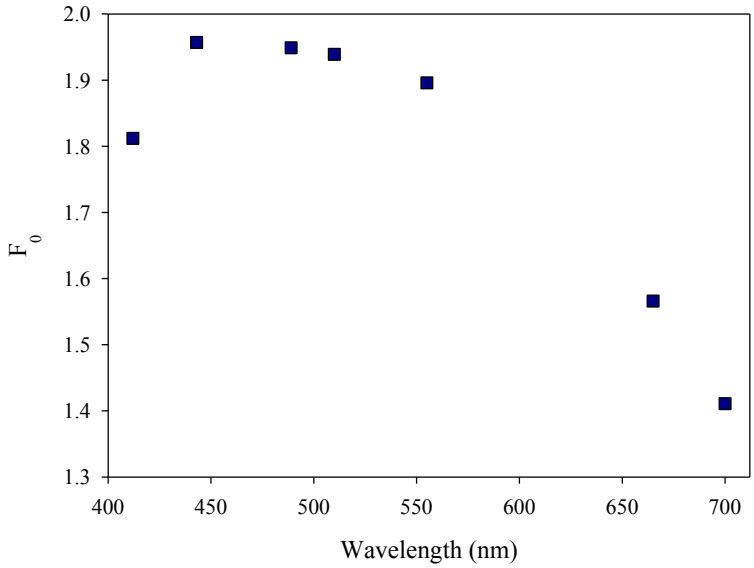

Figure 4.6: The extraterrestrial solar irradiance value F_0 which accounts for the attenuation that occurs within the atmosphere and the radiation from the sky. These values are used to normalise R_{rs} (λ) signals.

c) Comparison of the $b_b(\lambda)/\ a(\lambda)$: R_{rs} and $b_b(\lambda)/\ a(\lambda)$: nL_w relationship when the phase function is fixed

The variation between wavelengths for the $b_b(\lambda)/\ a(\lambda)$: nL_w Hydrolight results is shown in figure 4.5. Using the wavelength with the highest gradient value, which was found to be 555nm, the percentage difference between that and the gradient values of 412, 665 and 700 nm was 13%, 16% and 25%, respectively, where the other wavelengths show a less than 3% deviation from 555nm. Table 4.3 lists these percentage differences, as well as the observable differences when the normalisation step is removed and the $b_b(\lambda)/\ a(\lambda)$: R_{rs} (λ) relationship is used.

	412 nm	**443 nm**	**489 nm**	**510 nm**	**555 nm**	**665 nm**	**700 nm**
b_b/a:nL_w	13%	<3%	<3%	<3%	Base	16%	25%
b_b/a:R_{rs}	9%	6%	3%	2%	Base	1%	1%

Table 4.3: The percentage differences between the gradients for the normalised and non-normalised relationships using 555 nm as a reference value.

Removing the normalisation step has resulted in a gradient difference of 9%. in the blue waveband (412 nm), with a gradual decrease towards the red wavelengths (700nm). While the removal of the normalisation step significantly reduced the variation between the gradients, there still remained a significant difference between the wavelengths. Although fixing the phase function with the $b_b(\lambda)/\ a(\lambda)$: R_{rs} resulted in a tighter relationship between wavelengths (Table 4.4), the effect of fixing the phase function on

the $b_b(\lambda)/\ a(\lambda)$: nL_w relationship had no impact on the gradient distribution (Table 4.5).

412 nm	443 nm	489 nm	510 nm	555 nm	665 nm	700 nm
1%	2%	3%	3%	Base	2%	2%

Table 4.4: The percentage difference in gradient (from 555 nm) when the normalization step is removed and the phase function is fixed.

412 nm	443 nm	489 nm	510 nm	555 nm	665 nm	700 nm
10%	0.9%	2%	2%	Base	17%	25%

Table 4.5: The percentage differences in gradient (from 555 nm) for the $b_b(\lambda)/\ a(\lambda)$: nL_w relationship, for a fixed phase function.

d) The effect on the $b_b(\lambda)/\ a(\lambda)$: R_{rs} relationship when the phase function is altered

To assess how altering the phase function affects the relationships of $b_b(\lambda)/\ a(\lambda)$: R_{rs} with respect to the gradient deviations between wavelengths, the phase function was altered by plus and minus five and ten percent (of the original value) and the Hydrolight runs were repeated. The percentage differences in the gradients from the 555 nm value are given in table 4.6. It can be seen that altering the phase function does have an effect on the values of the gradients.

Variation	412 nm	443 nm	489 nm	510 nm	555 nm	665 nm	700 nm
+5%	3%	4%	4%	4%	Base	2%	3%
-5%	0.4%	1%	3%	3%	Base	2%	2%
+10%	4%	5%	5%	4%	Base	3%	3%
-10%	0.8%	0.4%	2%	2%	Base	1%	1%
0%	1%	2%	3%	3%	Base	2%	2%

Table 4.6: The percentage difference in gradients when the normalization step is removed and the phase function is altered by the percentage indicated in the left hand column.

The normalisation step has therefore been shown to have a significant influence on the relationship of $b_b(\lambda)/\ a(\lambda)$: R_{rs}, which may be partly explained by the wavelength dependence of the extraterrestrial solar irradiance. However, following the removal of the normalisation step, gradient variation across the wavelengths was significantly reduced but was still present. It has been shown that this may be attributed to the changes in phase function. A fixed phase function was shown to result in a very small percentage difference when the normalisation step was removed, and varying the phase function introduced increased percentage differences in the positive direction (table 4.6). Gordon (1983) demonstrated that the relationship between R_{rs} and b_b/a depends on the angular distribution of the underwater light field, which is partly a function of the phase function but also depends on the input light field. These relationships are explored further in Chapter 5.

4.2 Converting an R_{rs} signal to a b_b / a vector

At this stage in the analysis, linear relationships have been generated which could be used to convert an $R_{rs}(\lambda)$ observation to a corresponding $b_b(\lambda)/\ a(\lambda)$ ratio. Table 4.7 shows representative linear relationships for a solar angle of 45°, wind speed of 3.1 ms^{-1} and zero cloud cover. These relationships allow an observed R_{rs} spectrum to be converted waveband by waveband to b_b/a (λ) values and matched to entries in an *LUT* of $b_b(\lambda)/\ a(\lambda)$ vectors generated in Matlab from triplet concentrations of *OSMs*. (Later, for the purposes of spectral matching, it is shown that polynomial relationships yielded rather better inversion results: see Chapter 5.)

	412 nm	**443 nm**	**489 nm**	**510 nm**	**555 nm**	**665 nm**	**700 nm**
m	21.4239	20.69417	20.128	19.92828	19.57386	19.01585	19.00808
c	0.000851	0.003366	0.005123	0.005687	0.006055	0.007611	0.006966

Table 4.7: The values required to convert an R_{rs} (λ) signal into a b_b/a (λ) vector based on the linear relationship $y = mx + c$.

4.3 Environmental Variability

In view of the potential spatial and temporal variability in meteorological conditions during the acquisition of remote sensing data, the effect of environmental variability on the relationship of $b_b(\lambda)/\, a(\lambda)$ vs. R_{rs} (λ) was investigated. 75 Hydrolight libraries were created using the *SIOPs* and procedures described in chapter 2. The different combinations of environmental conditions are listed in table 3.3. Figure 4.7 illustrates that the resulting variability in the $R_{rs}(\lambda)$ signals is relatively low, with the maximum difference of 5% occurring at 550 nm.

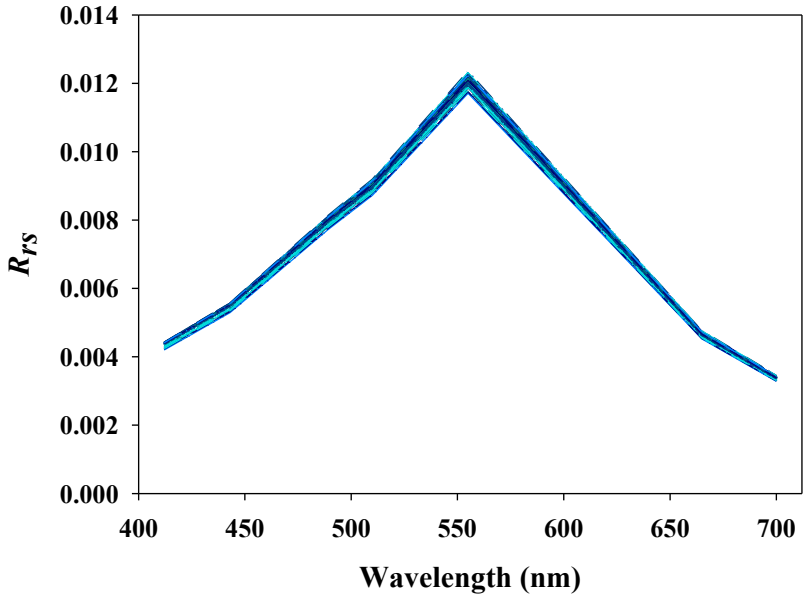

Figure 4.7: This graph represents the distribution across the 75 combinations of environmental conditions derived from Table 3.3 for the $R_{rs}(\lambda)$ signal. The remote sensing signal for each environmental condition was calculated for a water body with the following constituent concentrations: 4 mg/m^3 for *CHL*, for 6 g/m^3 *MSS* and 0.3 m^{-1} for *CDOM*.

Figure 4.8 shows the variability in the gradient m for the 75 combinations of environmental conditions. The plots highlighted in red represent environmental conditions (such as limited cloud cover and a solar angle between 35 and 55 degrees) that would be conducive to satellite monitoring of an area. The spread of the gradients appears small but becomes more pronounced towards the red end of the spectrum. The individual effects of the solar angle, cloud cover and wind speed are shown in Figures 4.9 to 4.13. These graphs suggest that the environmental factors that have most effect on the $b_b(\lambda)/\, a(\lambda)$ vs $R_{rs}(\lambda)$ relationships are the solar angle (figure 4.9) and cloud cover (figure 4.10) with obvious exceptions when the cloud cover is 100% (figure 4.10).

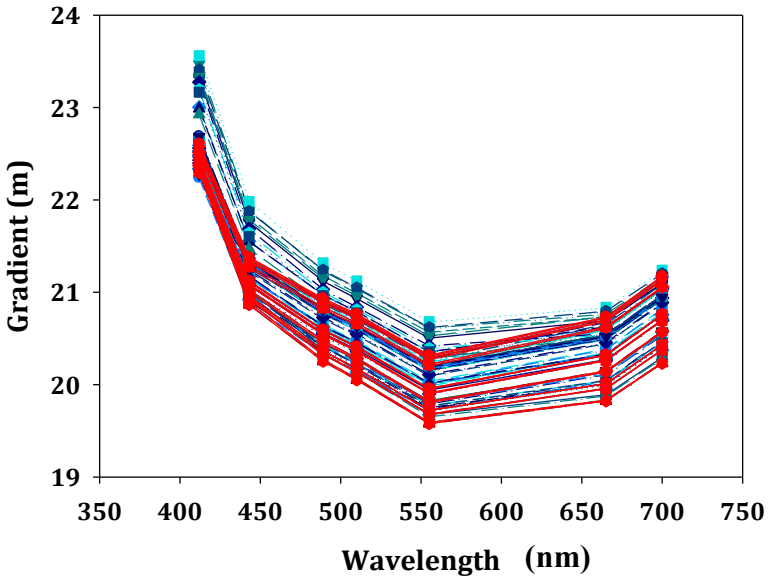

Figure 4.8: Variations in m for all 7 SeaWiFS wavelengths for the 75 environmental combinations that were investigated. Those highlighted in red represent conditions that are conducive to satellite observations.

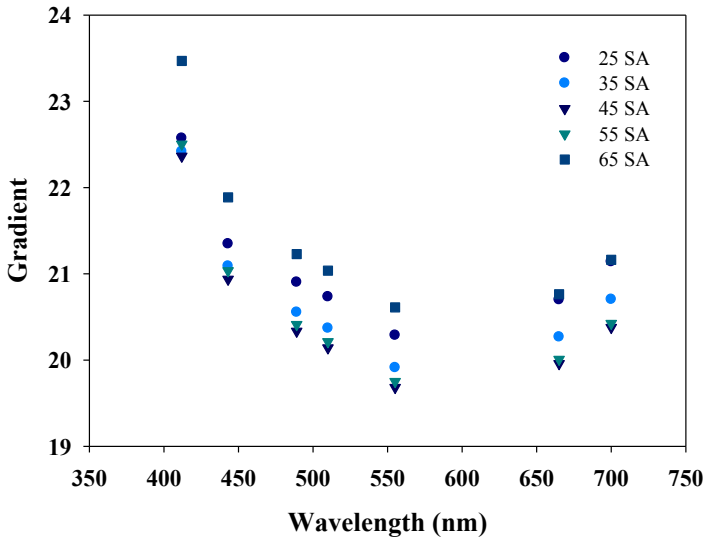

Figure 4.9: This graph depicts the changes in gradient for the relationships between R_{rs} (λ) and b_b/a (λ) (at each wavelength) when only the solar angle is altered. Showing that, overall, the solar angle has the greatest effect on the relationship.

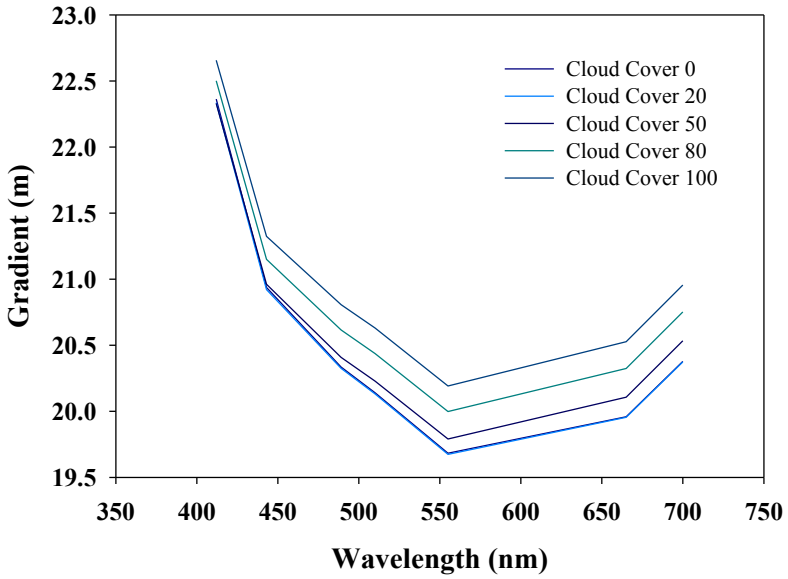

Figure 4.10: This graph represents the effects of altering only the cloud cover as an environmental condition. The solar angle and wind speed have been held constant and 45° and 3.5ms^{-1} respectively.

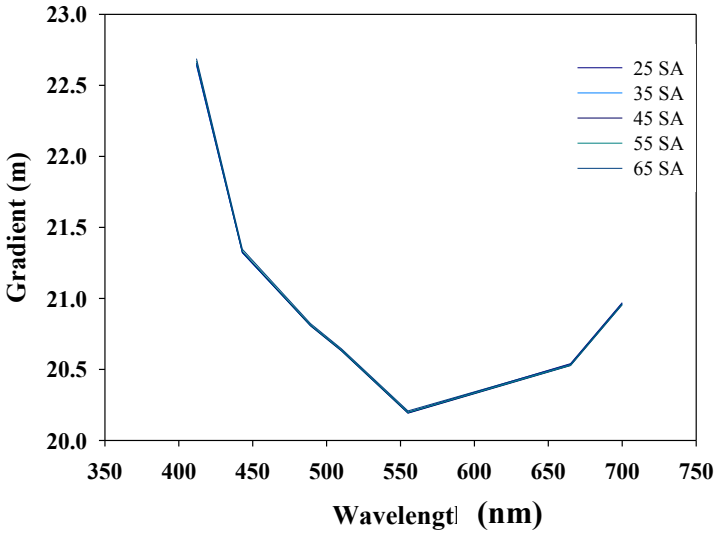

Figure 4.11: Modeled data shows the effect of varying solar angle when the cloud cover is 100%. The other cloud cover parameters of; 0, 20%, 50% and 80% present the same distribution as seen in figure 4.10.

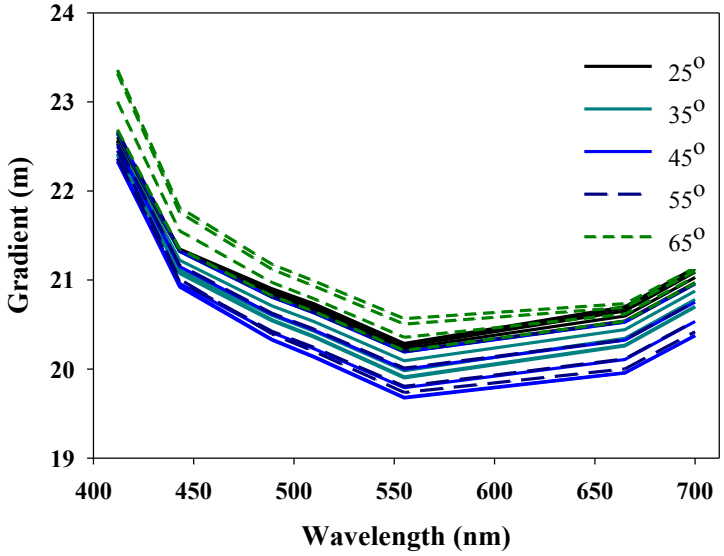

Figure 4.12: The combined effect of altering cloud cover and wind speed on the relationship between $R_{rs}(\lambda)$ and b_b/a (λ). The spread seen within the same colour bands is due to altering cloud cover. Wind speed seems to have little effect on the distribution.

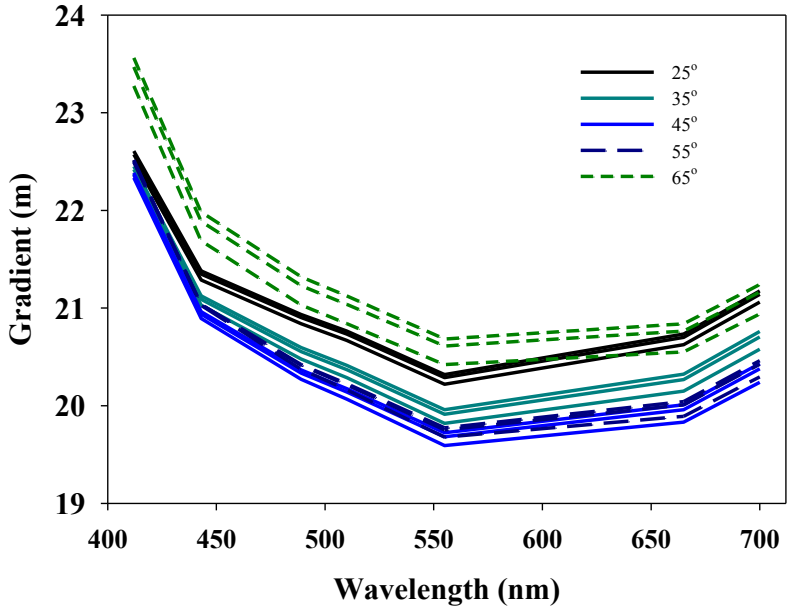

Figure 4.13: This figure displays the effects of altering wind speed at each solar angle. It is evident that wind speed has very little effect within each solar angle but that once again, altering the solar angle clearly alters the gradient and therefore, the relationship between $R_{rs}(\lambda)$ and b_b/a (λ).

For remote sensing inversion, it was necessary to evaluate the importance of converting an R_{rs} signal to a b_b/a value waveband by waveband as opposed to applying a single inversion relationship for all wavebands. Figure 4.14, which displays the linear relationships of $b_b(\lambda)/\, a(\lambda)$ vs $R_{rs}(\lambda)$ for the different wavebands (including varying environmental conditions), suggests that it is necessary to use waveband-specific relationships. Also, a selection process could usefully be incorporated into the inversion process, whereby the user is able to select relationships that best suit the environmental conditions under which data were collected. This process shall be discussed in greater detail in chapter 5.

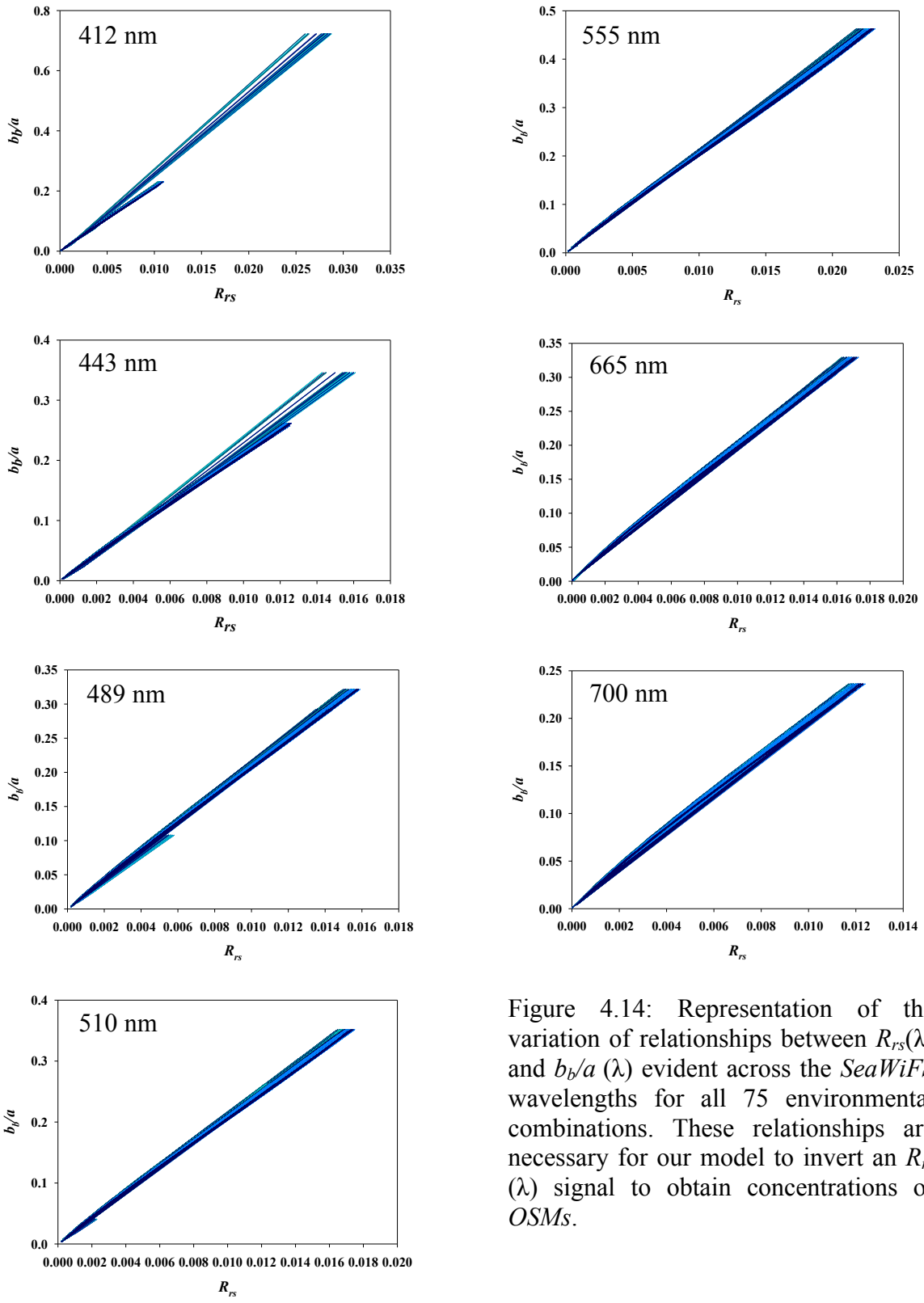

Figure 4.14: Representation of the variation of relationships between $R_{rs}(\lambda)$ and b_b/a (λ) evident across the *SeaWiFS* wavelengths for all 75 environmental combinations. These relationships are necessary for our model to invert an R_{rs} (λ) signal to obtain concentrations of *OSMs*.

4.4 Summary of Chapter 4

- A wavelength dependency was identified when normalized water leaving (nL_w) spectra obtained by radiative transfer calculations were plotted against the $b_b(\lambda)$ / $a(\lambda)$ values used as inputs for these calculations.

- A much tighter relationship between $b_b(\lambda)$/ $a(\lambda)$ and R_{rs} was obtained by the removal of the normalisation step and fixing the phase function.

- The effects of environmental variability on the relationship between $b_b(\lambda)$/ $a(\lambda)$ and R_{rs} was investigated for 75 combinations of environmental conditions (solar angle, cloud cover and wind speed). The maximum calculated variability in R_{rs} signals for a given set of b_b/a values was 5% at 550 nm.

- The wavelength dependence that has been demonstrated in the gradients of the linear relationships between $b_b(\lambda)$/ $a(\lambda)$ and R_{rs} means R_{rs} signals will be converted to a b_b/a vector wavelength by wavelength for the purposes of spectral matching.

- A selection step will be incorporated in the inversion process developed in Chapter 5, whereby the user is able to select environmental conditions that best suit the conditions of data collection.

Chapter 5

Look up tables (*LUTs*) and the various available approaches to spectral matching

In this chapter, the use of a *LUT,* coupled with a spectral matching inversion algorithm for the retrieval of *OSMs* is tested using modeled spectra as inputs. Performing such controlled matches is an important assessment of the robustness of the inversion technique before it is applied to *in situ* remote sensing reflectance data. This chapter will look at the results that are obtained when an R_{rs} signal from a modeled ocean, generated using HydroLight**,** is converted to a $b_b(\lambda)/\, a(\lambda)$ vector (i.e. a set of waveband-specific values) and then matched to a *LUT* of $b_b(\lambda)/\, a(\lambda)$vectors generated from known constituent concentrations. A detailed description of the spectral matching procedure is given, followed by the results that led to an environmental selection step being included. This step allows the user to select the inversion relationship between $b_b(\lambda)/\, a(\lambda)$ that best suits the environmental conditions at the time when the data was collected. The effects of varying *LUT* resolution, as well as the number of spectra to be matched, will be tested with respect to the search times of the spectral-matching look-up table procedure. The various spectral matching algorithms that are available are also discussed.

5.1 Look-up table (*LUT*) principles

The inversion of remotely sensed data for the purposes of ocean color interpretation by spectral matching typically involves three stages:

i. Construction of a forward model for the generation of a spectral library that will be used for matching purposes
ii. Selection of an objective function that describes the disparity between the input spectrum and an entry in the spectral library
iii. Development of a search algorithm that optimizes the match by minimizing the objective function.

Look-up tables have frequently been adopted in data inversion problems due to the way in which they allow large volumes of data to be effectively represented. Liu and Miller (2008) and Mobley *et al.* (2005) were among the first to use a *LUT* for a spectral matching approach in ocean color remote sensing. The approach presented here to resolve the inversion of R_{rs} signals is similar to that adopted by Mobely *et al.* (2005). The obvious way to tackle the problem of R_{rs} inversion was to create a look-up table (*LUT*) of R_{rs} spectra using radiative transfer calculations that encompassed the range of *OSM* concentrations likely to be found in shelf seas. This *LUT* could then be interrogated to identify matches to the initial 'observed' spectrum or spectra. However, the quality of the matches achieved depends on the spacing of the *LUT* entries. The construction of a table with sufficient resolution to be useful in practice would require a very large number of entries. If these entries were obtained from radiative transfer calculations performed in Hydrolight, a great deal of computing time would be required. A possible solution to this problem can be found in the relationship between b_b/a and R_{rs} which was explained in section 2.4 and is displayed in equation 5.1,

$$R_{rs}(\lambda) = \frac{(1-r_F) f_{L,\beta}}{n^2 Q} \times \frac{b_b(\lambda)}{a(\lambda)} : G \times \frac{b_b(\lambda)}{a(\lambda)} \tag{5.1}$$

where, the variable, $\frac{f}{Q}$ is dependent on the optical properties of the water (*f*), the angular distribution of the upwelling light field and the volume scattering function (Chami *et al.*, 2006; Chang and Whitmire, 2009). Consequently, using this relationship, the spectral character of the light leaving the ocean is strongly dependent on the ratio of $b_b(\lambda)/a(\lambda)$ (Gordon and Morel, 1983; Morel and Prieur, 1977). If *G*, which can be considered as a constant only as a crude approximation under restricted circumstances, is known as a function of wavelength, then observed R_{rs} values can be uniquely mapped on to b_b/a values. It is then only necessary to generate an *LUT* of b_b/a vectors in wavebands matching those of the R_{rs} observations. This is easily performed using the products of the *OSM* concentrations and the relevant *SIOPs* (table 3.2 and 3.3).

The *LUT* for this work was therefore calculated by using expressions of the form shown in equations 3.2 and 3.3 to generate total b_b and a values from the *SIOPs* listed in table 3.1. The range of *OSM* concentrations covered was as follows: 0-10 mg m^{-3} for *CHL*, 0-10 g m^{-3} for *MSS* and 0-1 m^{-1} for *CDOM*. The numerical increments between calculations were 0.1 for *CHL* and *MSS* and 0.01 for *CDOM*. The result was a high resolution library of 1,030,301 b_b/a vectors covering the 7 SeaWiFs wavebands. The *LUT* was created in MatLab.

5.2 The spectral matching procedure used in this thesis

The *LUT* and spectral matching inversion procedure that was implemented in this work is outlined in figure 5.1 and described below. This procedure was used for the retrieval of *OSM* concentrations, the investigation of environmental variability, error analysis and the examination of the effects that spatial and *SIOP* variability has on *OSM* concentration retrievals.

First, an R_{rs} signal or signals is obtained for an area of interest, and these signals are entered as the 'unknown' spectra that are to be matched to the *LUT*. The Matlab program that performs the spectral matching is then launched and the user is provided with several options. The number of spectra to be matched must be specified and then the environmental conditions that best match the conditions under which the signal or signals originate must be selected. There is a choice of five solar angles and cloud cover parameters and three wind speeds (table 3.3). The spectral matching routine employs this environmental data to select the best polynomial $b_b(\lambda)/\ a(\lambda)$: R_{rs} relationship for the signal inversion. Section 5.3 details the variation in these relationships for the different environmental conditions. The R_{rs} data is then converted to $b_b(\lambda)/\ a(\lambda)$ spectra, wavelength by wavelength, using the 3rd order polynomial relationships described in section 5.3.

The spectra are then matched to the *LUT* of $b_b(\lambda)/\ a(\lambda)$ vectors using a matching procedure that is based on the calculation of the root mean square error (*RMSE*) averaged across all the wavebands. The best match is taken to be the one with the lowest *RMSE*. Finally an output file is created with the best *OSM* constituent retrievals for the given R_{rs} signal or signals.

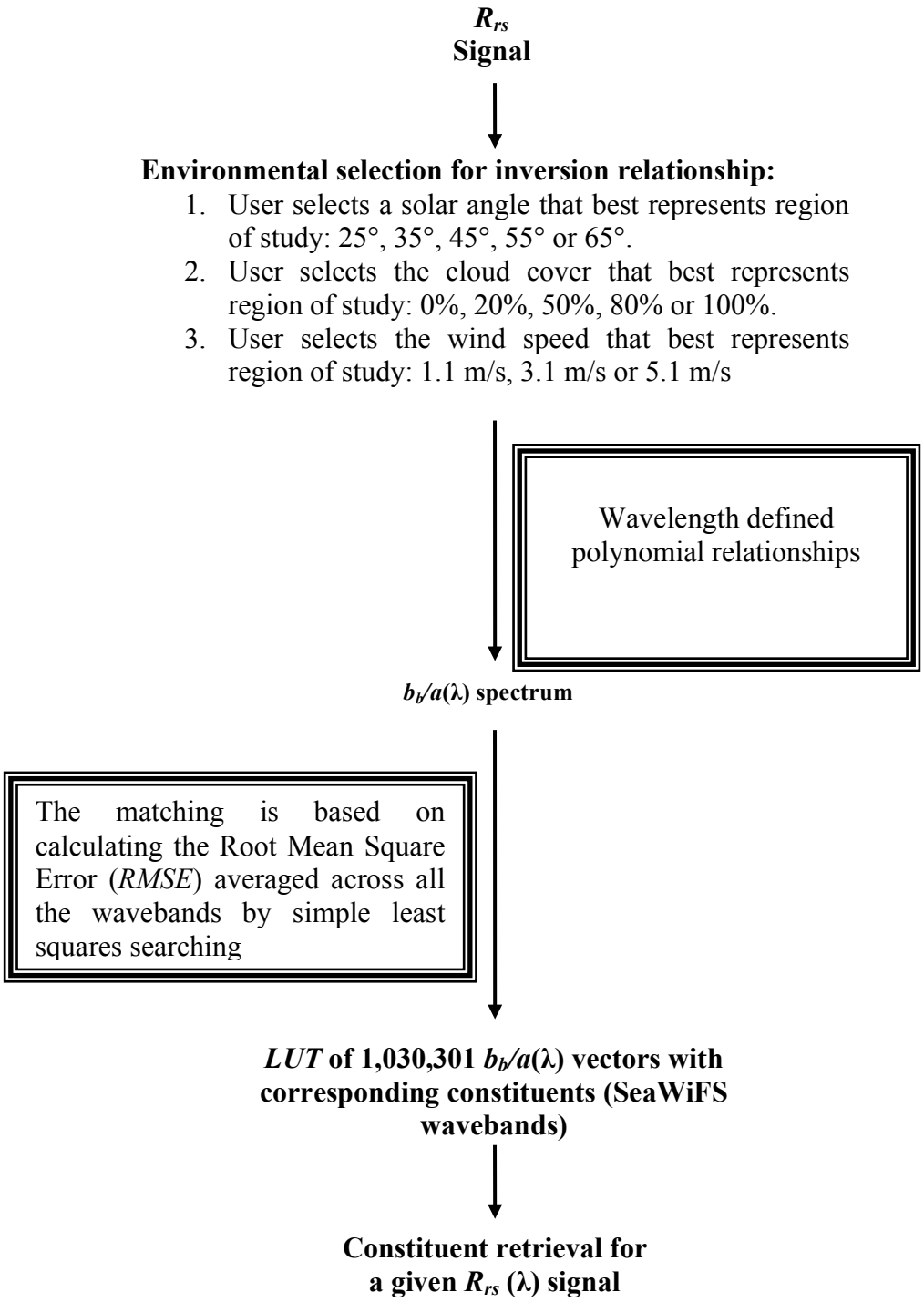

Figure 5.1: An overview of the spectral matching procedure that occurs for the inversion of an R_{rs} (λ) signal to obtain *OSM* concentrations.

The matching of seven-waveband "observed" vectors with entries in the *LUT* was based on the calculation of the root mean square error (*RMSE*) averaged over all wavebands. This measure of spectral distance differs from the one used by Defoin- Platel and Chami (2007) who calculated the maximum fractional difference waveband by waveband. For a single observed vector, the calculation of all *RMSE* values took a few seconds using MATLAB on a desktop computer: the time required could be significantly reduced by optimising the software used. The *RMSE* is calculated by:

$$x_{rmse}\left(\lambda\right) = \frac{\sqrt{\sum\left(x\left(\lambda\right)_{library} - x\left(\lambda\right)_{observed}\right)^2}}{\lambda_n} \tag{5.2}$$

Where λ_n is the total number of wavelengths (7 SeaWiFs), $x_{library}$ refers to each of the 7 wavelengths in the *LUT* of 1,030,301 b_b/a vectors and $x_{observed}$ is the unknown spectrum (at each wavelength), for which a constituent retrieval is required.

5.3. Variability in the $b_b(\lambda)/\ a(\lambda)$: R_{rs} relationship used for spectral matching.

The relationships between $b_b(\lambda)/\ a(\lambda)$: R_{rs} that are used to convert an R_{rs} signal to a b_b/a spectrum are based on 3rd order polynomials (equation 5.3) and are derived from the relationships displayed in figure 4.14. Polynomial expressions were used because it was discovered they gave slightly more accurate OSM retrievals (approximately 10%) than straight lines when tested using modeled data.

$$y = ax^3 - bx^2 + cx + d \tag{5.3}$$

With a, b, c and d calculated at each wavelength for the 75 environmental combinations that are given in table 3.3. Figure 5.7 and tables 5.1 to 5.4 show the variability that can arise with these parameters when the environmental conditions are altered. It is this variability that led to the inclusion of environmental selection in the spectral matching routine (figure 5.1) for the inversion of an R_{rs} signal. This means a relationship is selected for environmental conditions that best fit the conditions present when *in situ* or satellite data is recorded.

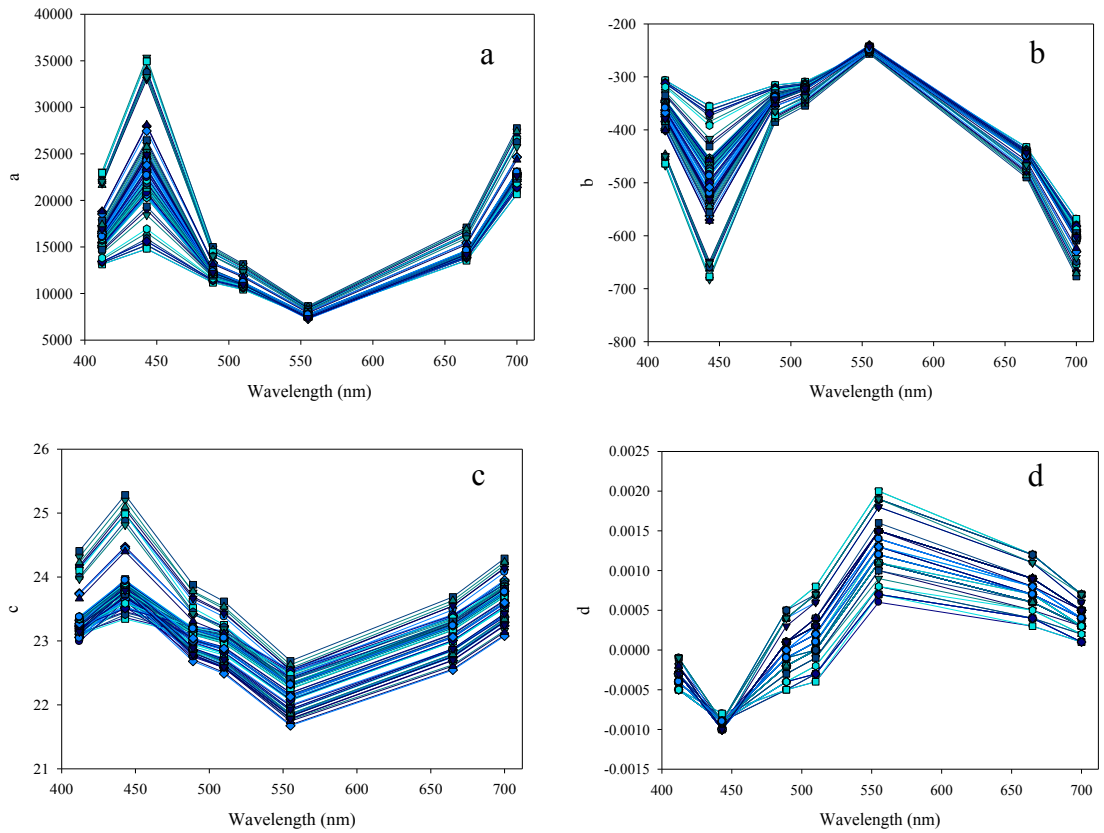

Figure 5.2: Variability that occurs between the polynomial components, *a*, *b*, *c* and *d* for the relationship between $b_b(\lambda)/\ a(\lambda)$and R_{rs} when the environmental conditions are altered. The combinations of environmental conditions used are given in table 3.3. The variation in these coefficients is up to 42% in *a*, 50% in *b*, 8% in *c* and 25% in *d*.

	412nm	443nm	489nm	510nm	555nm	665nm	700nm
Mean	16533.27	23320.35	11163	10419.7	7266.308	13532.66	20658.27
Range	10000.45	20575.52	3834.264	2743.881	1398.572	3564.398	7107.663

Table 5.1 Component a of the polynomial relationship.

	412nm	443nm	489nm	510nm	555nm	665nm	700nm
Mean	-367.238	-498.931	-385.346	-354.742	-256.76	-489.928	-676.936
Range	161.2049	327.7801	69.88304	45.67245	16.69289	57.42662	108.9139

Table 5.2 Component b of the polynomial relationship.

	412nm	443nm	489nm	510nm	555nm	665nm	700nm
Mean	23.34395	23.92223	22.68169	22.48619	21.67381	22.5453	23.07708
Range	1.418669	1.940391	1.196424	1.132953	1.013253	1.142184	1.213693

Table 5.3 Component c of the polynomial relationship.

	412nm	443nm	489nm	510nm	555nm	665nm	700nm
Mean	-0.00034	-0.00093	-0.00048	-0.00037	0.000646	0.000323	9.32E-05
Range	0.000427	0.000124	0.000987	0.001168	0.001356	0.000893	0.000649

Table 5.4 Component d of the polynomial relationship.

5.4 Discussion of alternative spectral matching techniques

This section discusses the various spectral matching algorithms that are available (i.e. stage three of the inversion process) and how they compare to the least squares matching routine actually used in this work, which is based on the calculation of the *RMSE* averaged across all the wavebands by simple least squares searching. Howari (2003) reviewed five different functions that could be used for spectral matching:

Absolute difference: $$M_{AD} = \sum \left| s_j - r_j \right| \tag{5.4}$$

Squared difference: $$M_{SD} = \sum \left(s_j - r_j \right)^2 \tag{5.5}$$

Squared derivative: $$M_{AD} = \sum \left| \Delta s_j - \Delta r_j \right|, \Delta s_j = s_j - s_{j-1}, \Delta r = r_j - r_{j-1} \tag{5.6}$$

Euclidean vector distance: $$M_E = \sum \left| s_j^2 - r_j^2 \right| \tag{5.7}$$

Correlation coefficient: $$M_{CC} = \frac{\left[\Sigma x_j y_j - \left(\left(\Sigma x_j \Sigma y_j \right) / N \right) \right]}{\left[\left(\Sigma x_j^2 - \left(\left(\Sigma x_j \Sigma x_j \right) / N \right) \right) \left(\Sigma y_j^2 - \left(\left(\Sigma y_j \Sigma y_j \right) / N \right) \right) \right]^{\frac{1}{2}}} \tag{5.8}$$

Where the M values are the calculated results for each of the matching functions, s_j and r_j are the normalised intensity values at point j for the sample and library spectra, respectively and x_j and y_j are the x and y values in the library and sample spectra respectively. In the comparison carried out by Howari (2003), the correlation coefficient performed the best, followed by the squared derivative, the Euclidean vector difference and then the absolute difference algorithm. However, the author concluded that any of the functions could be useful as an elimination tool, whereby a large search library could be reduced to a smaller quantity which could then be interpreted by alternative methods.

Work by Bissett (2006) on the interpretation of ocean colour data in terms of water column optical properties and bathymetry involved validation of a spectral matching and *LUT* technique for the inversion of hyperspectral reflectance spectra. In addition to equations 5.6 and 5.7, the functions listed below were considered in this work, but only the Euclidean vector distance (equation 5.7) was actually used.

Manhattan: $$\sum_{k=1}^{n}\left|x_{ik}-x_{jk}\right| \tag{5.9}$$

Chebyshev: $$\max_{k}\left|x_{ik}-x_{jk}\right| \tag{5.10}$$

Canberra: $$\sum_{k=1}^{n}\frac{\left|x_{ik}-x_{jk}\right|}{\left|x_{ik}\right|+\left|x_{jk}\right|} \tag{5.11}$$

Bray Curtis: $$\frac{\sum_{k=1}^{n}\left|x_{ik}-x_{jk}\right|}{\sum_{k=1}^{n}\left(x_{ik}+x_{jk}\right)} \tag{5.12}$$

Angular Separation: $$\frac{\sum_{k=1}^{n}x_{ik}.x_{jk}}{\sqrt{\sum_{k=1}^{n}x_{ik}^{2}\cdot\sum_{k=1}^{n}x_{jk}^{2}}} \tag{5.13}$$

Vector Distance Separation algorithms (5.9 – 5.12) and vector angle separation (5.13) can be used to measure the closeness of two spectra *i* and *j*, with x_{ik} representing an R_{rs} spectrum *i* at wavelength *k*. The work by Bissett (2006) focused on performing *k* nearest neighbour analysis (*kNN*) where *k* is the closest fitting spectrum that corresponds to a particular environmental parameter, such as *IOPs*, and where the retrieval is taken to be the mean of the most frequently occurring value of *k*. As well as classifying water bodies, this *kNN* analysis can be used for error estimation whereby, if the *k* values all correspond to the same environmental condition, or there about, it may be concluded that there is not a strong influence by noise and the retrieval will be correct, within a small error. Conversely, if there is a large variation in the *k* values, it may be presumed that one can be less confident in the validity of the retrieval.

Mobley *et al.* (2005) developed a spectrum-matching, *LUT* approach for the interpretation of ocean colour for the retrieval of specific environmental information (without ancillary data) that includes water column *IOPs* and bottom classification. The authors state that all required information is contained within an R_{rs} hyperspectral signal and therefore inversion of an R_{rs} signal would be expected to have a high accuracy of retrieval. They investigated the following spectrum-matching algorithms:

Least-squares matching of the absolute spectra:

$$LSQabs(i) = \sum_j \left\{ w(j) \left[R_{rs}(i,\lambda_j) - \dot{R}_{rs}(\lambda_j) \right]^2 \right\} \tag{5.14}$$

Least-squares matching of length normalized spectra:

$$\left| R_{rs}(i) \right| = \sqrt{\sum_j R_{rs}^2(i,\lambda_j)} \tag{5.15}$$

the quantity to be minimized is then:

$$LSQnorm(i) = \sum_j \left\{ w(j) \left[\frac{R_{rs}(i,\lambda_j)}{\left| R_{rs}(i) \right|} \frac{\dot{R}_{rs}(\lambda_j)}{\left| \dot{R}_{rs} \right|} \right] \right\} \tag{5.16}$$

Angle matching of length-normalised spectra:

$$\cos(\theta) = \sum_j \left\{ w(j) \frac{R_{rs}(i,\lambda_j)}{\left| R_{rs}(i) \right|} \frac{\dot{R}_{rs}(\lambda_j)}{\left| \dot{R}_{rs} \right|} \right\} \tag{5.17}$$

Least squares matching of offset spectra:

$$\min R_{rs}(i) = \min_{j} R_{rs}(i, \lambda_j) \tag{5.18}$$

The spectra are then compared using:

$$LSQoffset(i) = \sum_{j} \left\{ w(j) \left[\left(R_{rs}(i, \lambda_j) - \min R_{rs}(i) \right) - \left(\dot{R}_{rs}(\lambda_j) - \min \dot{R}_{rs} \right) \right]^2 \right\} \tag{5.19}$$

Where $\dot{R}_{rs}$ is the 'unknown spectrum to be matched, $R_{rs}(i, \lambda_j)$ represents the i^{th} spectrum in the library of known spectra and $w(j)$ is a weighting function to determine the quality of the matches. The authors found that these algorithms performed similarly with respect to the quality of matches obtained. Consequently, they concluded that the choice of the spectral matching algorithm, with modeled data, is not as important as may have once been perceived. However, they did not test this theory on application to real *in situ* data.

5.5 Comparison of the Euclidean and correlation coefficient algorithms with the least squares matching method for modeled data

To test the routine devised for converting an R_{rs} signal to a b_b/a vector, as well as the spectral matching method described in figure 5.1, modeled R_{rs} data were used to assess the quality of *OSM* concentration recovery. 396 R_{rs} signals were taken at random from the Hydrolight generated library for the following environmental conditions: solar angle 45°, cloud cover 0 % and wind speed 3.1 m/s. These spectra represented a range of possible signals from a modelled water body whose constituent concentrations lay within the limits employed in creating the library. The selected spectra were converted to b_b/a vectors and then matched to the library using the three algorithms given by equations 3.7, 5.5 and 5.6. Figure 5.3 displays the recoveries for *CHL*, *MSS* and *CDOM* for all three matching algorithms. The least-squares and Euclidean algorithms gave approximately the same results: the best recovery is observed for *MSS* with only a 1% maximum deviation from a perfect recovery, whereas *CHL* and *CDOM* show a larger deviation of up to 10% and 5% respectively, from a perfect recovery, indicated by their R^2 values. However, the correlation coefficient method performed poorly with deviations from a perfect recovery reaching 460% (when *CHL* levels were 0), 400% (when *MSS* levels were 0) and 90% for *CHL, MSS* and *CDOM*, respectively. Such poor performance would be expected to be degraded further when the correlation coefficient method was applied to real data.

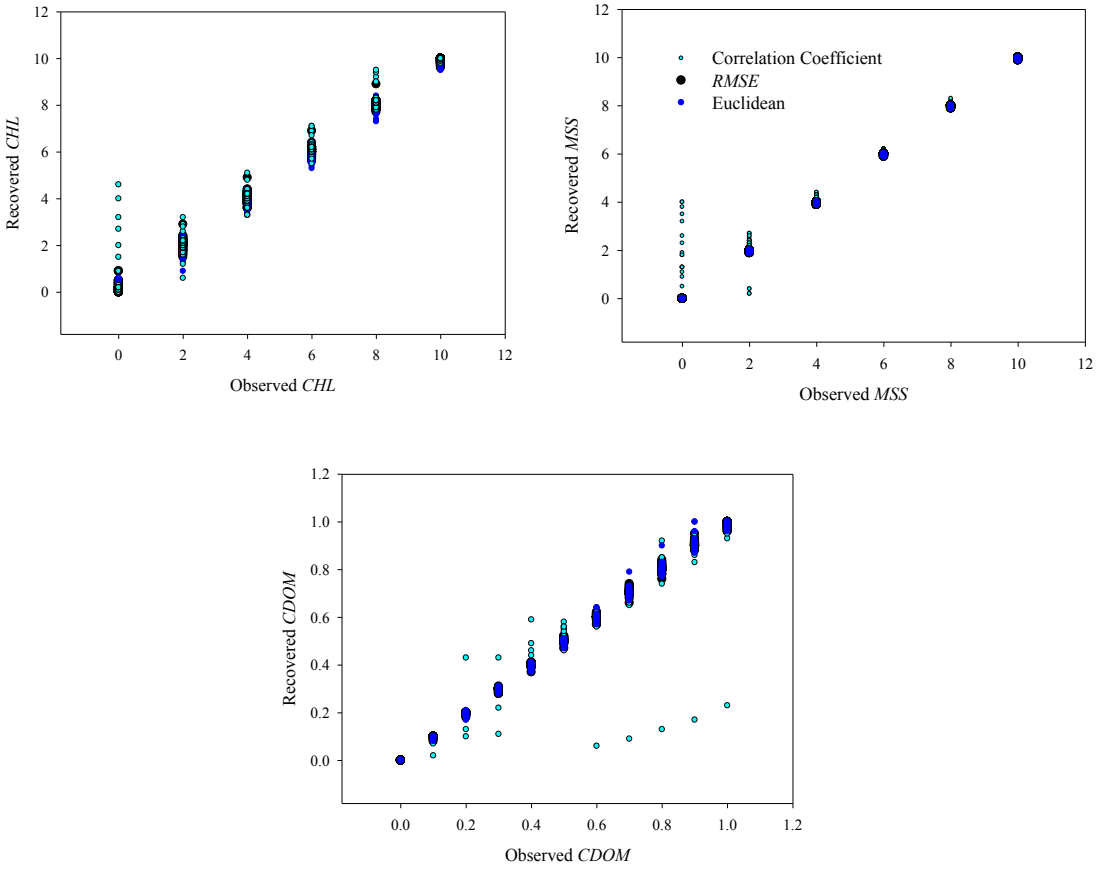

Figure 5.3. *OSM* retrieval from the spectral matching *LUT* approach for R_{rs} inversion. Three matching algorithms were tested on modeled R_{rs} spectra: least squares matching, Euclidean distance and the correlation coefficient algorithm.

a) Application of spectral matching to in situ SPMR data

The results for the least squares matching and Euclidean algorithm concur with the findings of Mobley *et al.* (2005), who showed that the choice of algorithm for the matching procedure is generally not critical. However, this conclusion was derived using modeled data. For the practical applications of these algorithms to real data, an re-assessment of their performance is required. Consequently, a comparison was made between the spectral matching algorithm used in this work (equation 3.7) and the

Euclidean algorithm (equation 5.5) using data collected using a SeaWiFS Profiling Multispectral Radiometer (SPMR). The Correlation Coefficient algorithm was excluded as it performed the poorest using modeled data. Figure 5.4 shows the recovery of *OSM* using the least-squares matching and Euclidean algorithm on *in situ SPMR* data collected on the Western coast of the UK. This data encompasses the areas of the Bristol Channel, Irish Sea and the Sound of Jura.

These recoveries show that the least squares matching method used in this work performs in a similar way to the Euclidean matching algorithm which has been used by other workers in the field. However, both algorithms show variable results for *OSM* retrieval, with the poorest recovery occurring for *CHL*. Chapter 6 investigates this problem in more depth.

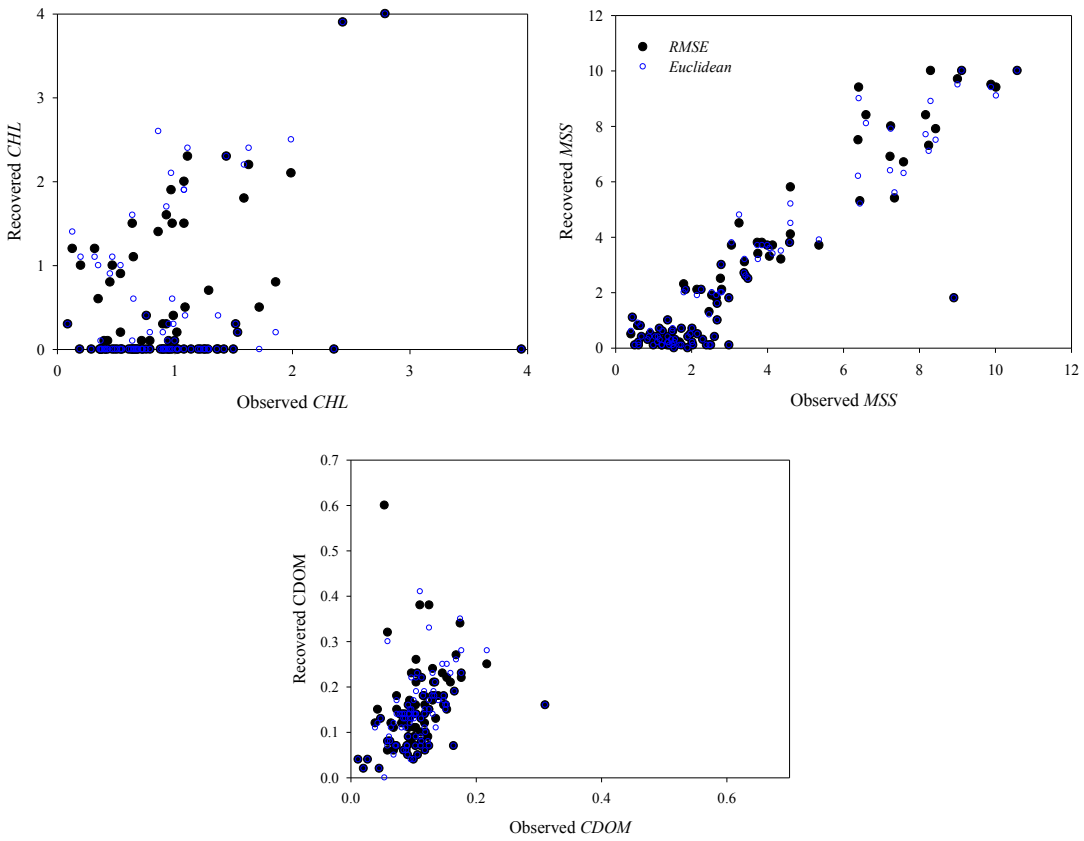

Figure 5.4. *OSM* retrieval for two different spectral matching algorithms: least squares matching and the Euclidean coefficient algorithm, using *in situ SPMR* data.

5.6 Comparisons of matching techniques in the presence of noise

If a spectrum were taken out of the b_b/a library and used as the 'observed' spectrum, the spectral matching routine would always obtain an exact match and a perfect constituent recovery for all three matching algorithms. It would therefore be expected that the 'recovered' spectrum would be identical to the observed spectrum and its associated *OSMs*. This provides a simple method for testing the matching routine at a basic level. However, since,

1. *in situ* data is not perfect and
2. the full matching routine used in this work requires an R_{rs} signal to be converted to a b_b/a spectra before it can even be matched to the *LUT*

The robustness of these matching routines was assessed by introducing artificial noise into to the b_b/a spectra. 344 b_b/a vectors were selected at random from the *LUT* and perturbed by applying noise independently to each waveband. The noise added was generated from a Gaussian distribution whose mean was equal to the initial b_b/a value and whose standard deviation was set to 5% of the mean. This percentage was selected because 5% corresponds to the target uncertainty for the recovery of water-leaving radiances from *SeaWiFs* and *MODIS* observations. However, this figure is exceeded by at least a factor of two in practice (Gregg *et al.*, 2009). The quality of the matches to the *LUT* are shown in figures 5.5 to 5.7. These results show that the introduction of noise results in poor performance of all matching algorithms. Overall, the least-squares matching algorithm performs the best and the Correlation Coefficient the worst, with a more significant deterioration occurring in *CHL* retrieval for all three algorithms.

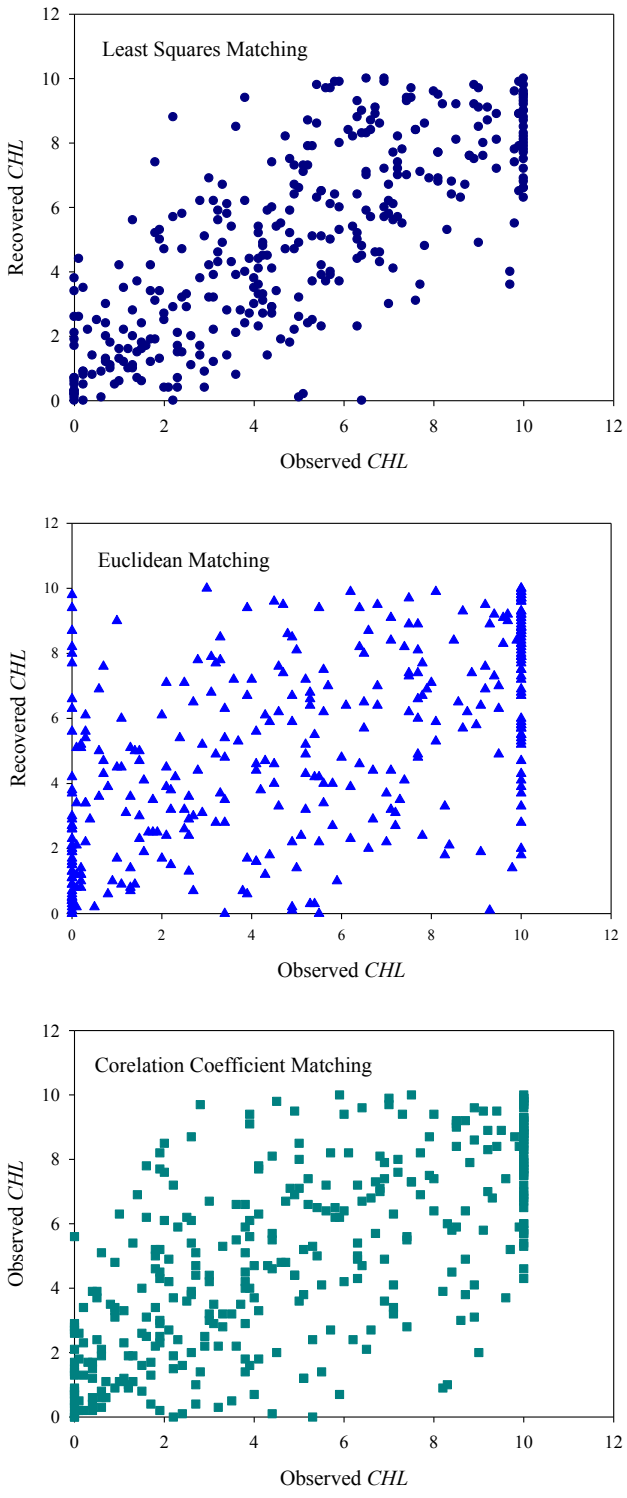

Figure 5.5. *CHL* recovery from modeled b_b/a spectra that were artificially perturbed by 5% to simulate noise. Three matching algorithms were used: Least-squares, Euclidean and the correlation coefficient algorithm.

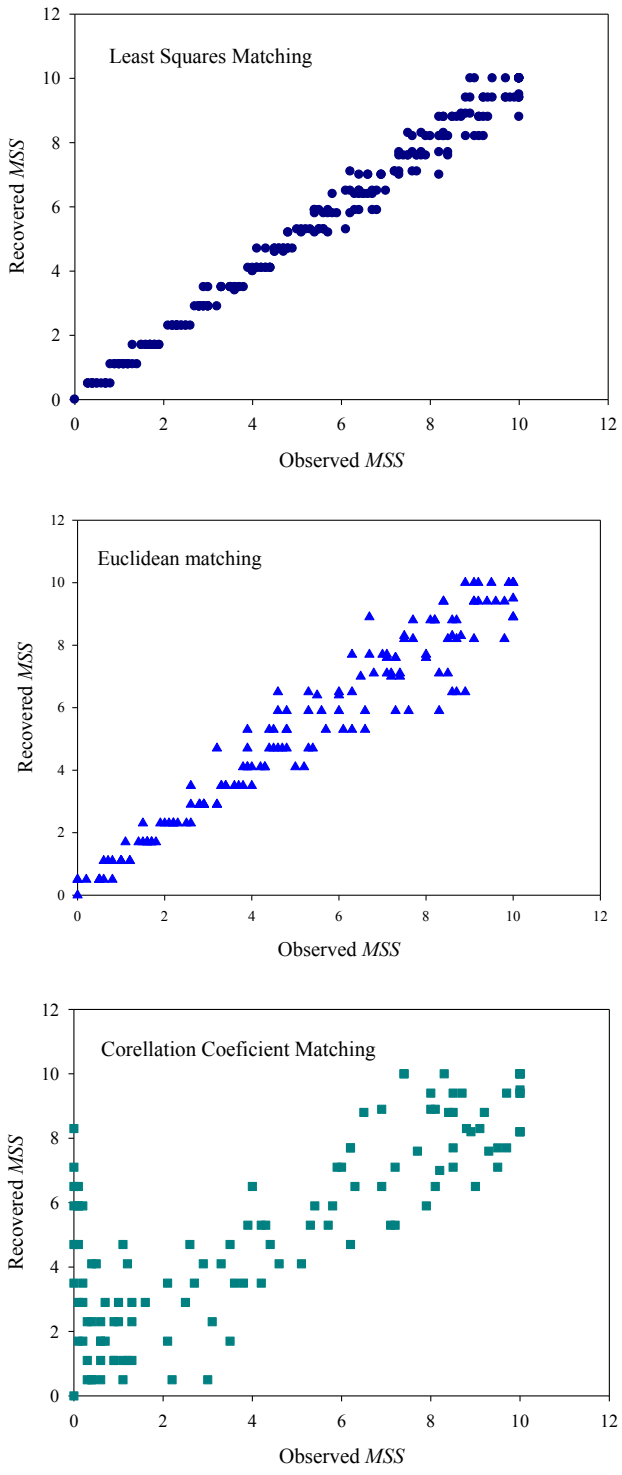

Figure 5.6. *MSS* recovery from modeled b_b/a spectra that were artificially perturbed by 5% to simulate noise. Three matching algorithms were used: Least-squares, Euclidean and the correlation coefficient algorithm.

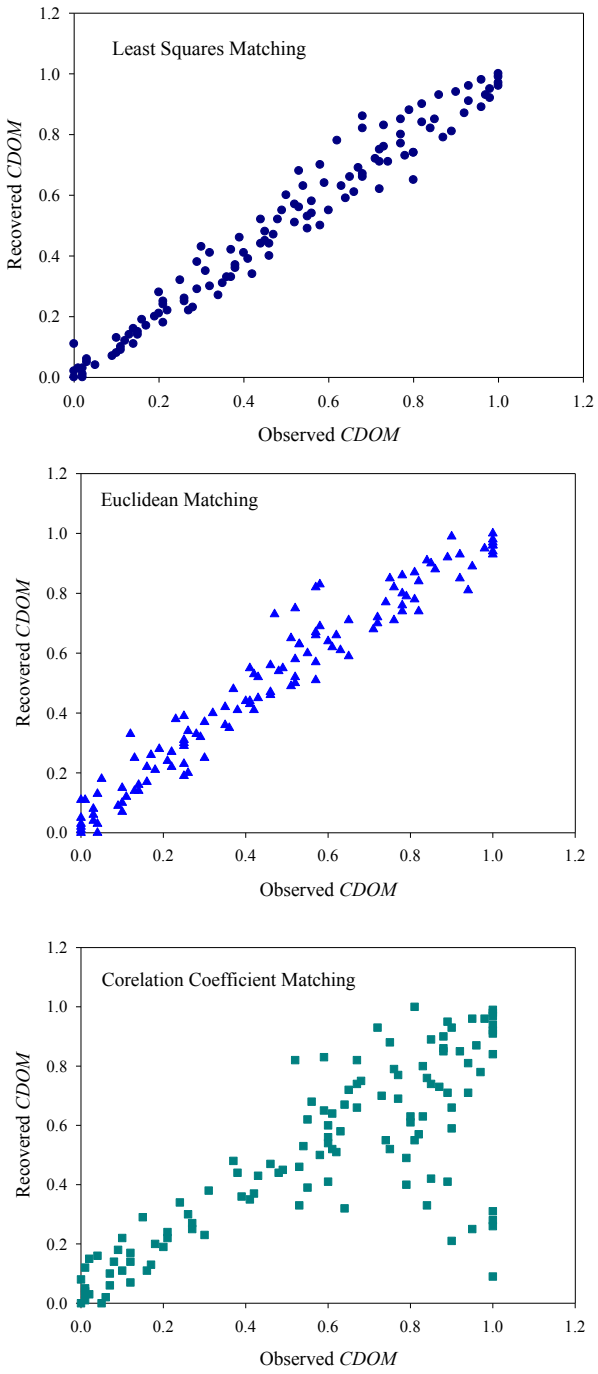

Figure 5.7. *CDOM* recovery from modeled b_b/a spectra that were artificially perturbed by 5% to simulate noise. Three matching algorithms were used: Least-squares, Euclidean and the correlation coefficient algorithm.

5.7 Effect of library resolution and library size on recovery time

Library (or *LUT*) resolution is a critical factor in spectral matching. In the work discussed here, the inversion of an R_{rs} signal is performed with the aim of retrieving the *OSM* concentration that best corresponds with the input spectrum. Problems can occur if the input signal is generated by *OSM* concentrations that fall in the intervals between values represented in the *LUT*. Therefore, to optimize the inversion results, a *LUT* with a very high resolution was generated in Matlab, resulting in over one million $b_b(\lambda)/\, a(\lambda)$ vectors. The generation of such a high resolution *LUT* using Hydrolight would place unrealistic demands on computer time, and was the fundamental reason that an approach based on a $b_b(\lambda)/\, a(\lambda)$ *LUT* was developed in the course of this project.

With such a high resolution *LUT*, it was important to evaluate the effects on the time required for the spectral matching process. Figure 5.8 shows the effects of increasing library size on the time it takes to match one spectrum. While there is a significant decrease in time for the smaller library sizes, these *LUT* sizes are too small to achieve good results. The benefits of saving only one second with a smaller resolution is lost when the quality of matches returned is poor. In fact, as the number of spectra to be matched in a single run increases, the average time per spectrum drops to around 1.87 seconds. Matches were performed on a 32bit 1.80GHz Intel Pentium Dual CPU (E2160) computer with 3GB of RAM (DDR2 @ 500Mhz), and increasing computer specifications would be expected to decrease the search time.

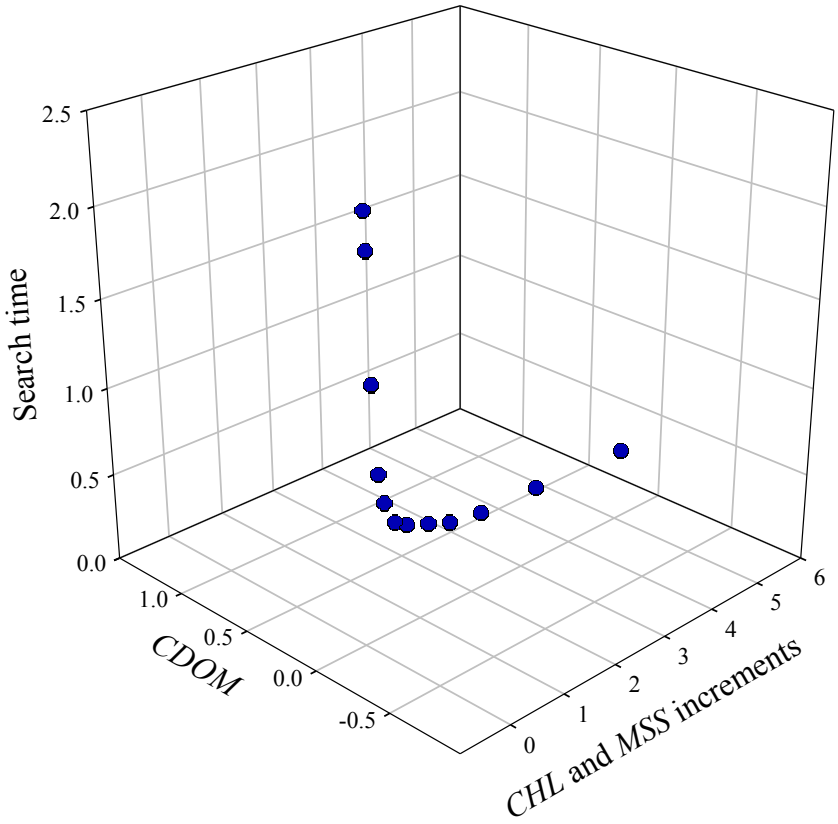

CHL mg/m^3 and *MSS* g/m^3 increment	*CDOM* increment	Matrix dimensions (*CHL x MSS x CDOM*)	Library size	Time (Seconds)
0.1	0.1 m^{-1}	101x101x101	1030301	2.31
0.14	0.1 m^{-1}	71x71x101	515150	2.10
0.2	0.1 m^{-1}	51x51x101	262701	1.41
0.28	0.1 m^{-1}	36x36x101	169781	0.92
0.39	0.1 m^{-1}	26x26x101	68276	0.74
0.57	0.1 m^{-1}	18x18x101	32724	0.61
0.8	0.1 m^{-1}	13x13x101	17069	0.57
1.2	0.1 m^{-1}	9x9x101	8181	0.51
1.6	0.1 m^{-1}	7x7x101	3636	0.47
2.2	0.1 m^{-1}	5x5x101	2525	0.43
3.3	0.1 m^{-1}	3x3x101	909	0.42
5.1	0.1 m^{-1}	2x2x101	404	0.40

Figure 5.8. Graph showing the effects of increasing the library resolution on the time it takes to match one spectrum in Matlab using a least squares matching algorithm. A tabulated output of the results is given below the graph. Although the increment size changed, the range remained the same: : 0-10 mg/m^3 for *CHL*, 0-10 g/m^3 for *MSS* and 0-1 m^{-1} for *CDOM*.

It is also important to consider the effects of the library resolution on the quality of *OSM* recovery. Figure 5.9 shows a graphical representation of *LUTs* of different resolutions, all of which encompass concentration ranges of 0-20 mg m^{-3} for *CHL*, 0-20 g m^{-3} for *MSS* and 0-1 m^{-1} for *CDOM*.

First, an 11 x 11 x 11 matrix with concentration intervals of 2, 2 and 0.1 for *CHL*, *MSS* and *CDOM* respectively provides a library size of 1331 *OSM* concentrations.

Second, a 6 x 6 x 11 matrix with larger concentration intervals of 4, 4 and 0.1 for *CHL*, *MSS* and *CDOM* respectively provides a library size of 396 *OSM* concentrations. The consequence of employing this second matrix for spectral matching is that there is greater chance that a desired concentration will fall between the matrix values than they would with the larger dimensioned matrix.

The effect of *LUT* resolution on *OSM* retrieval was tested by evaluating the quality of matches when 100 b_b/a spectra that represent the range of concentrations present in both matrices, were matched to the different libraries Figure 5.10 presents the results of testing the two matrices. When the input spectrum fell between matrix entries, the next closest match was selected. As can be seen from the graphs in figure 5.5, this can result in very poor *OSM* recoveries.

a) Final Library Resolution

Data collected by the Strathclyde University optics group suggests that *OSM* concentrations in Western UK shelf seas, from where the *SIOPs* used in this work were derived, are typically below 10 mg m^{-3} for *CHL*, 10 g m^{-3} for *MSS* and 1 m^{-1} for *CDOM*. Values recorded above these concentrations accounted for less than 4% of the total data set. Consequently, the *LUT* employed for the remainder of this work was constructed using ranges of 0-10 mg/m^3 for *CHL*, 0-10 g/m^3 for *MSS* and 0-1 m^{-1} for *CDOM*. The concentration intervals were 0.1, 0.1 and 0.01 for *CHL*, *MSS* and *CDOM*, respectively. However, one benefit of an *LUT*-based spectral matching approach is that the

concentration ranges and resolution of the *LUT* can be easily altered for other ranges. For example Babin *et al.* (2003) reported concentrations that reached up to 40 mg m^{-3} for CHL and 73 g m^3 for *MSS* in European waters and Fang *et al.* recorded *CDOM* values that reached 1.41 m^{-1} in the Pearl River estuary, China.

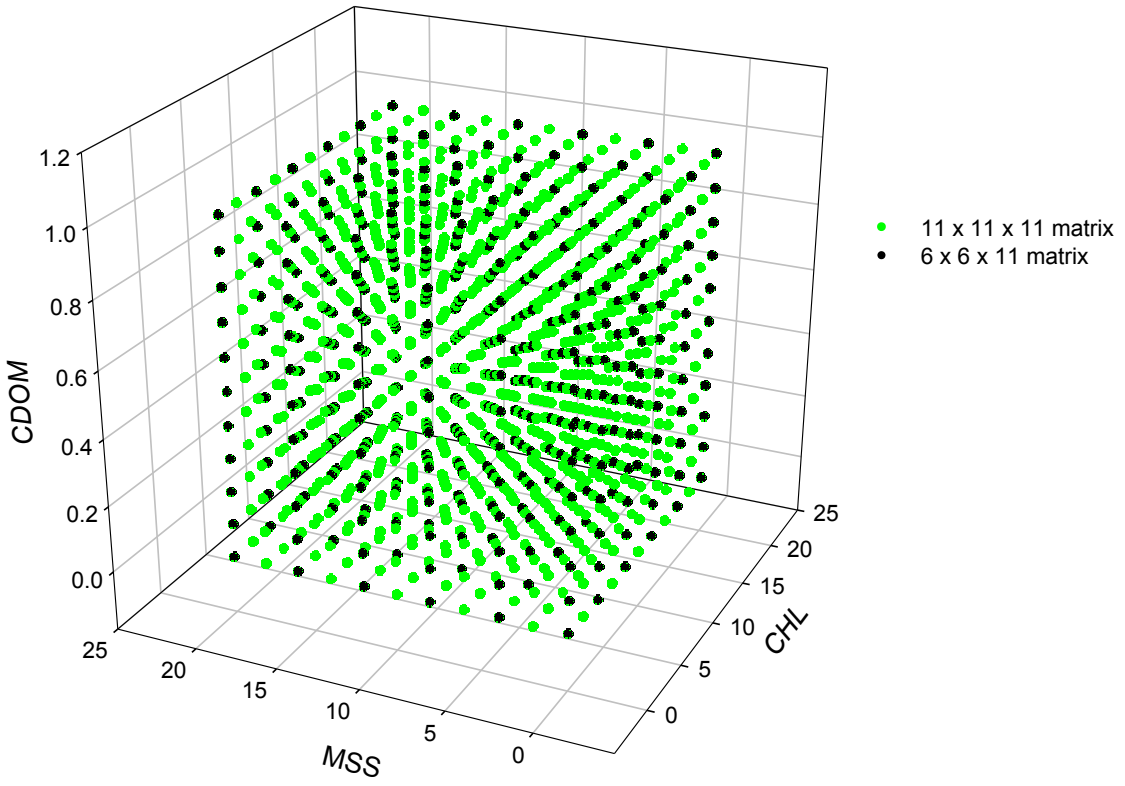

Figure 5.9. Matrix resolution when the concentration intervals are increased. The black dots represent the resolution of the smaller matrix whereas the green dots indicate the larger matrix and display the effects of increasing resolution as the gaps between the black dots are now filled with *OSM* entries.

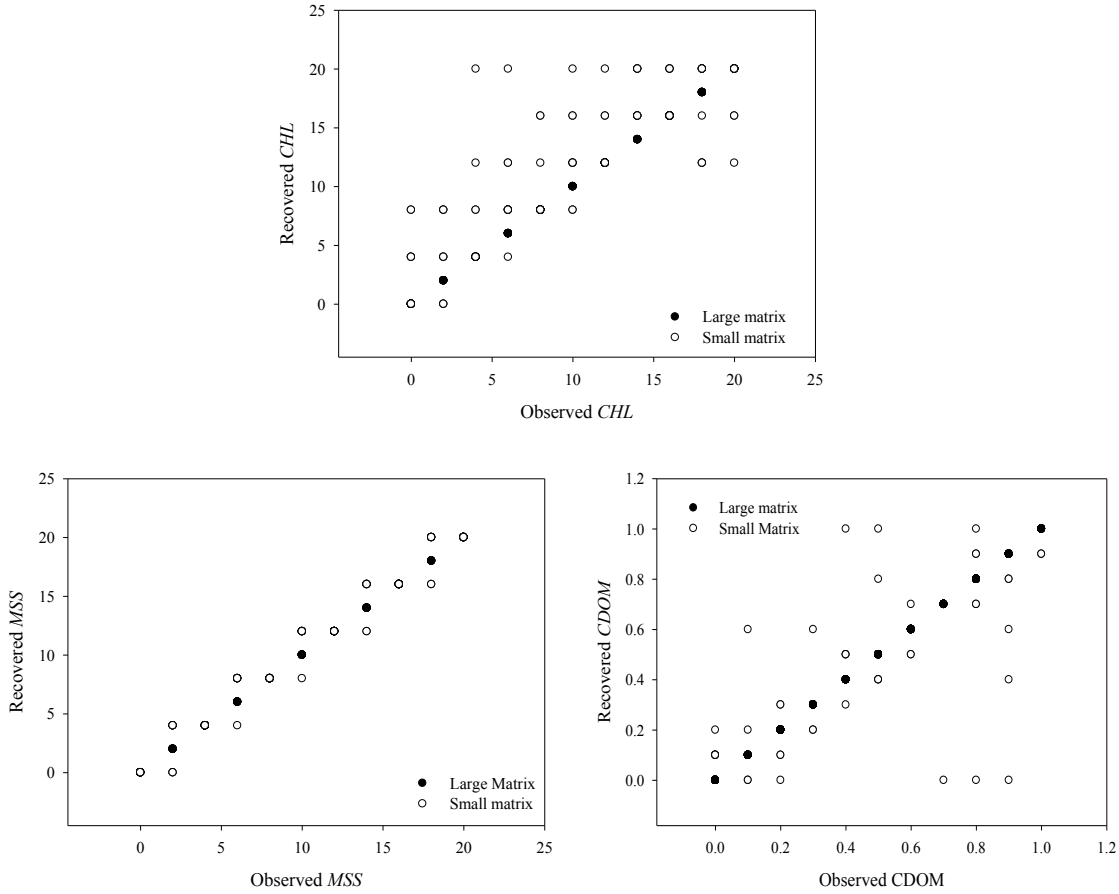

Figure 5.10. Graphs showing recoveries of *OSM* when the library resolution is altered. The larger matrix contained entries for all 'unknown' spectra, whereas the smaller library had gaps and therefore the 'unknown' spectra fell between the library entries. Both libraries cover the same concentration range; 0-20 mg/m^3 for *CHL*, 0-20 g/m^3 for *MSS* and 0-1 m^{-1} for *CDOM*.

5.8 Summary of chapter 5

i. There are a number of algorithms available to perform spectral matching using a look up table of pre-computed values.

ii. The matching algorithm used in this work (least squares) showed comparable retrieval results to the widely implemented Euclidean matching algorithm.

iii. Increased resolution of the *LUT* increases the search time required. Such time penalties could be overcome by increasing the available computer processing speed.

iv. The spectral matching process for the inversion of an R_{rs} signal and the retrieval of *OSM* concentrations has been summarized in figure 5.5.

v. The conversion of an R_{rs} to a b_b/a spectrum can be done using 3rd order polynomial relationships that are generated to represent different environmental conditions based on solar angle, cloud cover and wind speed.

vi. The *LUT* and spectral matching procedure adopted in this work provides greater flexibility in its application to changing data sets than other, more complex techniques. For example, it can be quickly adapted to changes in optical properties that occur with spatial variability.

Chapter 6

Introduced errors for modeled data and implications of *SIOP* variability

The reported occurrence of multiple solutions to the inversion of remote sensing reflectance, R_{rs}, signals is important when attempting to recover the concentrations of optically significant materials (*OSMs*) from optically complex shelf seas. This chapter has sought to quantify the severity of this problem in a number of ways:

1. Artificially perturbing 'observed' spectra and comparing the quality of matches returned with the non-perturbed spectra
2. Determining the effects of increased observational errors on the recovery of *OSMs* from optically complex waters.
3. Quantifying the degradation of recovery when the acceptance criterion is relaxed i.e. when the *R.M.S.E* taken to be representative of a good match, is increased.
4. Comparing results derived from data to which artificial noise has been added with the *OSM* recoveries from *in situ SPMR* data to determine if the spread of recoveries observed with *in situ* data can be explained by errors of observation.
5. Examining the variability in potential solutions by looking at their 'spectral neighborhood'.
6. Discussing the ambiguity that can occur when the simple algorithm which is used in this work is applied to areas where the *SIOPs* differ from those used to create the fundamental inversion relationships.

6.1 Introduction of Statistical Noise to 'Observed' data

Artificial errors in the observational measurements were simulated in this study through the introduction of artificial noise, using a Gaussian distribution, independently to each waveband. This statistical method of applying noise meant that the mean was set to equal the "true" value (at each wavelength) and the standard deviation was varied as a test of sensitivity (to represent different amounts of 'noise'). Therefore, to introduce statistical noise into test spectra:

1. The $b_b/a(\lambda)$ vectors were selected at random from the already pre-computed *LUT* described in previous chapters.
2. The noise level was selected from a Gaussian distribution whose mean was equal to the initial $b_b/a(\lambda)$ value and whose standard deviation was set at a variable percentage (0% to 5%) of the mean. A 5% error corresponds to the target uncertainty for the recovery of water-leaving radiances from SeaWiFs and MODIS observations, but this figure is exceeded by at least a factor of two in practice (Gregg *et al.,* 2009)). The level of perturbation is synonymous with the level of noise that is applied independently to each waveband.

The consequence of this perturbation is a series of spectra that are distorted versions of the original. A visual representation of this distortion is given in figure 6.1.

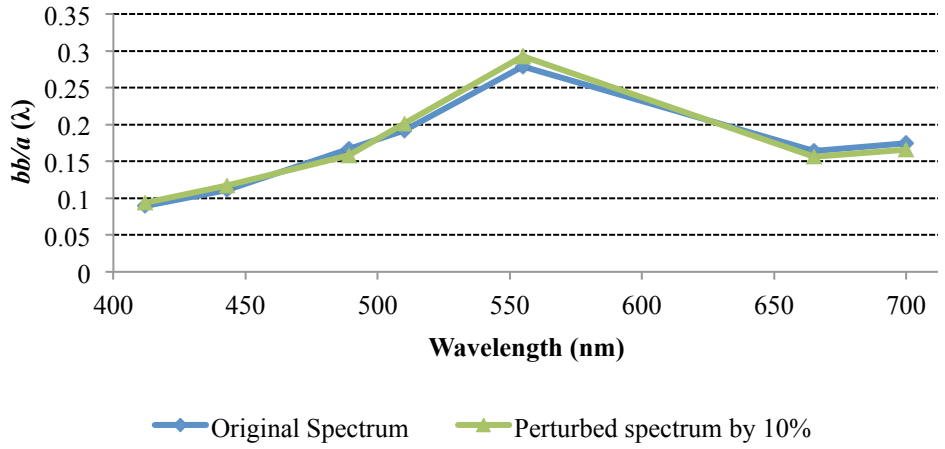

Figure 6.1. Example of a statistically perturbed $b_b/a(\lambda)$ vector.

The use of modeled data means the constituent concentrations used to generate the original spectra are known. Consequently, the quality of constituent retrievals obtained (from the signal to which noise has been added) can be compared and quantified with respect to the original spectrum.

The quality of the matches obtained using the pre-computed *LUT* entries is assessed by calculating the *RMSE* for a b_b/a vector (averaged across all wavebands). For the purposes of assessment in this chapter, matches were generated with acceptance criteria increasing from an *RMSE* of 0 to 0.01 in increments of 0.0001. The results of introducing statistical noise and the effects this has on the retrieval of *OSM*, by spectral matching are presented in the following sections.

6.2 Effect of measurement errors and acceptance criteria on the number of matches returned (modeled data).

One hundred $b_b/a(\lambda)$ vectors were selected at random from the pre-computed *LUT* and perturbed by a varying degree of noise, as described in section 6.1. Figure 6.2 shows the combined effect of noise and acceptance tolerance on the number of matches obtained from the b_b/a vectors. If an exact replica of the observed spectrum was found in the library, then only one match was returned with the minimum *RMSE* of 0. The points plotted in figure 6.2 represent an average of the 100 randomly selected spectra used in this test

Obtaining an single exact match when the *RMSE* was set to 0 was an important result, which

(i) Indicated that no intrinsic ambiguity was found in the six-waveband matching process.

(ii) Confirmed that there was a unique relationship between $b_b/a(\lambda)$ vectors and the *OSM* concentration triplets used to generate the *LUT*. Given the unique mapping of *OSM* concentration triplets on $b_b/a(\lambda)$ vectors, the recovery of *OSM* concentrations becomes a trivial operation for modeled data in the absence of added noise.

The results showed that the number of potential matches increased rapidly when the acceptance tolerance was increased (an *RMSE* of 0.0024 produced 618 matches for noise-free spectra). The addition of random noise to the "observed" spectrum reduced the number of matches obtained for a given acceptance interval because a higher proportion of *OSM* recoveries for the modified spectra fell outside the acceptance criteria. Quantifying the number of $b_b/a(\lambda)$ matches did not however, give any indication of the quality of *OSM* concentrations that were recovered, and this aspect is investigated next.

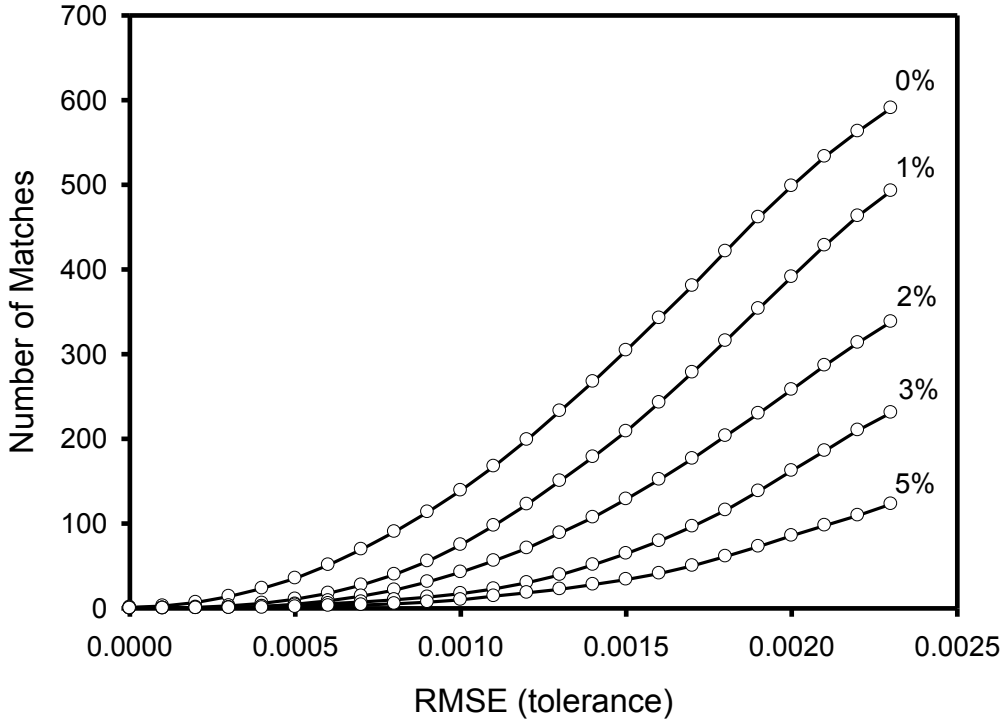

Figure 6.2. Number of matches returned within a given acceptance interval (*RMSE*) for b_b/a vectors to which Gaussian noise had been added in the range 0% to 5 %.

6.3 Effect of errors of observation on the recovery of *OSM* concentrations

a) Quality of *OSM* retrieval in conjunction with the introduction of noise

For brevity, the recovery of *CHL* concentrations is used as an example in this section: other *OSMs* followed a very similar pattern. As in section 6.2, a set of 100 $b_b/a(\lambda)$ vectors were selected at random from the *LUT* and perturbed in the way described in Section 6.1. To assess the effect of observational errors on the recovery of *OSM*, the *LUT* was searched and the match with the lowest *RMSE* for each vector accepted. Figure 6.3 illustrates the degradation in accuracy of *CHL* recovery in response to added noise for the 100 randomly selected $b_b/a(\lambda)$ vectors. Perfect recoveries were achieved only when zero noise was added.

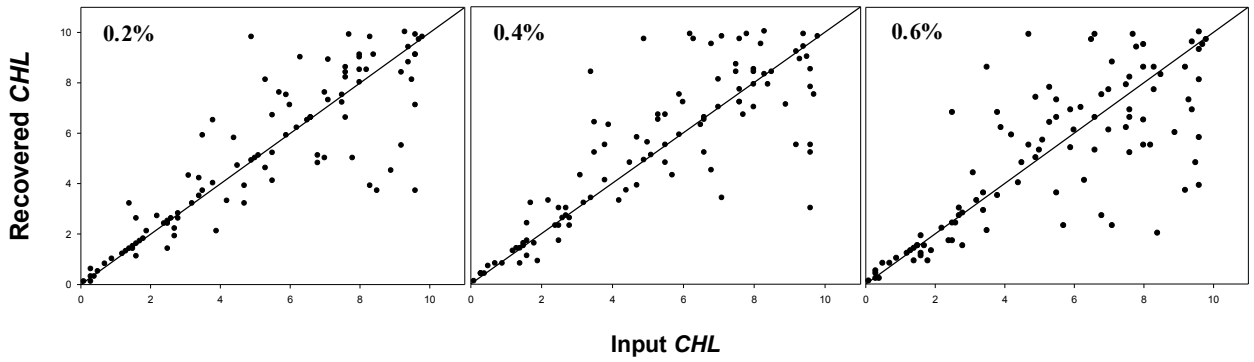

Figure 6.3. Degradation in *CHL* recovery as noise is added to the observed $b_b/a(\lambda)$ vector with standard deviations (from left to right) of 0.2%, 0.4% and 0.6% of the mean value. For each recovery, the *LUT* match with the lowest *RMSE* was selected.

The average *RMSE* values for the 100 "observations" provide a useful measure of the quality of the matches achieved. These values were 0.00026, 0.00043 and 0.00063 for

standard deviations of 0.2%, 0.4% and 0.6%, respectively. In order to gain a clearer picture of the significance of errors of observation for the inversion process, the process was repeated for a further 3000 entries randomly selected from the *LUT*. These spectra were subjected to the same perturbation and matching as previously described. Figure 6.4 shows how the average percentage error in *CHL* recovery increases with the standard deviation of the added noise, expressed as a percentage of the true value. The line drawn through the points is of the form $y = 11.4 \ln(x) + 34$.

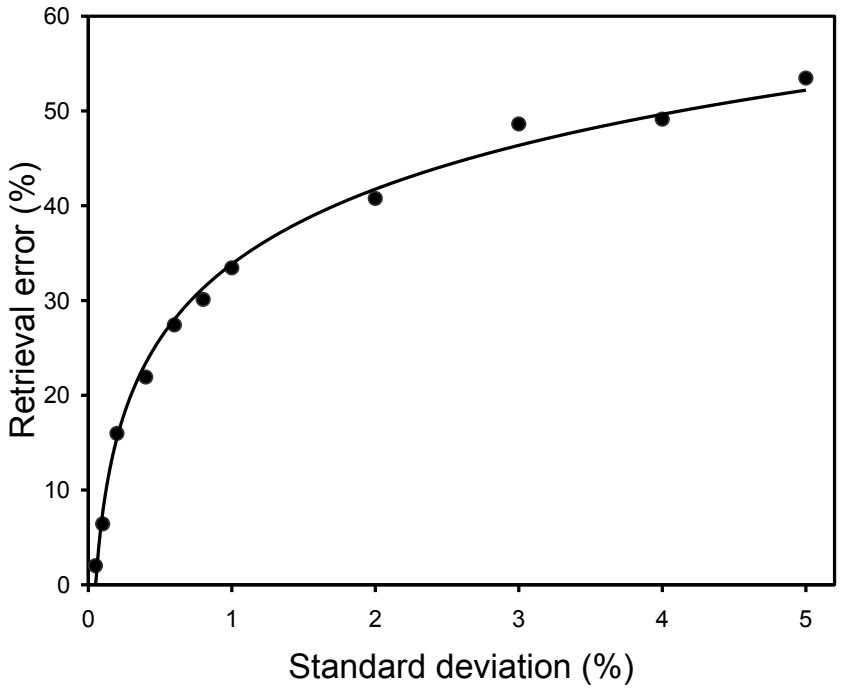

Figure 6.4 Variation in the average percentage error for *CHL* recovery for 3000 randomly selected spectra as the standard deviation of the added noise increases.

b) Mapping the observed errors in *OSM* recovery with modeled data onto *in situ SPMR* data.

The objective of this section was to assess the magnitude of the errors in constituent retrievals that occurred when *in situ* R_{rs} signals from shelf seas were used for spectral matching. This enabled a comparison to be made with the retrievals obtained from the artificially perturbed spectra, described above, that represented realistic levels of observational uncertainty. Due to the persistent cloud cover over the Western UK Shelf Sea, it is difficult to obtain high quality satellite images. Consequently, *in situ* R_{rs} signals were derived from radiometric profiles obtained by deploying an *SPMR* (Satlantic) at 96 stations in the Irish Sea and Bristol Channel. This is the geographical area from which the *SIOPs* used to construct the spectral library were derived. The errors of observation present in the *SPMR*-derived signals, estimated using regression analysis for stations where multiple profiles were carried out, were taken to be 10% for each waveband. Figure 6.5 show results for both modelled and measured recoveries of *CHL*, *MSS* and *CDOM* using the standard spectral library. The filled circle symbols show recoveries for 396 modelled R_{rs} spectra with 10% RMS random noise added. The open symbols show recoveries for 96 R_{rs} spectra derived from *SPMR* profiles. The most obvious conclusion is that *CHL* is affected more strongly than *MSS* or *CDOM* by the addition of noise to spectral observations. Equally interesting, however, is that fact that the constituent recoveries from the field data fall within the error boundaries predicted by adding realistic noise levels to the modelled data.

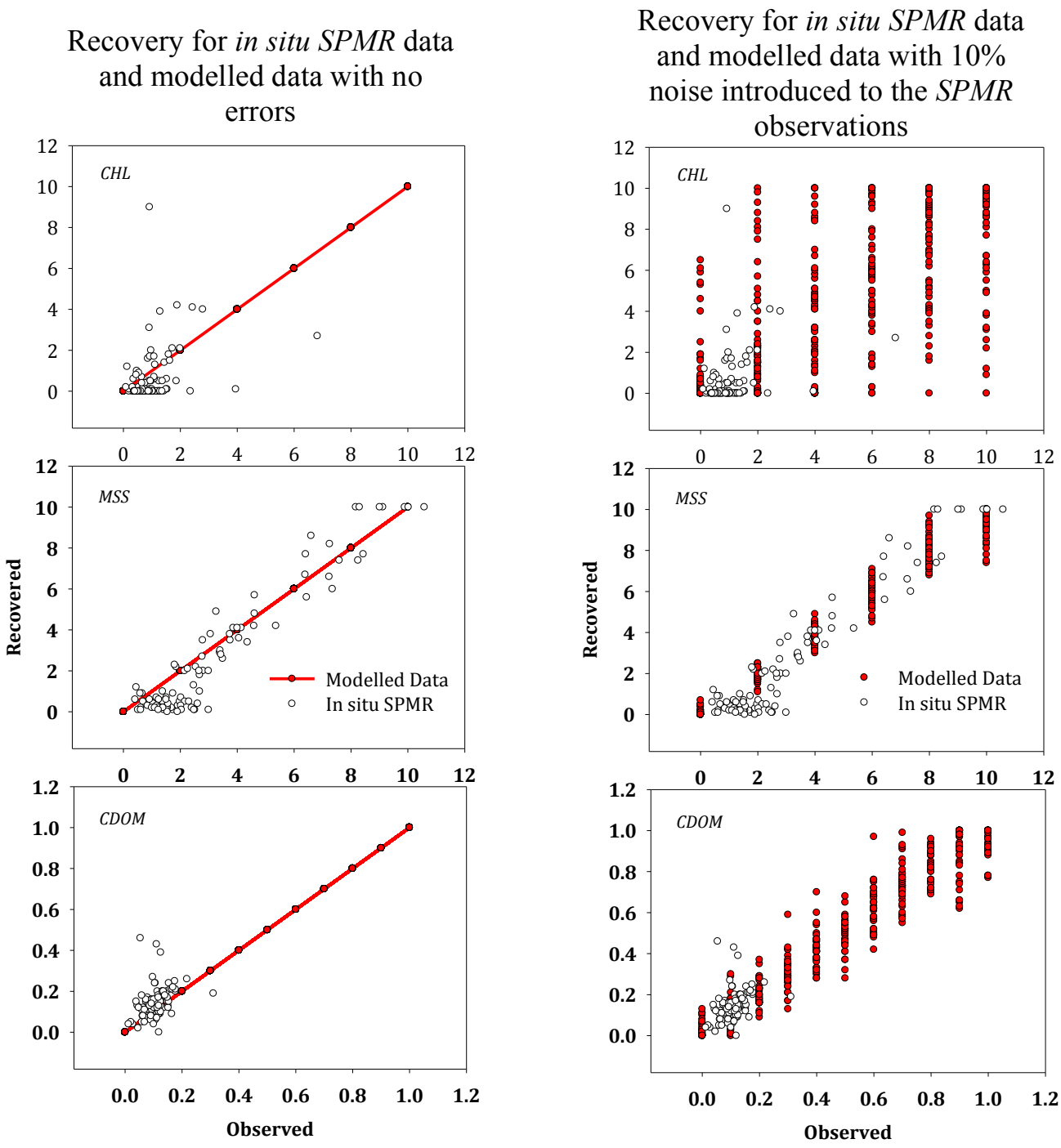

Figure 6.5. Constituent retrieval for *in situ SPMR* data and modeled data with artificial noise (representative of observational noise) introduced.

6.4 Spectral neighbourhood

The term spectral 'neighbourhood' was briefly introduced in chapter 1, when particle swarm optimization (*PSO*) was discussed. With respect to spectral matching, it refers to an area or group that provides potential solutions to an optimization problem. This technique can be very useful when the management of large data sets is required. A prime example of this is the deconvolution process of R_{rs} signals described in this work, where the 'problem' could be significantly reduced if the first step of the process involved application of the spectral neighbourhood theory, whereby the size of the data set is first reduced in size as opposed to seeking a single answer immediately. In addition to this, it can be used to explore the problem of ambiguity in the inversion process. As it is not known *a priori* what shapes the spectral neighbourhoods will assume as the acceptance criteria are relaxed. This work has shown that they generally appear as expanding single clusters, which implies that the range of possible solutions remains in the vicinity of the actual value. It could be the case that the spectral neighbourhood is less well behaved (for example it could have split into multiple clusters) which would make the inversion process subject to much larger errors. In the present context, the *RMSE* can be used to determine the spectral neighbourhood of potential solutions to R_{rs} inversion. Figures 6.6 a. and b. display the effect of increasing the *RMSE* acceptance criteria on the size and shape of spectral neighbourhood clusters in a three-dimensional space defined by b, a and b_b/a.. The plots show that the potential size of neighbourhoods at each wavelength increases (demonstrated from a change in colour from blue at the centre to red at the extremities) as the acceptance of an *RMSE* close to zero is relaxed. This could be considered as a crude method that enables the reduction of a very large dataset quickly to allow more refined methods to interrogate the data further and seek a single answer.

Qiu and Hancock's (2006) work in pattern recognition involved performing matching and cluster analysis based on spectral neighbourhood partitions. Their approach however, involved applying neighbourhoods to the data to be matched using the Fiedler-

vector of the Laplacian matrix to decompose data into neighbourhoods for matching and cluster analysis. The Fiedler vector is the eigenvector that corresponds to the second smallest eigenvalue of the Laplacian matrix, which is a matrix representation of a graph (Bailey *et al.*, 1995). The authors describe the neighbourhood in terms of a node, *i*, surrounded by other nodes i.e. the neighbourhood, connected by edges in the graph. The author's diagrammatical representation of this is given in figure 6.7. The objective of their approach was to weight each node by a level of significance at the centre of a neighbourhood, following the fielder vector defined path, selecting central nodes based on this weighting factor.

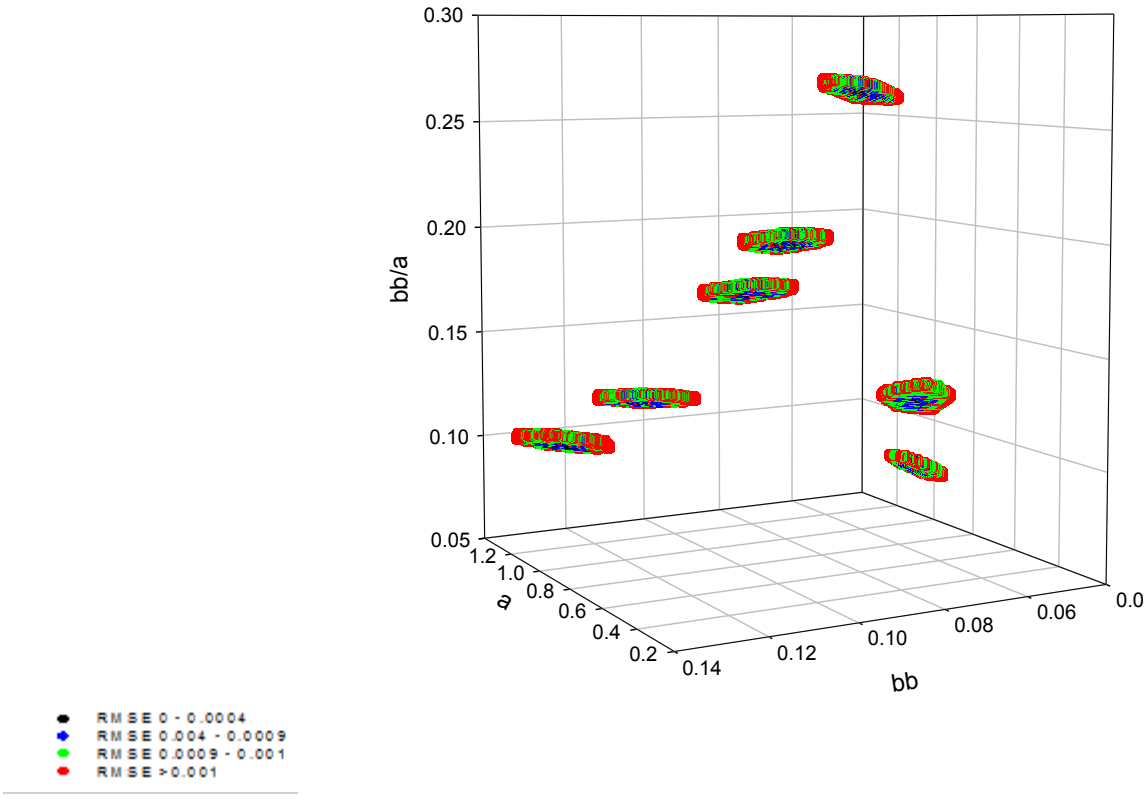

Figure 6.6. a) The effect, across the SeaWiFs wavelength, of varying the spectral neighbourhood as defined by the *RMSE*. b) Higher resolution view of the spectral neighbourhood, at 489nm, as the strictness of the *RMSE* fit to zero is relaxed.

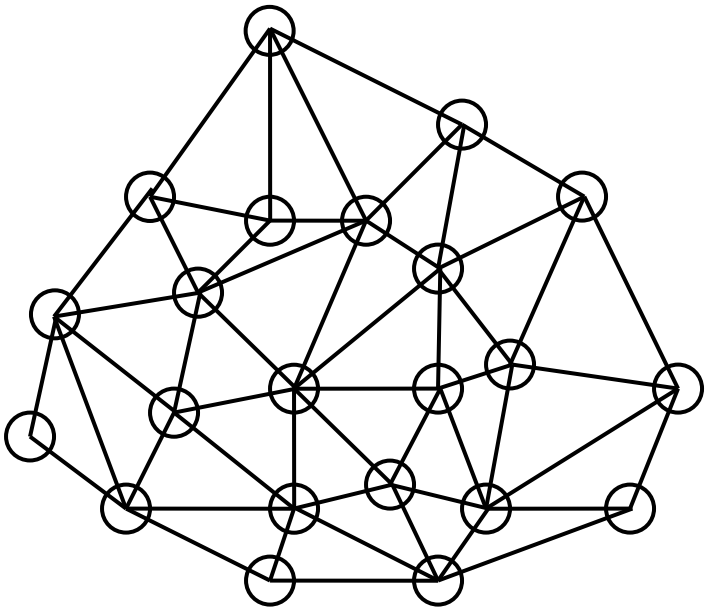

Figure 6.7. Characterization of neighbourhoods (Qiu and Hancock, 2006).

Figure 6.8 shows the variation that can occur in the constituent retrieval of *CHL* and *MSS* when the spectral neighbourhood, defined by the *RMSE*, is increased. This figure demonstrates the potential for the variability that can occur within a spectral neighbourhood using least squares matching and shows a wider distribution of potential solutions the recovery of CHL compared to *MS*S..

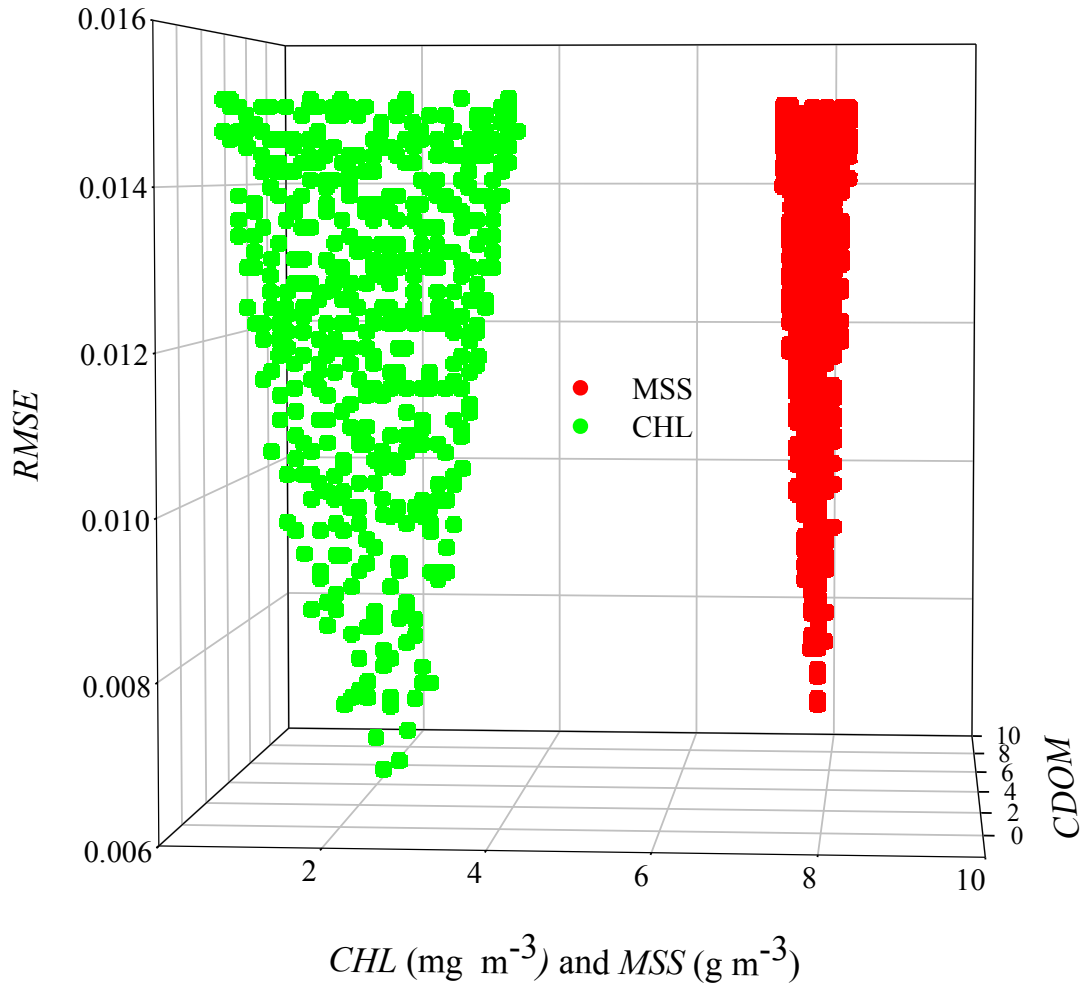

Figure 6.8. Calculation of the *RMSE* for recoveries obtained by using least squares spectral matching. The variability that occurs with the constituent retrieval within a spectral neighbourhood is evident and represents the increase in acceptance of the *RMSE*, i.e. values that are further away from zero are accepted. The *CDOM* variations are assumed to be negligible for the purpose of demonstrating how spectral neighbourhoods may appear.

6.5 Potential errors arising if a spectral matching inversion algorithm is applied without considering the differences in specific optical properties between phytoplankton taxa

Phytoplankton play an important role in determining the optical properties of the ocean, Given the existence of approximately 5000 known species of marine phytoplankton (Hallegraeff, 2003), it is important to assess the degree of variability in the specific absorption and backscattering coefficients of phytoplankton taxa in different water regions. This is an important aspect of ocean optics because the effects different species have on the interaction of light with the seawater can affect the robustness of remote sensing inversion algorithms (Mill and Nu, 1998). Consequently, there have been numerous studies of the magnitude and spectral shape of the specific absorption coefficients of different phytoplankton species. Although the *SIOPs* can have similar shapes if the phytoplankton are from the same taxonomic group, it is widely accepted that there can be wide variations between groups and consequently geographical locations (Morel and Gentili, 1993; Bricaud *et al.*, 1995). Suzuki *et al.* (1998) studied the differences that can arise between the chlorophyll specific absorption spectra, $a^*CHL(\lambda)$, of phytoplankton in the North Pacific Ocean as a result of the differences in the phytoplankton pigment composition, noting the association of higher values at warmer locations. Likewise, Bricaud *et al.* (1995) investigated a^*CHL variability using 815 spectra from different regions of the world ocean, where concentrations ranged from 0.02 to 25 mg m^{-3}. This work revealed ranges of 0.18 to 0.01 $m^2\,mg^{-1}$ for a^*CHL (at 440nm), with decreasing variability in eutrophic waters and Mill and Nu (1998) observed a^*CHL values with ranges of 0.020-0.056 $m^2\,mg^{-1}$ (at 440 nm) and 0.013-0.020 m^2 mg (at 674 nm) in the Gulf of California. The backscattering coefficient has shown similar variability for different phytoplankton taxa with variations of backscattering efficiencies ranging from 0.0023 to 0.081 (at 470 nm) (Vaillancourt *et al.*, 2004). Due to this potential variability, it is likely that the success of standard operational algorithms depends on the use of appropriate *SIOPs*. A potential side effect of using inappropriate *SIOPs* is the over estimation of *CHL* (Loisel *et al.*, 2008). Consequently, a modeling

study was conducted on the sensitivity of constituent recovery using least squares spectral matching involving *SIOPs* derived in the laboratory for five different phytoplankton species.

a) The ambiguity that arises when *SIOPS* from 5 different species of Phytoplankton are used

The chlorophyll-specific absorption and scattering coefficients, from cultures grown at Strathclyde University, were obtained for five species of phytoplankton: *Prymnesium parvum*, *Rhinomonas reticulata*, *Phaeodactylum tricornutum*, *Isochrysis galbana* and *Dunaliella primolecta* (Craig, 2000). Chlorophyll-specific backscattering was estimated using a b_b/b ratio of 0.0128 that was representative of phytoplankton dominated waters (Loisel *et al.*, 2007). Figure 6.9 shows how the *CHL* specific absorption and backscattering coefficients varied for each of the phytoplankton species, with the *SIOPs* used to generate the b_b/a spectral library included for comparison.

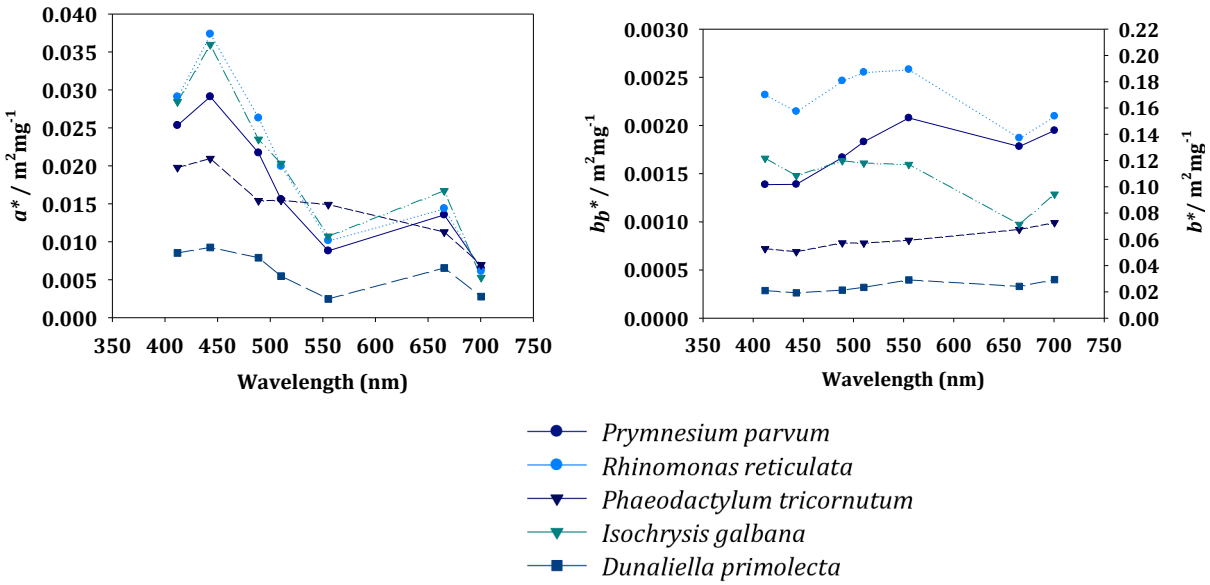

Figure 6.9 Chlorophyll-specific absorption and backscattering coefficients for five phytoplankton species. The chlorophyll-specific absorption coefficient was obtained from cultures grown at Strathclyde University and the specific backscattering was estimated using a b_b/b ratio of 0.0128.

The species-specific *SIOP*s were used to generate b_b/a spectra for water with *CHL* concentrations of 2, 4, 6, 8 and 10 mg m^3. No *MSS* and *CDOM* were included. These synthetic spectra were then matched to the original b_b/a library which was generated using *SIOPs* derived for UK west coast waters. Constituent retrievals deviated from the perfect recovery obtained when the matched spectrum was derived from the *SIOPs* used to create the library, although a linear relationship was obtained for three of the five phytoplankton species (figure 6.10). There is an approximate factor of five variations between the species due to mismatches. These results emphasize the importance of the selection of appropriate *SIOPs* if the performance of the spectral matching technique is to be optimized, even in Case 1 waters.

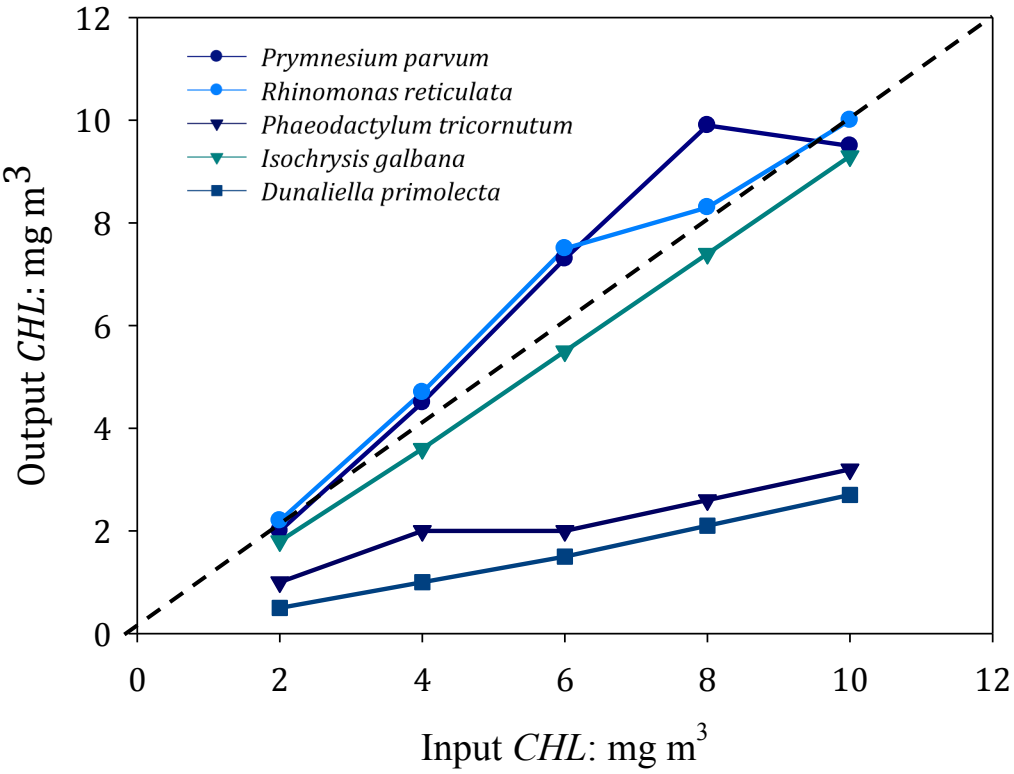

Figure 6.10. *CHL* recovery for spectra generated using *SIOPs* for five phytoplankton taxa. The 1:1 (dashed) line is the consequence of matching b_b/a spectra derived from the library *SIOPs*.

b) Distinguishing phytoplankton species from space.

In an attempt to determine if different phytoplankton species produced remote sensing signals that were sufficient to allow their discrimination in the clearest (Case 1) ocean waters, R_{rs} spectra for the five species of phytoplankton have been plotted in figure 6.11. It would appear that the significant variability observed between the *SIOPs* of these phytoplankton species has also been replicated in the remote sensing signals. Consequently, this result offers the possibility that discrimination in more optically complex waters may be possible. However, observational noise must be considered as well as other particulates that effect the absorption and scattering properties of light. These additional influences may make discrimination more complex than this initial result implies. To some extent, consideration of additional particulates may provide insight as to why the inversion algorithm used in this work, spectral matching by calculation of the *RMSE*, performs the poorest for *CHL* recovery. Obviously this is a highly topical subject in ocean colour interpretation studies and requires considerable investigation. The physiological (morphology and size) differences between different species and how this effects their spectral characteristics must also be considered.

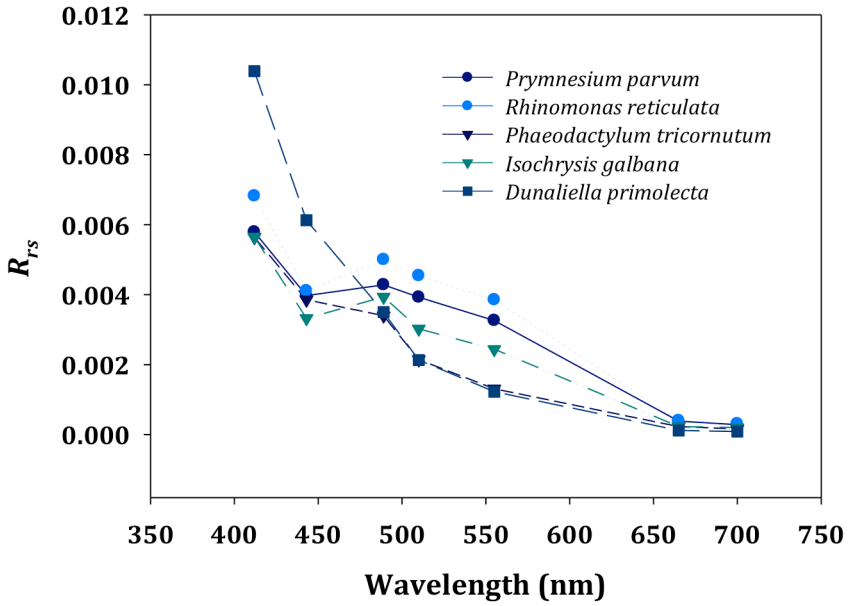

Figure 6.11. The remote sensing signals for five different species of phytoplankton, a typical satellite observational error is approximately 10% (Gregg *et al.*, 2008).

6.6 Discussion

The performance of the spectral matching routine for the recovery of *OSM* concentrations has been efficiently demonstrated using a *LUT* of b_b/a vectors. This work has shown that with a perfectly defined and modeled system, the spectral matching model produces exact retrievals and no ambiguity exists in the inversion process. The addition of Gaussian noise to the observed spectra and the relaxation of the acceptance criteria, based on the *RMSE*, accounted for two potential sources of ambiguity. The introduction of statistical 'observational' noise leads to a rapid degradation in constituent retrieval despite only small amounts of noise being introduced (figure 6.2). In addition to this, poor constituent retrieval occurs when b_b/a spectra, derived from *SIOPs* representing different phytoplankton taxa, are matched with a b_b/a library constructed using Western UK coast *SIOPs*. Finally, the spectral matching model had had partial success (figure 6.4) when applied to real *in situ SPMR* data. In this case, the *in situ* R_{rs} signals were measured in the area from which the *SIOPs* used to create the b_b/a library were derived. This work has confirmed the sensitivity of a simple spectral matching model to observational noise, and it can be concluded that deriving unambiguous *OSM* concentrations with this spectral matching routine is unlikely in optically complex waters. However, the availability of supplementary knowledge such as restricted ranges of constituent concentrations may help to reduce errors in constituent recoveries. In addition to this, hyperspectral data could improve the quality of recoveries in this type of inversion through spectral matching and also provides the scope to select optimum wavelengths. If any spectral matching approach is to be pursued, then a great deal of further work is required on the creation of *LUTs* using *SIOPs* that best represent the region of study. It should be noted that the application of any inversion method for satellite data must take into consideration the uncertainties that could potentially be introduced, including the atmospheric correction from the top of the atmosphere that is introduced to water reflectance data.

6.7 Chapter 6 Summary

i. The addition of random noise to the "observed" spectrum reduced number of matches produced for a given acceptance interval.

ii. The average percentage error in *CHL* recovery increases with the standard deviation of the added noise.

iii. *CHL* is affected more strongly than *MSS* or *CDOM* by the addition of noise to spectral observations.

iv. The potential size of spectral neighbourhoods at each wavelength increases as the acceptance of an *RMSE* close to zero is relaxed.

v. *CHL* specific absorption and backscattering coefficients vary significantly for each of the five phytoplankton species: *Prymnesium parvum*, *Rhinomonas reticulata*, *Phaeodactylum tricornutum*, *Isochrysis galbana* and *Dunaliella primolecta*.

vi. Constituent retrievals for the five Phytoplankton species deviated from the perfect recovery obtained when the matched spectrum was not derived from the *SIOPs* used to create the library, although a linear relationship was obtained for three of the five species investigated.

vii. The sensitivity of a simple spectral matching model to observational noise has been demonstrated.

Chapter 7

Case Studies in the Irish Sea, Bristol Channel and The Clyde

The robustness of the remote sensing inversion algorithm, using spectral matching, has been demonstrated so far using modelled data and *in situ SPMR* data. The *SIOPs* that were used for the analysis up to this point have been representative of the UK Western shelf sea and were calculated using a series of linear and multiple linear regressions. This chapter will investigate the effects on constituent recovery when using *SIOPs* that are specific to a region of study in contrast to the ones that are representative of a larger area. In addition to this, the effects of using regionally derived *SIOPs* to generate new relationships between R_{rs} and b_b/a will be investigated to ascertain the potential for the use of a 'one fits all' relationship. The case study regions used in this chapter to investigate regionally derived relationships, shall be the Irish Sea and the Bristol Channel. Finally, the quality of recoveries for the Irish Sea, Bristol Channel and The Clyde will be demonstrated using the *SIOPs* representative of the Western UK Shelf Sea. It must be noted that a selection of the graphs in the following section contain data points that are not normally distributed. Consequently, the R^2 can be misleading where there is in fact, an over-estimation of reality.

7.1 Effects on the $R_{rs}(\lambda):b_b(\lambda)/a(\lambda)$ relationships using regionally calculated *SIOPs*

The premise of this work is that the relationships that have been derived between R_{rs} and $b_b(\lambda)/a(\lambda)$ are relevant to different regions of interest. Furthermore, it is important to ascertain if the relationships that have been established are valid in regions where the *SIOPs* are different from the original *SIOPs* used to quantify the relationships. Consequently, before applying the inversion method to real *in situ* data, Hydrolight was used, in the same way as described in chapter 3, to generate new relationships using *SIOPs* derived specifically for:

1. The Irish Sea
2. The Bristol Channel

These relationships, wavelength by wavelength, are displayed in figure 7.1 together with the originally derived relationships representative of the Western UK Shelf sea. The results show that changing the *SIOPs* does not significantly affect the relationship between R_{rs} (λ) and b_b/a (λ). Consequently, the previously established procedure for recovering b_b/a (λ) from R_{rs} (λ) can be applied, with reasonable confidence, to regions where the *SIOPs* are different from those used in the original derivation.

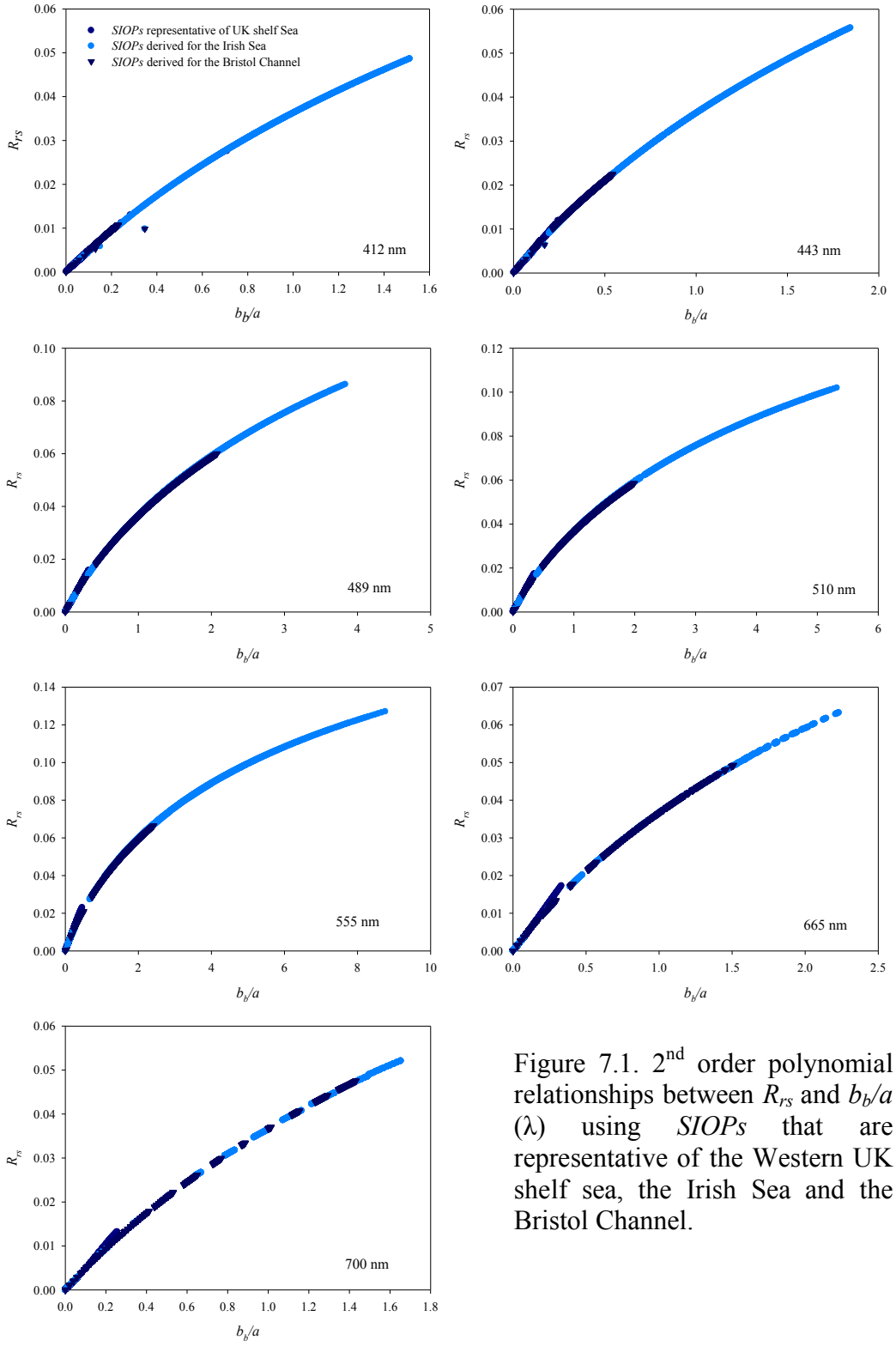

Figure 7.1. 2nd order polynomial relationships between R_{rs} and b_b/a (λ) using *SIOPs* that are representative of the Western UK shelf sea, the Irish Sea and the Bristol Channel.

7.2 The Irish Sea

This section assesses the quality of constituent recoveries obtained when the *SIOPs* used to create the *LUT* are derived specifically for the Irish Sea. Previous results using modelled data have shown significant degradation in constituent recoveries, particularly for *CHL* retrieval, when artificial 'noise' was added to the inputs. It is anticipated that such results will be reflected, if not exacerbated, when the R_{rs} (λ) spectral matching inversion algorithm is applied to *in situ* data.

A particularly poor recovery was observed for *CHL* with R^2 values of 0.001. The mineral recovery was significantly better (at least up to 6 g m^{-3}) and is illustrated in Figure 7.2. *CDOM* recoveries resulted in an R^2 value of 0.1 due largely to the frequent recovery of a '0' concentration. The poor retrievals of these constituents could be due to the reduced data set used when regional relationship SIOPs were derived, or to the presence of concentration combinations that were not included within the resolution of the *LUT*.

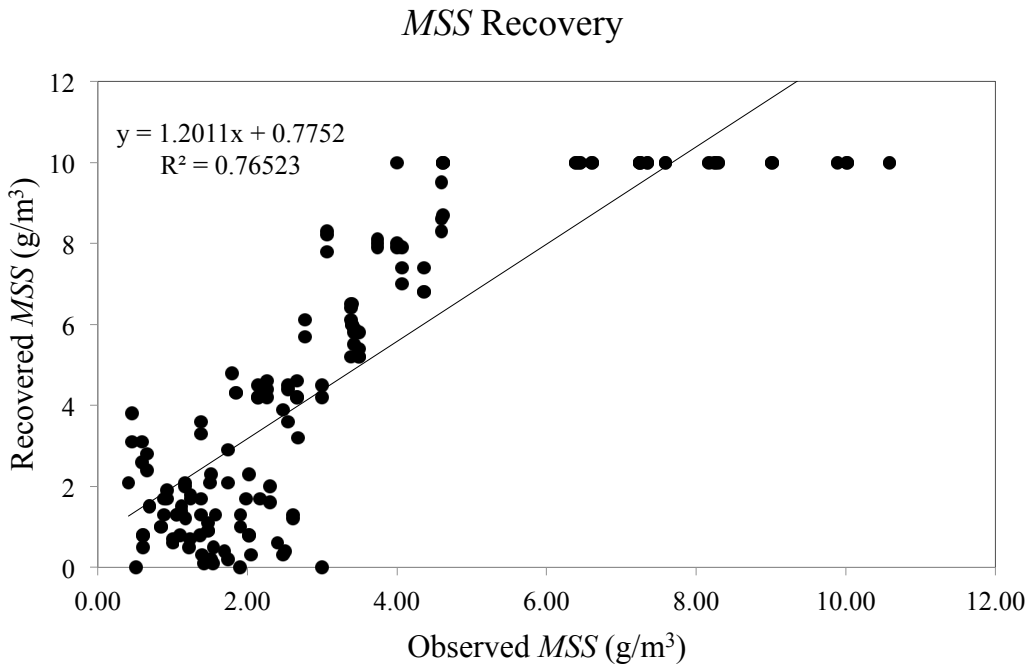

Figure 7.2. *MSS* recoveries for the Irish Sea *in situ SPMR* data. The spectral matching involved a *LUT* table that was created using *SIOPs* derived specifically for the Irish Sea.

7.3 The Bristol Channel

The results from applying the spectral matching procedure, to *in situ SPMR* data from the Bristol Channel were similar to those obtained for the Irish Sea. There was poor retrieval for all constituents with R^2 values of 0.18 for CHL, 0.54 for MSS and 0.00 for *CDOM*. The inversion relationships and *LUT* were derived specifically for the Bristol Channel. A possible reason for such a poor recovery is the variability in the type of waters that were sampled. A region that is to be specifically modelled should contain a small range of water types. However, as is seen in Figure 3.1, measurements in the Bristol Channel cover coastal sites where there is high sediment re-suspension as well as significantly less turbid offshore waters. The *SIOPs* for the Bristol Channel included measurements from both these types of area and therefore, may be too varied for the purposes of specific regional modelling.

7.4 Quality of constituent retrieval using *SIOPs* representative of the Western UK Shelf Sea

The previous section presented the results of applying spectral matching inversion using relationships created with *SIOPs* specific to the region of study. An alternative approach is to using *SIOPs* representative of the Western UK shelf Seas as a whole, derived by averaging values for The Bristol Channel, The Clyde and the Irish Sea.

Before constituent retrievals using this approach can be presented, a series of validation tests are required to anticipate the robustness of this inversion algorithm. This will be done as follows:

1. The wavelength specific relationships derived in Chapter 4 will be tested using the linear derived gradient (m) value that is used to convert the R_{rs} signal to a b_b/a vector. The *in situ* data will be used to create the same relationships between R_{rs} and b_b/a to determine m and ascertain if the application of the generalized relationships is justified. The variation that is present between the two values of m could also give an indication of the expected error in recovery.

2. The inversion procedure involves the conversion of an R_{rs} signal to a b_b/a signal using the relationships described in Chapter 4. The b_b/a signal obtained can be compared with the *in situ* b_b/a measurements where these are available. This provides an intermediate step in the validation of the inversion process. Which does not depend on the SIOPs used for constituent recovery.

3. Finally, the quality of the constituents retrieved can be assessed.

$R_{rs}(\lambda)$ and $b_b/a(\lambda)$ data collected from the Western UK Shelf Sea are plotted in Figure 7.3. The line of best fit has a slope (m) of 21.2 compared to an m value of 21.4 for the

modelled data set (though the R^2 value of 0.6 is lower than in the modelling studies). This gives some confidence that the relationships derived for the modelled data are valid for this *in situ* data set. The lower R^2 value will provide an understanding for any deviations from a precise recovery.

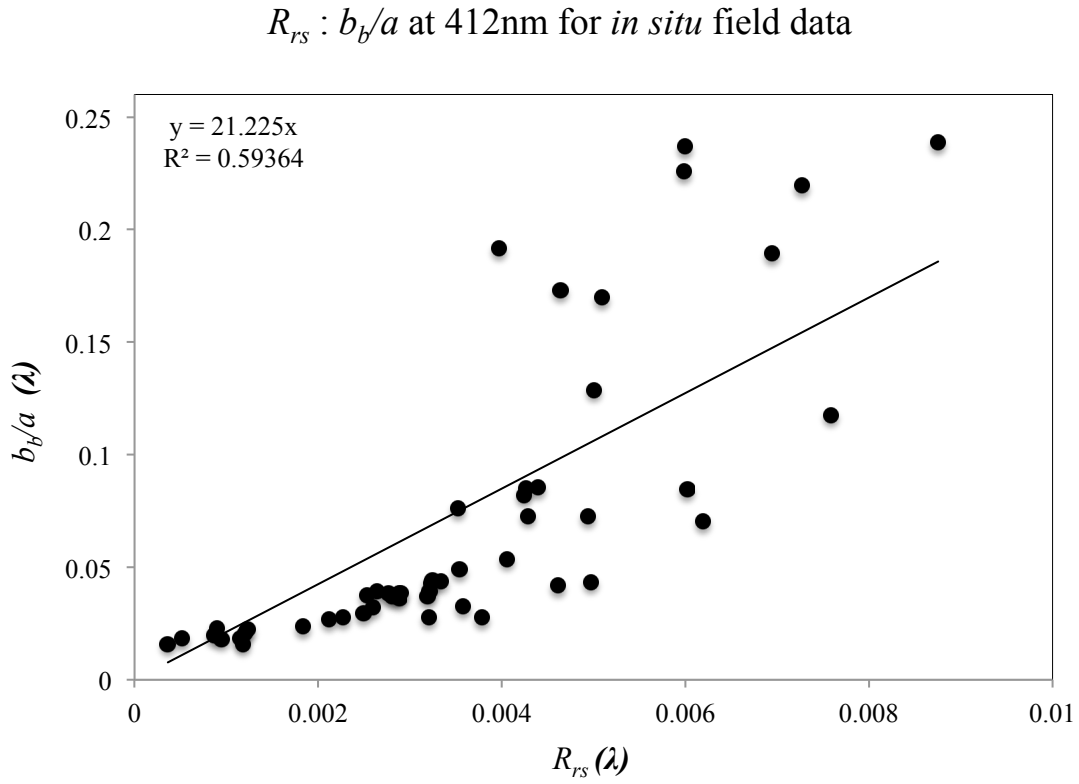

Figure 7.3 Relationship derived between *in situ* R_{rs} and b_b/a data.

The second stage of the validation prcoess is to examine the relationship between the observed and recoverd b_b/a signal. The results are presented in figure 7.4 for 412 nm. With an R^2 value of 0.71, the deviation from a perfect recovery suggests a certain amount of breakdown in the constituent recoveries. The remaning wavelengths present a similar distribution, although slightly more variation is observed at the red end of the spectrum.

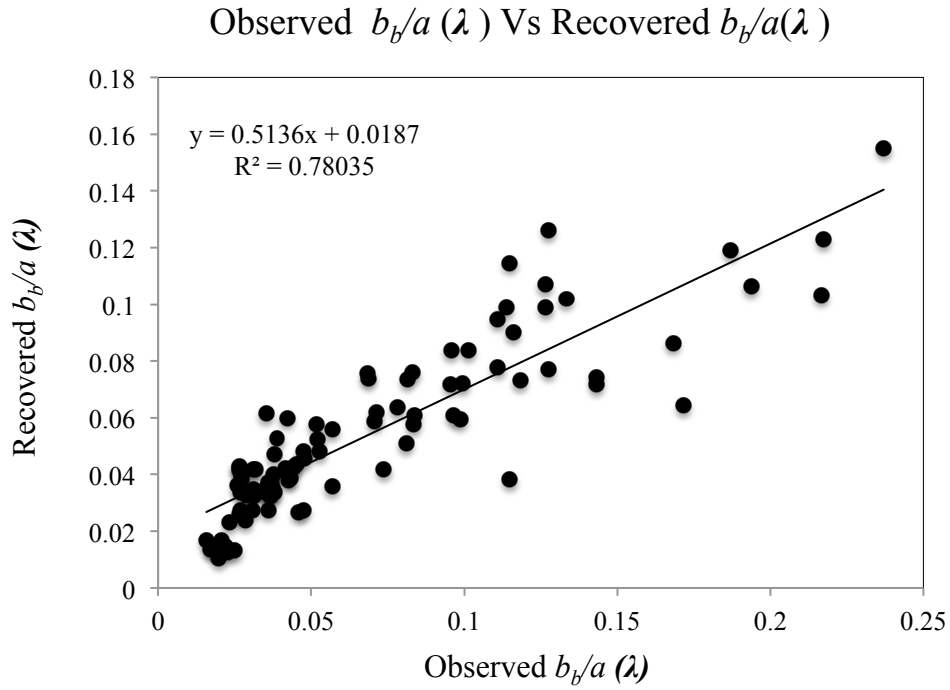

Figure 7.4. Comparison of the observed b_b/a signal to the recovered signal at 412nm.

The results in this chapter have demonstrated the level of uncertainty that can be anticipated when the inversion procedure developed within this work is applied to real data. The work of previous chapters has clearly demonstrated that the introduction of observational noise can significantly decrease the quality of constituent retrievals using modelled data and consequently, would be expected to be a contributing factor to any poor retrieval observed with *in situ* data. For the purpose of assessing the retrieval quality of the spectral matching algorithm, data was divided into the separate cruises that were undertaken to collect the data: The Bristol Channel, The Clyde and the Irish Sea, 2001 and 2002 cruises. Figure 7.5 to 7.7 presents all *in situ* data collected in the Western UK Shelf Sea. All constituents show an reasonable R^2 value when the observed concentration is compared with the recovered. Due to the range in concentrations, the true accuracy of recovery is masked. Consequently, the *in situ* data has been split into regions with the results displayed in figure 7.8 to 7.11 for The Bristol Channel, The

Clyde and the Irish Sea, 2001 and 2002 cruises, respectively. The results for the Bristol Channel have no recoveries for *CHL* or *CDOM*. This is due to the majority of recovered concentrations being 0 and is reflective of the results obtained in section 7.3 using the regionally derived relationships. In addition to the reasons listed in section 7.3, other reasons for the poor recoveries may be due to the absence of a close match within the *LUT* or due to the ambiguity that can exist due to observational noise. Regardless, the *MSS* recovery is generally good with a high R^2 value that is greater than the R^2 value for the created inversion relationships. Overall, the Clyde presents the best results across the constituent classes, particularly for *CHL*. It must be noted that variable quality of the *in situ* measurements is reflected in the constituent recoveries. The Bristol Channel data had a number of inconsistencies, making quality control and validation difficult. Finally, the Irish Sea has also demonstrated a good recovery for the data collected.

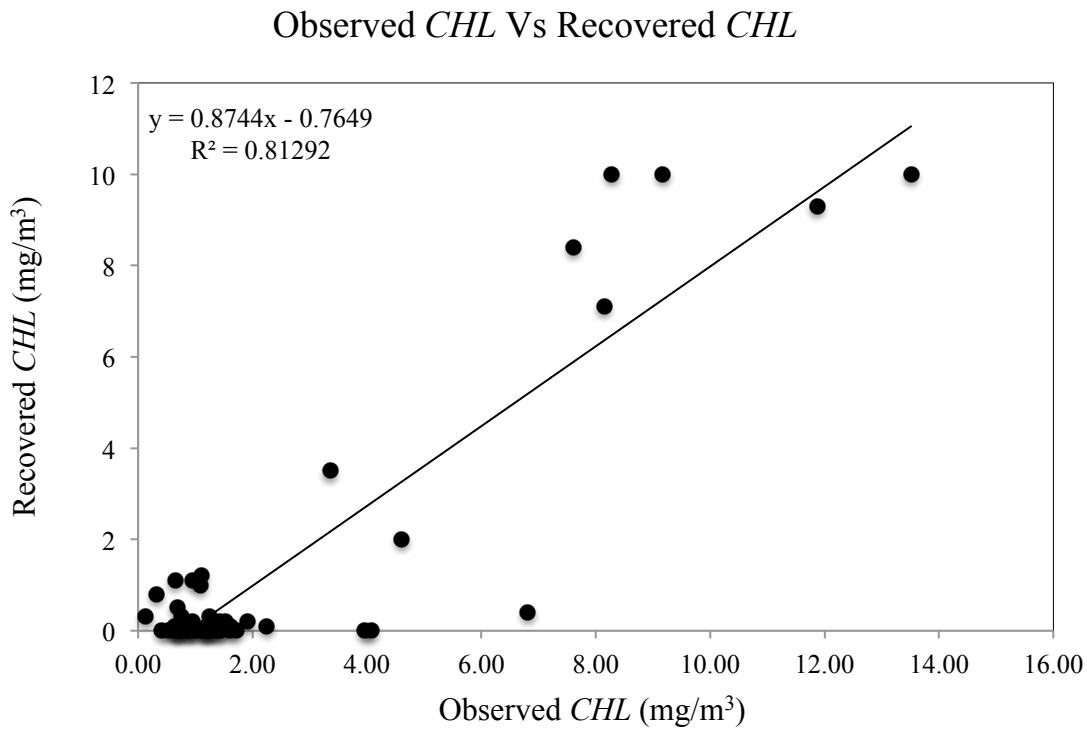

Figure 7.5. *CHL* recovery for *in situ* data collected in the Western UK Shelf Sea.

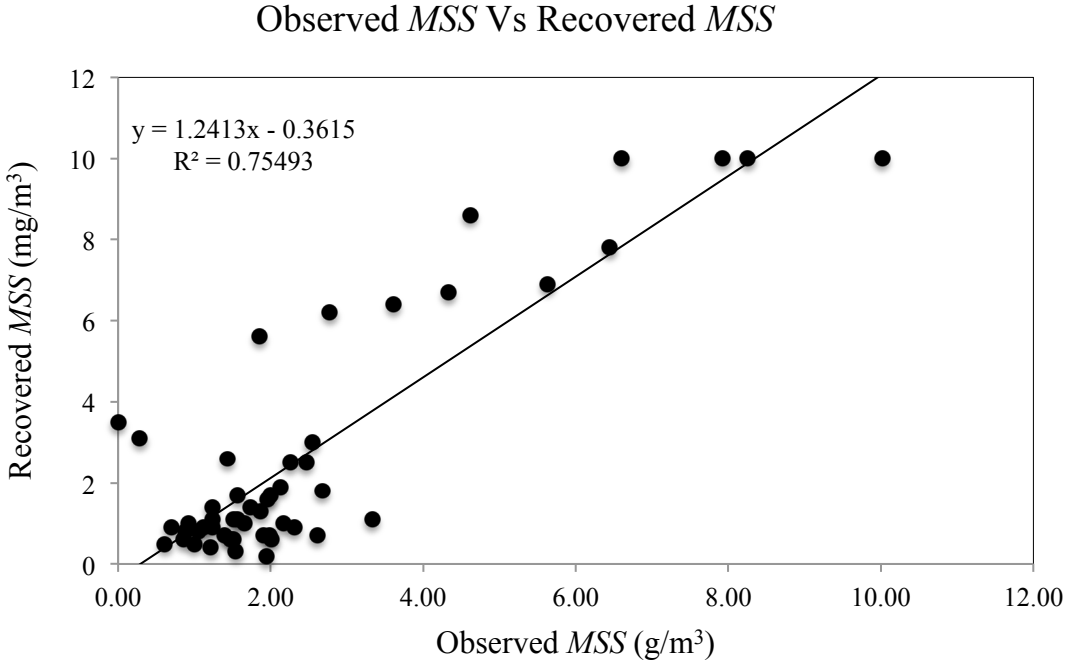

Figure 7.6. *MSS* recovery for *in situ* data collected in the Western UK Shelf Sea.

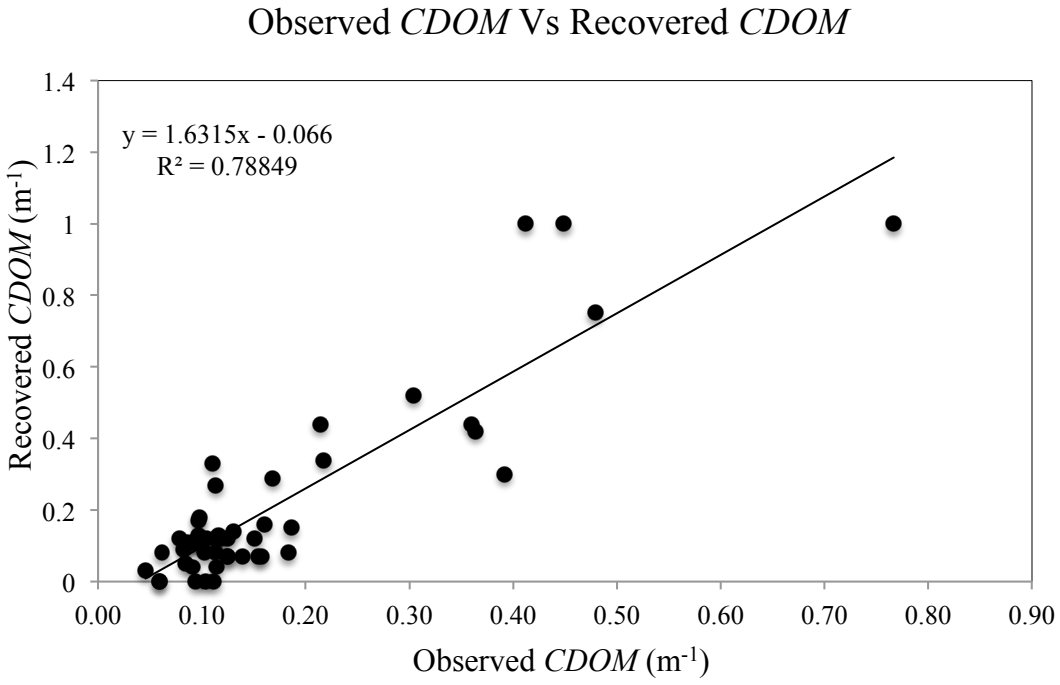

Figure 7.7. *CDOM* recovery for *in situ* data collected in the Western UK Shelf Sea.

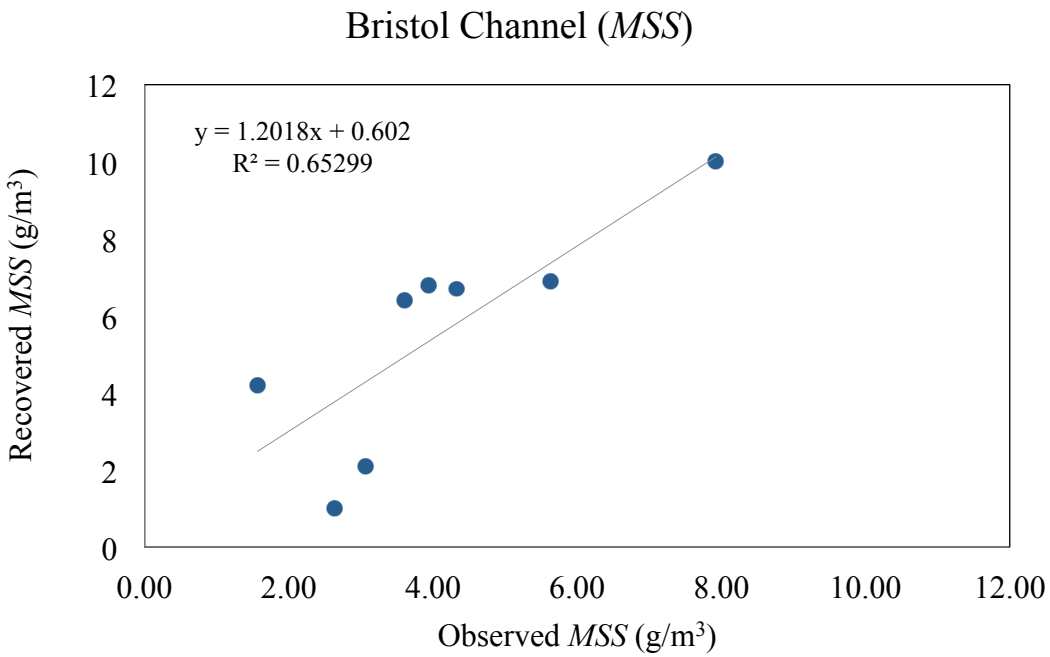

Figure 7.8. *MSS* retrieval for the Bristol Channel, using a simple least squares matching routine.

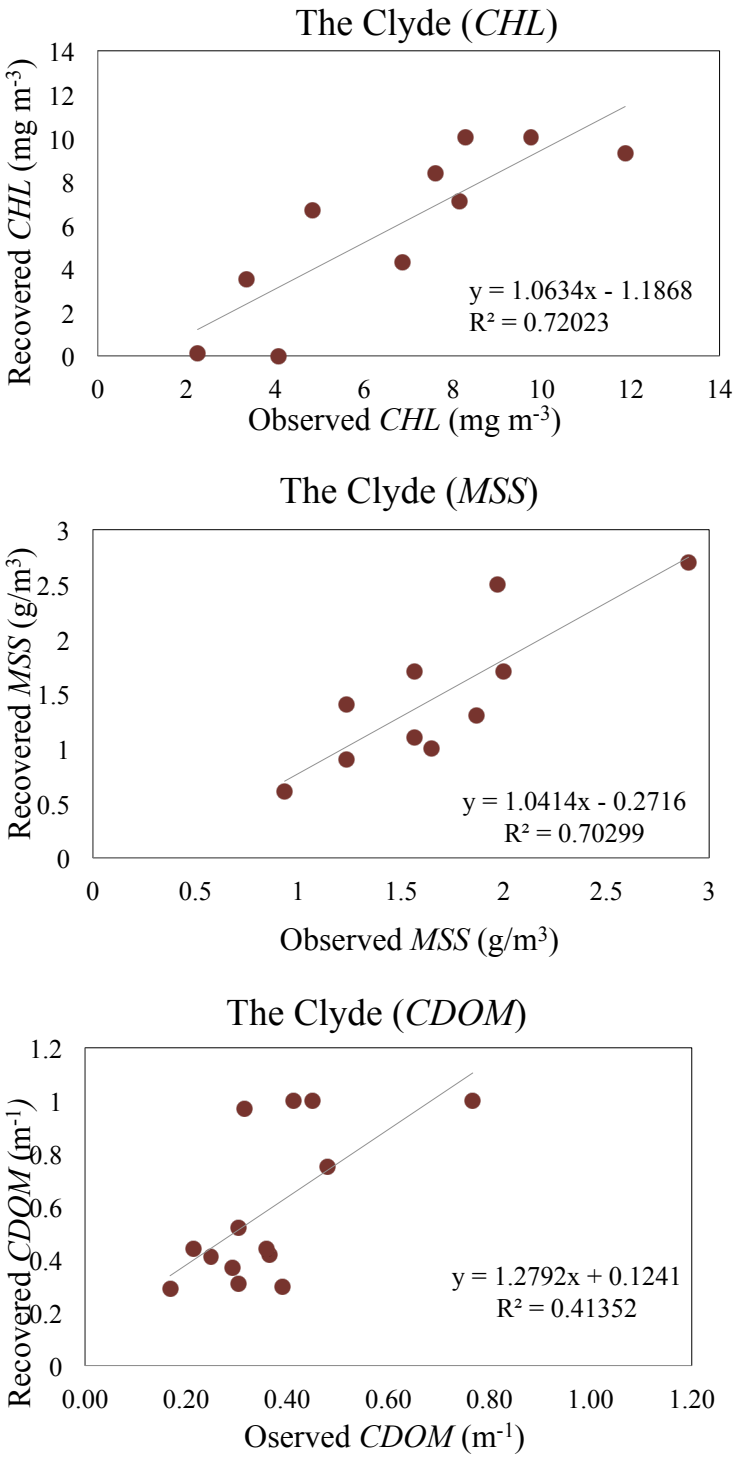

Figure 7.9. Constituent retrieval for The Clyde, using a simple least squares matching routine. Relatively good retrievals are observed for all particulates.

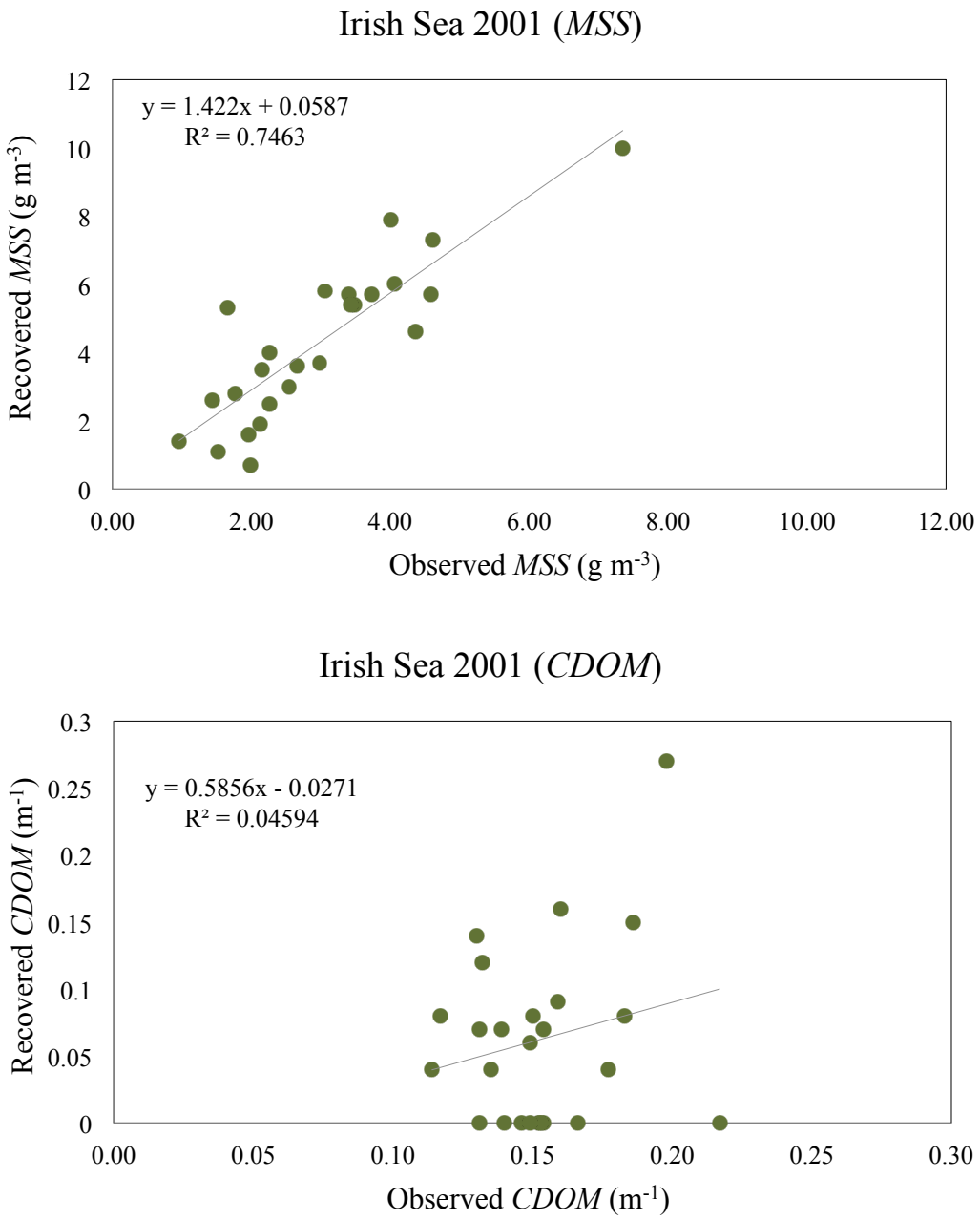

Figure 7.10. Constituent retrieval for the Irish Sea (2001), using a simple least squares matching routine. A Relatively good retrieval is observed for *MSS*.

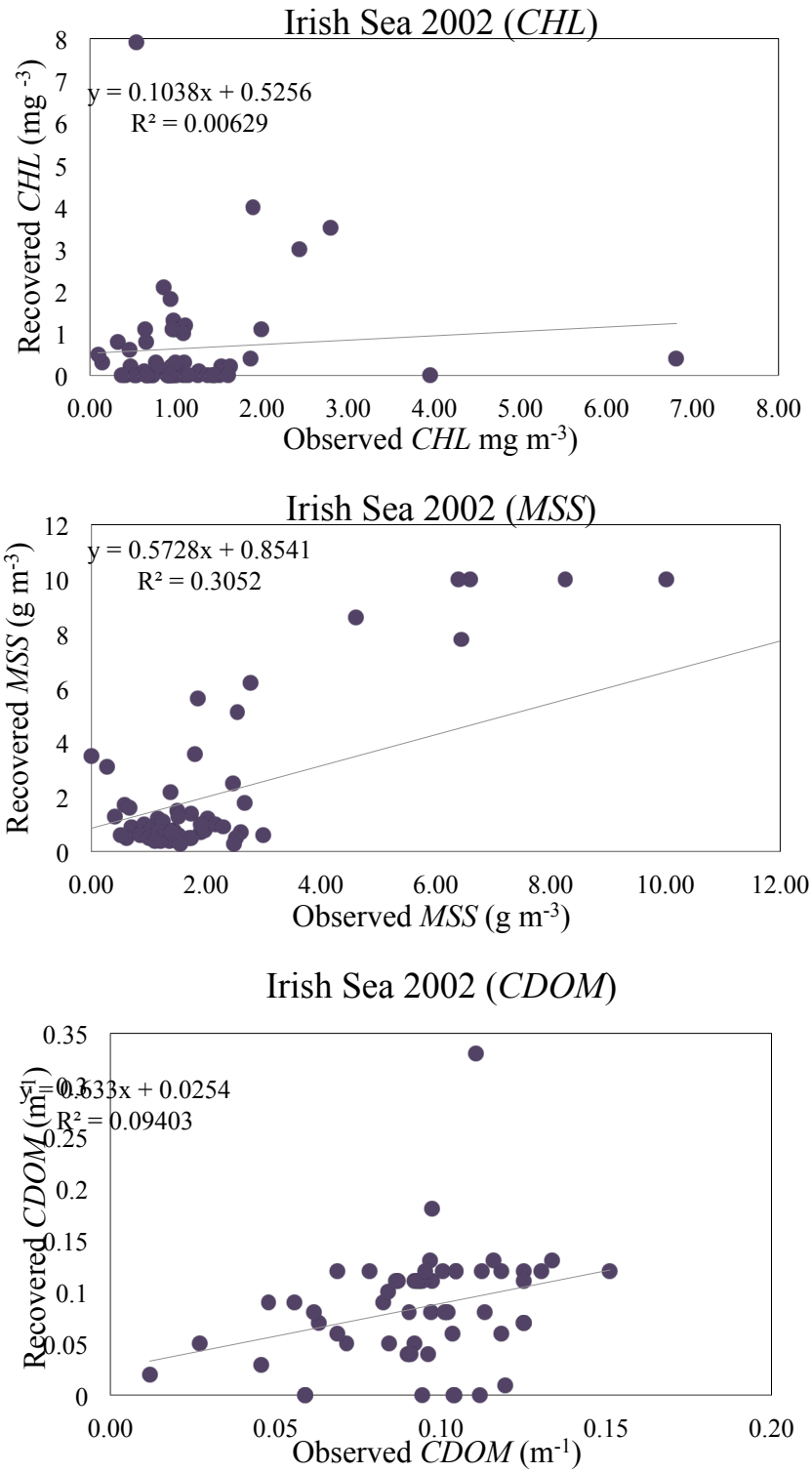

Figure 7.11. Constituent retrieval for the Irish Sea (2002), using a simple least squares matching routine. A Relatively good retrieval is observed for all constituents.

The results of the constituent retrieval have demonstrated that:

1. Remote sensing inversion using a simple least squares approach is possible and can yield quite accurate results, particularly for *MSS*.

2. The generation of new *LUTs* using *SIOPs* specific to a region of study does not produce improved constituent matches and may reduce the quality of retrievals due to the reduction in the size of the available data set .

3. While some inaccuracy can be attributed to the presence of noise in the observations, the quality of constituent retrievals is still good despite the use of a general 'one fits all' algorithm that is representative of a larger geographical area.

7.5 Chapter 7 Summary

- The relationships between R_{rs} and b_b/a were shown to not vary significantly when *SIOPs* specifc to each region were used to create them

- Overall, constituent retrieval was optimum using inversion relationships created from *SIOPs* representative of a larger geographical area, in comparison to those created on a small regional scale.

- While ambiguity exists in the form of observational noise, the quality of constituent retrievals is still good (represented by a high R^2 value) despite the use of a general 'one fits all' algorithm representative of a larger geographical area.

- The constituent retrieval using *SIOPs* representative of the Western UK shelf Sea has demonstrated reasonably well the benefit and level of accuracy that can be achieved using a simple, least squares spectral matching inversion algorithm.

Chapter 8

Conclusions and Discussion

This chapter shall give a summary of the conclusions and discussions that have been made throughout this thesis. This will be achieved by revisiting the outline of this thesis which was presented in chapter 1. Each of the chapter aims will be given again in italics, followed by the main conclusions of the chapter. Finally, suggestions for further work, relating directly to this thesis, shall be given.

8.1 Summary of Work

This work has shown that the propagation of natural light in turbid media (including seawater) is determined by both the conditions of illumination and the inherent optical properties of the medium. The illumination conditions include solar angle, degree of cloud cover and sea state, while the relevant inherent optical properties (*IOPs*) are the spectral coefficients of absorption and scattering and the scattering phase function. These inherent optical properties are functions of seawater composition, including the concentrations of phytoplankton, suspended minerals and dissolved organic substances. Using knowledge of the concentrations of these materials, obtained through a number of cruises in the Western UK shelf sea, and their specific optical cross-sections, the reflectance of a water body was calculated using radiative transfer theory. This work then attempted the inverse of this process for the determination of constituent concentrations from reflectance.

This work was undertaken because of the problem of reflectance inversion, which is at the heart of the optical remote sensing of oceanic processes. Optical remote sensing using satellite-borne radiometers has become an important tool for studying biological and physical processes in ocean basins (Dickey *et al*, 2004; Platt *et al*, 2008), and is recognized as being potentially of great value for monitoring the changing status of coastal waters and shelf seas (Petersen *et al*, 2008). Unfortunately, remote sensing algorithms derived using global data sets are not reliable when applied to waters subject to terrestrial influence (Robinson 2006). A solution to this problem is of great significance in modern oceanography, planetary science and climate change modelling.

This research project aimed to successfully invert remote sensing signals by spectral matching. This involved the comparison of water-leaving radiance spectra with a *LUT* of pre-defined spectra, calculated using radiance transfer theory for water columns of known composition. Ultimately, it has been demonstrated that inversion techniques can

be labour intensive and it is for this reason that the spectral matching inversion algorithm has been developed in this thesis. An easily adaptable inversion algorithm is highly desirable for the investigation of ocean colour, where fast and reliable results can be obtained without the time burden that is associated with more complex techniques and radiative transfer modelling. This work enabled the following challenging problems to be addressed:

1) The need for an effective computational scheme for database searching. This was achieved by implementing a simple least squares matching algorithm for the spectral matching.
2) An effective technique to by-pass the time consuming constraints of radiative transfer calculations. This was achieved through the development of *LUTs* that could be created quickly using Matlab and easily adapted to new regions of interest.
3) Uncovering the possible existence of ambiguities in the spectral matches. This was achieved by introducing errors wavelength by wavelength and assessing the quality of the constituent retrievals.
4) Robustness of a spectral matching approach to remote sensing inversion using modelled data as well as *in situ* radiometric data. This was also achieved by assessing the quality of constituent retrieval.
5) The implications of applying such an inversion algorithm to various spatial locations where water constituents are potentially very different, was investigated by using different regional locations as case studies.

The following section will give the main conclusions that can be drawn from this work on a chapter by chapter basis.

8.2 Conclusions and Discussion

A) CHAPTER2: FUNDAMENTAL OPTICAL PROPERTIES

The radiative transfer theory and the simple relationships that can be derived between remote sensing radiance signals and the backscattering to absorption ratio were investigated as a potential way to develop a spectral matching inversion algorithm using simple least square matching. It was concluded that under certain circumstances, this relationships can be expressed in the simplest form of $R_{rs}(\lambda) = G\, b_b/a\ (\lambda)$, to allow the investigation of the inverse problem of remote sensing and recover *OSM* concentrations from remote sensing reflectance signals.

B) CHAPTER 3: THE CALCULATION OF SPECIFIC INHERENT OPTICAL PROPERTIES (SIOPS)

Typical *SIOPs* were derived from *in situ* measurements that were collected from cruises that encompassed areas of the Western UK shelve seas. These *SIOPs* were calculated using the spectral absorption and beam attenuation coefficient (at nine wavebands) of water and were measured using; the WETLabs ac-9 *in situ* absorption and attenuation meter for the calculation of the scattering coefficient and; a HOBILabs HydroScat-2 backscattering sensor for the measurement of optical backscattering at two wavelengths. Matlab scripts were constructed to overcome the time burden of using Hydrolight's *GUI* and radiance distribution and *IOP* libraries were created for 75 environmental conditions.

C) CHAPTER 4: SIMPLIFICATIONS OF THE $R_{RS}(\lambda)$ TO $B_B/A(\lambda)$ RELATIONSHIP FOR USE IN SPECTRAL MATCHING

The generally complex relationship between $b_b/a(\lambda)$ and $R_{rs}\ (\lambda)$ can be reduced to a relatively simple approximation when specific conditions are applied. The work in this

chapter identified a wavelength dependency in the normalized water leaving (nL_w) spectra and R_{rs} (λ) signals when plotted against their $b_b(\lambda)/\ a(\lambda)$ spectral counterparts. A stronger wavelength dependency was observed for $nL_w(\lambda)$ signals due to the normalisation step and the range of phase function that can occur with large datasets. Due to the greater wavelength variation with the $nL_w(\lambda)$ to $b_b/a(\lambda)$ relationship, a 3rd order polynomial relationship, wavelength by wavelength, between $R_{rs}(\lambda)$ and $b_b/a(\lambda)$ was used for the inversion of remote sensing signals. However, for simplicity, linear relationships between R_{rs} (λ) and b_b/a (λ) were used for all analytical and comparative purposes.

The effects of environmental variability on the relationship of $b_b(\lambda)/\ a(\lambda)$: R_{rs} were investigated using these linear relationships. This investigation included a total of 75 combinations of different environmental conditions that included solar angle, cloud cover and wind speed. Variability was relatively low, with the difference between the maximum and minimum $R_{rs}(\lambda)$ signals (representing the 75 conditions) only 5% at 550 nm where the distribution visually looked the largest. However, having obtained relationships for the 75 environmental combinations, a selection process was incorporated into the inversion routine, whereby the user can select environmental conditions that best suits the region of data collection

D) CHAPTER 5. THE SPECTRAL MATCHING TECHNIQUE.

The matching algorithm used in this work showed comparative retrieval results to the widely implemented Euclidean matching algorithm. An increased resolution of the *LUT* resulted in a corresponding increase in the search time; however, such time inefficiencies could potentially be overcome with an increased computer processing speed.

In comparison to other, more complex techniques, discussed in chapter 1, such as: the Levenberg-Marquardt (*LM*) multivariate optimisation algorithm, genetic algorithms,

particle swarm optimisation and neural networks, the *LUT* and spectral matching procedure adopted in this work provides a data-set versatility that the more complex techniques do not. It can be quickly adapted to the changes in optical properties and therefore subsequent changes in *SIOPs*, that can occur with spatial variability.

E) CHAPTER 6: SIGNIFICANT SOURCES OF ERRORS AND THEIR POTENTIAL EFFECTS

The addition of random noise to the "observed" spectrum reduced the number of matches produced for a given acceptance interval. *CHL* retrieval was affected more strongly by the addition of noise to spectral observations than *MSS* or *CDOM*. These investigations also revealed that the potential size of spectral neighborhoods, at each wavelength, increased as the acceptance criteria of the *RMSE* was relaxed.

CHL specific absorption and backscattering coefficients were shown to vary significantly for each of the five phytoplankton species examined. Constituent retrievals deviated from the perfect recoveries when the matched spectrum was derived from the *SIOPs* that were representative of the individual phytoplankton species while the *LUT* was created using the *SIOPs* that were generally representative of the Western UK Shelf Sea.

The sensitivity of a simple spectral matching model to observational noise means that the derivation of *OSM* concentrations is subject to errors in optically complex waters. However, the accuracy of the recoveries could be predicted using modelling studies, and this was tested using the results given in chapter 7.

F) CHAPTER 7: REGIONAL CASE STUDIES

The inversion relationships created using modelled data were validated using *in situ* data. The inversion algorithm was considered to have performed well when the consituent rettrival acheived R^2 values reaching 0.8.

The use of regionally derived *SIOPs* caused no improvement to the quality of *OSMs* retrieved. In fact the quality of retrievals were considerably poorer than the ones

observed when general *SIOPs* were used which were considered to be representative of the Western UK Shelf Sea.

These results have demonstrated that a remote sensing inversion using a simple least squares approach is possible and can yield useful results, particularly for *MSS*.

While the approach presented here allows for the generation of new *LUTs* using *SIOPs* specific to a region of study this may reduce the quality of retrievals due to the limited sampling of that region. Ultimately, while ambiguity exists in the form of observational noise, the quality of constituent retrievals is still good despite the use of a general 'one fits all' algorithm that is representative of a larger geographical area.

8.3 Suggestions for further work

This work has uncovered the potential problems associated with new technologies and methods. However, as discussed within this work, there are potential solutions. For example, the simple inversion method demonstrated within this work has scope for improvement by perhaps using hyper-spectral data as this would allow optimum wavelengths to be selected that in turn increase the quality of constituent recoveries. The areas that have been highlighted within this work as requiring work at a community wide level has a particular emphasis on the standardisation of methods. This includes, but is not limited, to the following issues:

1. The determination of scattering spectra for the different classes of materials in natural marine suspensions, and the degree to which these spectra are spatially variable, needs further investigation. A standardisation of the methods used to determine this information would also facilitate a greater transfer of information amongst colleagues and allow algorithms that require such information to be universally applicable.

2. The spectral dependence of the b_{bp}:b_p ratio is a very important for ocean colour modelling. There is debate whether this shape can be described by a power law, and what form this law may have...

3. Ideally, the algorithm developed in this work would be applied to remote sensing satellite images, and validation of the constituent retrievals using in situ sampling would be required. The provision of high quality *in situ* data that coincides in time and space with cloud-free satellite images requires a major, resource-intensive and coordinated programme of work.

References

Aas E (1996). Refractive index of phytoplankton derived from its metabolite composition. *Journal of Plankton Research* 18, 2223-2249.

Aas E, Hokedal J and Sorensen K (2005). Spectral backscattering coefficient in coastal waters. *International Journal of Remote Sensing* 26, 331-343.

ac-9 User's Guide (Revision T), WETLabs, Philomath Oregon, (2008)

Aurin DA, Dierssen HM, Twardowski MS and Roesler CS (2010). Optical complexity in long island sound and implications for coastal ocean color remote sensing. *Journal of Geophysical research Oceans* 115, C07011, doi 10.1029/2009JC005837

Babin M, Morel A, Fournier-Sicre V, Fell F and Stramski D (2003). Light scattering properties of marine particles in coastal and open ocean waters as related to the particle mass concentration. *Limnology and Oceanography* 48, 843-859.

Bagheri S, Stamnes K and Li W (2001). Application of radiative transfer theory to atmospheric correction of aviris data. *Proceedings of the Tenth Airborne Earth Science Workshop*, JPL Publication 02-1.

Bailey DH, Bjorstad PE, Gilbert JR, Mascagni RS, Simon HD, Torczon VJ and Watson LT (1995). Parallel processing for scientific computing. *Proceedings of the seventh SIAM Conference*.

Binding CE, Bowers DG and Mitchelson-Jacob G (2003). An algorithm for the vertical retrieval of suspended sediment concentrations in the Irish sea from SeaWiFs ocean colour satellite imagery. *International Journal of Remote Sensing* 24, 3791-3806.

Bissett PW(2006). Continued development of the look-up-table (*LUT*) methodology for interpretation of remotely sensed ocean colour data. *Florida Environmental Research Institute* Award Number: N00014-06-1-0370.

Boss E, Stramski D, Bergmann T, Pegau WS and Lewis M (2004). Why should we measure optical backscattering? *Oceanography* 17, 44-49.

Boss E, Pegau WS, Lee M, Twardowski M, Shybanov E, Korotaev G and Baratange F (2004). Particulate backscattering ratio at LEO 15 and its use to study particle composition and distribution. *Journal of Geophysical Research* 109, C01014, doi: 10.1029/2002JC001514.

Brando VE and Dekker AG (2003). Satellite hyperspectral remote sensing for estimating estuarine and coastal water quality. *Transactions and Remote Sensing* 41, 1378-1387.

Bricaud A, Morel A and Prieur L (1981). Absorption by dissolved organic matter of the sea (yellow substance) in the UV and visible domains. *Limnology and Oceanography*, 26, 43 -53.

Bricaud A, Roesler C and Zaneveld JRV (1995). In situ methods for measuring the inherent optical properties of ocean waters. *Limnology and Oceanography* 40, 393-410.

Brown CA, Huot Y, Werdell PJ, Gentilli B and Claustre H (2008). The origin and global distribution of second order variability in satellite ocean colour and its potential applications to algorithm development. *Remote Sensing of Environment* 112, 4186-4203.

Bukata RP, Jerome JH, Kondratyev KY and Pozdnyakov DV (1995). *Optical Properties and Remote Sensing of Inland Coastal Waters*, 1st edition, Florida: CRC Press LLC, Chapter 1.

Cannizzaro JP, Carder KL, Chen RF, Heil CA and Vargo GA (2008). A novel technique for the detection of the toxic dinoflagellate, *Karenia brevis*, in the gulf of Mexico from remotely sensed ocean colour data. *Continental Shelf Research* 28, 137-158.

Carder KL, Chen FR, Cannizzaro JP, Campbell JW and Mitchell BG (2003). Performance of the MODIS semi-analytical ocean colour algorithm fro chlorophyll a. *Advances in Space Research* 33, 1152-1159.

Chami M, Mckee D, Leymarie E and Khomenko G (2006). Influence of the angular shape of the volume scattering function and multiple scattering on remote sensing reflectance. *Applied Optics* 45, 9210-9220.

Chami M, Shybanov EB, Churilova TY, Khomenko GA, Lee MEG, Martynov OV, Berseneva GA and Korotaev GK (2005). Optical properties of the particles in the Crimea coastal waters (Black Sea). *Journal of Geophysical Research* 110, C11020.

Chang G and Whitmire AL (2009). Effects of bulk particle characteristics on backscattering and optical closure. *Optical Express* 17, 2132–2142.

Chen J, Jia X, Yang W and Matsushita B (2009). Generalisation of subpixel analysis for hyperspectral data with flexibility in spectral similarity measures. *IEEE Transactions in Geoscience and Remote Sensing* 47, 2165-2171.

Defoin-Platel M and Chami M (2007). How ambiguous in the inverse problem of ocean colour in coastal waters? *Journal of Geophysical Research* 112, C01014, doi: 10.1029/2002JC001514.

Dickey TD (2004). Studies of coastal ocean dynamics and processes using emerging optical technologues. *Oceanography* 17, 9-11.

Doxaran D, Ruddick K, Mckee D, Gentili B, Tailliez D, Chami M and Babin M. (2009). Spectral variations of light scattering by marine particles in coastal waters, from visible to near infrared. *Limnology and Oceanography* 54, 1257-1271.

Fang LG, Chen SS, Li D and Li HL (2009). Use of reflectance ratios as a proxy for coastal water constituent monitoring in the Pearl River estuary. *Sensors* 9, 656-673.

Fournier G and Forand JL (1994). Analytic phase function for ocean water. *J S Jaffe* 2258, 194-201. In ocean optics XII SPIE.

Gallegos CL (2005). Optical water quality of blackwater river estuary: the lower St Johns river, Florida USA. *Estuarine, Coastal and Shelf Science* 63, 57-72.

Garver, S and Siegel D (1997). Inherent optical property inversion of ocean colour spectra and its biogeochemical interpretation. Time series from the Sargasso sea. *Journal of Geophysical Research* 102(C8).

Gordon HR, Brown OB, Evans RH, Brown JW, Smith RC, Baker KS and Clark DK (1988) A semianalytic radiance model of ocean colour. *Journal of Geophysical Research* 93, 10909-10924.

Gordon HR and Morel A (1983). Remote assessment of ocean colour for interpretation of satellite visible imagery. *A review, Springer-Verlag,* New York (USA).

Gordon, HR, Lewis MR, McLean SD, Twardowski MS, Freeman SA, Voss KJ, and Boynton GC (2009). Spectra of particulate backscattering in natural waters. *Opt. Express* 17(18), 16192-16208.

Gould RW, Arnone RA and Martinolich PM (1999). Spectral dependence of the scattering coefficient in case 1 and case 2 waters. *Applied Optics* 38, 2377-2383.

Gregg WW, Casey NW, O'Reilly JE and Esias WE (2009). An empirical approach to ocean colour data: reducing bias and the need for post-launch radiometric re-calibration. *Remote Sensing Environment* 113, 1598-1612.

Hagan MT, Demuth HB and Beale M (1996). *Neural Network Design*, 1st edition, Boston: PWS Publishing Co, Chapter 2.

Hallegraeff GM (2003). Harmful algal blooms: a global overview. In Hallegraeff, G.M., Andewrson, D.M. and Cembella, A.D. (eds) 2003. *Manual on Harmful Marine Microalgae.* UNESCO, Paris

Hayes D, Testor P, Zodiatis G, Konnaris G, Hannides A, Mortier L, Beguery L, DÓrtenzio F, Mauri E, Lekien F, Gerin R, Poulain P and Lazar A (2010). Glider transects in the Levantine Sea: a study of the warm core cyprus eddy. *Rapp. Comm. Int. Mer, Med* 39.

Howari FM (2003). Comparison of spectral matching algorithms for identifying natural salt crusts. *Journal of Applied Spectroscopy* 70, 782-787.

Hubert L, Lubac B, Dessailly D, Duforet-Gaurier L and Vantrepotte V (19??). Effect of inherent optical properties variabiliton the chlorophyll retrieval from ocean colour remote sensing: an in situ approach.

HydroScat-2 User's Manual (Revision H), Tucson Arizona (2008)

Jeffrey SW and Humphrey GF (1975). New spectrometric equations for the determining chlorophylls a, b, c1, c2 in algae, phytoplankton and higher plants. *Biochem. Physiol. Pflanz* 167,191-194.

Jeffrey SW, Mantoura RFC and Wright WW (1997). *Phytoplankton pigments in oceanography: Guidelines to modern methods (monographs on oceanographic methodology)*. UNESCO.

Jeffrey SW and Vesk M (1997). Introduction to marine phytoplankton and their pigment signatures, p. 37-84. In: S.W. Jeffrey, R.F.C. Mantoura, and W.W. Wright [eds]. *Phytoplankton pigments in oceanography: Guidelines to modern methods (monographs on oceanographic methodology)*. UNESCO.

Jerlov NG (1957). A transparency meter for ocean water. *Tellus* 9, 229-233.

Jerlov NG (1968) *Optical Oceanography*, 1st edition, London: Elsevier Publishing, Volume 5.

Kempeneers P, De Backer S and Park Y (2005). Retrieval of oceanic constituents from ocean colour using simulated annealing. *IEEE*, 5651-5654.

Kirk JTO (1983). *Light and Photosynthesis in Aquatic Ecosystems*, 1st edition, Cambridge: Cambridge University Press, Chapter 1.

Kirk JTO (1991). Volume scattering function, average cosines and the underwater light field. *Limnology and Oceanography* 36, 455-467.

Kirk JTO (1994). "The relationship between the inherent and the apparent optical properties of surface waters and its dependence on the shape of the volume scattering

function" in *Ocean Optics*, R. W. Spinrad, K. L. Carder, M. J. Perry, eds., (Oxford University Press, Oxford, 1994).

Kishino M, Takahashi M, Okami N and Ichimura S (1985). Estimation of the spectral absorption coefficients of phytoplankton in the sea. *Bulletin of Marine Science* 37, 634-642.

Komick NM, Costa MPF and Gower J (2009). Bio-optical algorithm evaluation for *MODIS* for western Canada coastal waters: An exploratory approach using *in situ* reflectance. *Remote Sensing of Environment* 113, 794-804.

Korosov AA, Pozdnyakov DV, Folkestad A, Pettersson LH, Sorensen K and Shuchman R (2009). Semi-empirical algorithm for the retrieval of ecology relevant water constituents in various aquatic environments. *Algorithms* 2, 470-497.

Kostadinov TS, Siegel DA, Maritorena S and Guillocheau N (2007). Ocean colour observations and modeling for an optically complex site: Santa Barbara channel, California, USA. *Journal of Geophysical Research* 112, C07011.

Kuchinke CP, Gordom HR, Harding LW and Voss KJ (2009). Spectral optimisation fro constituent retrieval in case 2 waters II: validation study in the Chesapeake Bay. *Remote Sensing of Environment* 113, 610-621.

Lee Z, Carder KL and Arnone RA (2002). Deriving inherent optical properties from water colour: a multiband quasi-analytical algorithm for optically deep waters. *Applied Optical* 41, 5755-5772

Levenberg K (1944). A method for the solution of certain non-linear problems in least squares. *Quant Applied Mat* 2, 164-168.

Liu CC and Miller RL (2008). Spectrum matching method for estimating the chlorophyll-a concentration, *CDOM* ratio and backscatter fraction from remote sensing of ocean colour. *Canadian journal of Remote Sensing* 34, 343-355.

Loisel H, Meriaux X, Berthon JF and Poteau A (2007). Investigation of the optical backscattering to scattering ratio of marine particles in relation to their biogeochemical composition in the eastern English Channel and southern North Sea. *Limnology and Oceanography* 52, 739-752.

Lourakis MIA (2005). A brief description of the Levenberg-Marquardt algorithm implemented by levmar. *Institute of Computer Science*, FORTH.

Maffione RA and Dana DR (1997). Instruments and methods for measuring the backward-scattering coefficient of ocean water. *Applied Optics* 36, 6057-6067.

Martinez-vicente V, Land PE, Tilstone GH, Widdicombe C and Fishwick JR (2010). Particulate scattering and backscattering related to water constituents and seasonal changes in the Western English Channel. *Journal of Plankton Research* 32, 603-619.

Maritorena, S, Siegel DA and Peterson AR (2002). Optimisation of a semianalytical ocean color model for global-scale applications. *Applied Optics* 41, 2705−2714.

Marquardt DW (1963). An algorithm for least-squares estimation of non-linear parameters. *Journal of the International Society of Applied Math* 11, 36-48.

McLain (2009). Environmental factors controlling the Barents Sea spring summer phytoplankton blooms. *Geophysical Research Letters* 36.

Mckee D, Cunningham A and Craig S (2003). Semi-empirical correction algorithm for ac-9 measurements in coccolithophore bloom. *Applied Optics* 42, 4369-4374.

Mckee D and Cunningham A (2005). Evidence for wavelength dependence of the scattering phase function and its implication for modelling radiance transfer in shelf seas. *Applied Optics* 44, 126-135.

Mill and Nu (1998). Specific absorption of phytoplankton in gulf of California.

Mobley CD (1994). *Light and Water Radiative Transfer in Natural Waters*, 1st edition, London: Academic Press Limited, Chapter 3 and 8.

Mobley CD (1999). Estimation of the remote sensing reflectance from above surface measurements. *Applied Optics* 38, 7442-7455.

Mobley CD and Sundman LK (2001). Hydrolight 4.2 Technical Documentation. Second printing, *Sequoia Scientific Inc*.

Mobley CD, Sundman LK and Boss E (2002). Phase function effects on oceanic light fields. *Applied Optics* 41, 1035-1050.

Mobley CD, Sundman LK, Davis CO, Bowles JH, Downes TV, Leathers RA, Montes MJ, Bissett WP, Kohler DDR, Reid RP, Louchard EM amd Gleason A (2005). Interpretation of hyperspectral remote-sensing imagery by spectrum matching and look-up tables. *Applied Optics* 44, 3576-3592.

Morel A (1973). Light scattering by seawater. Experimental results and theoretical approach. *Optics of the Sea* AGARD lecture series.

Morel A (1974). Optical properties of pure water and pure seawater. Chapter 1

Morel A and Gentili B (1993). Diffuse reflectances of oceanic waters II. Bidirectional aspects. *Applied Optics* 32, 6864-6879.

Morel A, Gentili B, Chami M and Ras J (2006). Bio-optical properties of high chlorophyll case 1 waters and of yellow-substance dominated case 2 waters. *Deep Sea Research* 53, 1439-1459.

Morel A and Gordon HR (1980). Report on the working group on water colour. *Boundary Layer Meteorology* 18, 343-355.

Morel A and Maritorena S (2001). Bio-optical properties of ocean water: A reappraisal. *Journal Of Geophysical Research Oceans* 106, 7163-7180.

Morel A and Mueller JL (2003). Normalised water leaving radiance and remote sensing reflectance: bidirectional reflectance and other factors. *Ocean Optics Protocols for Satellite Ocean Colour Sensor Validation, Revision 4* Volume 3.

Morel A and Prieur L (1977). Analysis of variations in ocean colour. *Limnology and Oceanography* 22, 709-722.

Morel A and Smith RC (1982). Terminology and units in optical oceanography. *Marine Geodesy* 5, 335-349.

National Research Council. *Assessing Requirements for Sustained Ocean Color Research and Operations* Washington, DC: The National Academies Press, 2011.

Oubelkheir K, Clemenston LA, Webster IT, Ford P, Dekker A, Radke L and Daniel P (2006). Using inherent optical properties to investigate biogeochemical dynamics in a tropical macrotidal coastal system. *Journal of Geophysical Research Oceans* 111, 15.

Peng F, Effler SW, O'Donnel D, Weidemann AD and Auer MT (2009). Characterisations of minerogenic particles in support of modelling light scattering in Lake Superior through a two-component approach. *Limnology and oceanography* 54, 1369-1381.

Philpot W, Davis CO, Bissett WP, Mobley CD, Kohler DDR, Lee Z, Bowles J, Steward RG, Agrawal Y, Trowbridge, Gould RW and Arnone RA (2004). Characterisation from hyperspectral image data. *Oceanography*17, 76-85.

Platt TN, Hoepffner N, Stuart V and Brown C (2008). Why ocean colour? The societal benefits of ocean colour technology. *IOCCG Report Number 7*.

Pope RM and Fry (1997) Absorption spectrum (380 700nm) of pure water: II. Integrating cavity measurements. *Applied Optics* 36, 8710-8723.

Preisendorfer RW (1961). *Application of radiative transfer theory to light measurements in the seas*. International Union of Geodesy and Geophysics Monographs.

Qiu Hand Hancock ER (2006). Graph matching and clustering using spectral partitions. *Journal of pattern recognition* 39, 22-34.

Ressom HW, Turner K and Musavi M (2006). Estimation of ocean water chlorophyll-a concentration using fuzzy c-means clustering and artificial neural networks. *International Joint Conference on Neural Networks*, 4118-4125.

Risovic D (1993). Two-component model of sea particle size distribution. *Deep Sea Research* 40, 1459-1473.

Robinson, I.S. and Sanjuan-Calzado, V. (2006). The application of satellite ocean colour data to marine ecosystem models. Report D2.3.6 for the Marine Environment and Security for the European Area - Integrated Project (MERSEA-IP). *Institut Français de Recherche pour l'Exploitation de la Mer* - France, 40pp.

Schiller H and Doerffer R (1997). Neural network for emulation of an inverse model-operational derivation of case 2 water properties from MERIS data. *International Journal of Remote Sensing* 9, 1735-1746).

Slade WH, Ressom HW, Musavi MT and Miller RL (2004). Inversion of ocean colour observations using particle swarm optimisation. *IEEE Transactions of Geoscience and Remote Sensing* 42, 1915-1923.

Smith RC and Baker K (1978). The bio-optical state of ocean waters and remote sensing. *Limnol Oceanogr* 23, 247.

Snyder WA, Arnone RA, Davis CO, Goode W, Gould RW, Ladner S, Lamela G, Rhea WJ, Stavn R, Sydor M and Weidemann A (2008). Optical scattering and backscattering by organic and inorganic particulates in U.S. coastal waters. *Optical Society of America* 47, 666-677.

Spinrad RW, Carder KL and Perry MJ (1994). *Ocean Optics*, 1st edition, New York: Oxford University Press, Chapters 1 -2.

Stavn RH and Keen TR (2004). Suspended minerogenic particle distributions in high-energy coastal environments: optical implications. *Journal of Geophysical Research* 109, C05005, doi: 10.1029/2003JC002098.

Stavn RH and Richter S (2008). Biogeo-optics; particle properties and the partitioning of the spectral scattering coefficient of ocean waters. *Applied Optics*47, 2660-2679.

Stramski D, Bricaud A and Morel A (2001). Modelling the inherent optical properties of the ocean based on the detailed composition of the planktonic community. *Applied Optics* 40, 2929-2945.

Stramski D, Wozniak SB and Flatau PJ (2004). Optical properties of Asian mineral dust suspended in seawater. *Limnology and Oceanography* 49, 749-755.

Stramski D, Babin M and Wozniak SB (2007). Variations in the optical properties of terrigenous mineral-rich particulate matter suspended in seawater. *Limnology and Oceanography* 52, 2418-2433

Sullivan JM, Twardowski MS, Zaneveld JR, Moore C, Bernard A, Donaghay PL and Rhoades B (2006). The hyper-spectral temperature and salinity dependent absorption of pure water, salt water and heavy salt water in the visible and near IR wavelengths. *Applied Optics* 45, 5294-530.

Sun D, Li Y, Wang Q, Gao J, Lv H, Le C and Huang C (2009). Light scattering properties and their relation to the biogeochemical composition of turbid productive waters: a case study of Lake Taihu. *Applied Optics* 48, 1979-1989.

Suzuki K, Kishino M, Sasaoka K and Saitoh S (1998). Chlorophyll specific absorption coefficients and pigments of phytoplankton off Sanriku, Northwestern North Pacific.

Tassan S and Ferrari (1998). Measurement of the light absorption by aquatic particulates retained in filters: determination of the optical pathlength amplification by the transmittance -reflectance. *Method J Plankton Res* 20, 1699-1709.

Ulloa O, Sathyendranath S and Platt T (1994). Effect of the particle size-distribution on the backscattering ratio in seawater. *Applied Optics* 33, 7070-7077.

Vaillancourt RD, Brown, CW, Guillard RRL and Balch WM (2004). Light backscattering properties of marine phytoplankton: relationships to cell size, chemical composition and taxonomy. *Journal of Plankton Research* 26, 191-212.

Van De Hulst HC (1957). *Light Scattering by small particles*. New York: Dover.

Wernand MR, Shimwell SJ, Boxall S and Van Aken HM (1998). Evaluation of specific semi-empirical coastal colour algorithms using historic data sets. *Aquatic Ecology* 32, 73-91.

Whitmire AL, Boss E, Cowles TJ and Pegau WS (2007). Spectral variability of the particulate backscattering ratio. *Optics Express* 15, 7019-7031.

Wozniak SB and Stramski D (2004). Modelling the optical properties of mineral particles suspended in seawater and their influence on ocean reflectance and chlorophyll estimation from remote sensing algorithms. *Applied Optics* 43, 3489-3503.

Yentsch CS (1962). Measurement of visible light absorption by particulate matter in the ocean. *Limnology and Oceanography* 7, 207-217.

Zhan H, Lee Z, Shi P, Chen C and Carder K (2003). Retrieval of water optical properties for optically deep waters using genetic algorithms. *IEEE Transactions on Geoscience and Remote Sensing* 41, 1123-1128.